Prediction of Energy Production from Wind Farms with Case Study of Baja California

A thesis is submitted to
The University of Manchester
for the degree of
Doctor of Philosophy
in the Faculty of
Engineering and Physical Sciences

2016

Gabriel Cuevas-Figueroa

School of Mechanical, Aerospace and
Civil Engineering

Table of Contents

Word Count: 49,694

List of Figures

List of Tables

Abstract

The University of Manchester
Gabriel Cuevas Figueroa
Doctor of Philosophy
Prediction of energy production from wind farms
with case study of Baja California

The influence of deployment of planned wind farms on the power output and energy yield of wind farms located in close proximity at downwind sites is investigated. The atmospheric model Weather Research and Forecasting (WRF) has been employed to simulate wind resource and energy yield from wind farms in the Baja California region of Northern Mexico. Accuracy of predicted wind speed and wind turbine energy supply are evaluated against full-scale measurements from a met-mast and from each of five 2 MW turbines at the La Rumorosa wind-farm. For this wind farm location, wind speed distribution is predicted to within 1.4% and the energy supply from the farm predicted to within 5.25%. Accuracy depends on the boundary layer model and atmospheric dataset employed. Wind farms are modelled using the scheme developed by Fitch et al. (2012) in which a momentum sink and turbulent kinetic energy source are defined as a function of the turbine thrust coefficient and power output, each of which vary with wind speed as defined by the manufacturer. Planned farms of up to 72 MW installed capacity are defined in terms of turbine number, rated power and spacing at four sites such that each farm operates with a typical capacity factor. For a single farm of 2 MW turbines located 10 km upwind, wind speed at the case study wind-farm is reduced by 3.00% and power output reduced by up to 5.84%. These deficits increase if 5 MW turbines are deployed rather than 2 MW turbines due to the development of a longer far-wake. The net energy supply from several sites in the region is assessed.

Declaration

No portion of the work referred to in the thesis has been submitted in support of an applicant for another degree or qualification of this or any other University or other Institute of learning.

Copyright Statement

Acknowledgements

I would like to thank my supervisors Dr Tim Stallard and Prof Peter Stansby for welcoming me into this research group, and for their excellent guidance, wise advice and unconditional support to improve my skills as scientist and researcher.

I would like to thank Prof Teresa Alonso Rasgado and the Latin American Postgraduate Programme from the University of Manchester for bringing me the opportunity of discovering this amazing Institution.

I would like to thank the Baja California Energy Commission for providing the met-mast and SCADA data from the La Rumorosa I wind farm. In the same way, I would like to express my gratitude to the Mexican Federal Electricity Commission, particularly to the Geothermoelectric Project Management Office, for providing additional met-mast data for this study.

I would like to acknowledge the National, Oceanic and Atmospheric Administration (NOAA) for the availability of the GFS, NAM and NARR meteorological datasets. I would like to acknowledge the use of WRF model, which is available on online from the Mesoscale and Microscale division of NCAR.

I would also like to acknowledge the assistance given by IT Services and the use of the Computational Shared Facility at The University of Manchester.

I would like to thank the Mexican National Council for Science and Technology (CONACyT) and the Secretariat of Public Education (SEP) for the financial support of this research, without which this would not have been possible.

Many thanks to all my friends and colleagues from the University, who have helped me to keep pushing throughout my studies.

And last, but not least, I could not find the words to express my gratitude to my Mother and my Family, who have been supporting me during these years to fulfil this achievement.

Notation

a	Dimensionless parameter which controls the shape of the attenuation of deceleration as a function of distance from the rotor plane.
a_i	Deceleration in the zonal, meridional and vertical directions, represented by i = 1, 2, 3 respectively.
A	Amplitude of deceleration.
A_0	Swept area of the rotor
A_{ijk}	Cross-sectional rotor area of one wind turbine bounded by model levels k, k+1 in grid cell i.
c	Shape factor
C_P	Power Coefficient
c_p	Specific heat at constant pressure
C_T	Thrust Coefficient
C_{TKE}	Fraction of energy converted into TKE
cv	Coefficient of variation
d	Perpendicular distance from a computational grid point to the actuator disk
dE_{LR}	Percentage wind energy deficit at La Rumorosa I wind farm
E_F	Wind energy yield calculated at the La Rumorosa I wind farm considering only the wind resource
E_w	Wind energy yield calculated at the La Rumorosa I wind farm accounting for the wake effect from close proximity farms
E	Wind energy yield obtained from the SCADA system
E_{approx}	Wind energy yield calculated from WRF and power curve
$\dot{E}_{kin,pc\|wp}$	Energy removal tendency given by the power output curve
Fr_x	Frictional acceleration in the *x* direction
Fr_y	Frictional acceleration in the y direction
Fr_z	Frictional acceleration in the z direction
$f(v)$	Weibull probability density function
f_{ij}	Horizontal density function of wind turbines per area
$F(v)$	Cumulative distribution function
g	Acceleration of gravity
H	Rate of gain or loss of heat
i	Grid-point index in *x* direction

j	Grid-point index in y direction
k	Grid -point index in z direction
k	Scale factor
k_1	Constant value
k_2	Constant value
l	Length scale
L	Perpendicular distance over which the deceleration is applied
m	Mass
N_t^{ij}	Horizontal density of wind turbines (number of turbines per square metre)
n_u	Number of wind speed bins
p	Pressure
P	Power
$P_w(U_i)$	Electrical power output from the wind turbine
P_{ijk}	Power extracted by the turbines
$P(u_{rh})$	Kinetic energy flux through the rotor area
q_v	Specific humidity
Q_v	Rates of gain or loss of water vapour through phase changes
R	Gas constant for dry air (287 J/kg K)
RMSE	Root Mean Square Error
$RMSE_f$	Root Mean Square Error for a statistical distribution
$RMSE_\theta$	Root Mean Square Error for a wind rose distribution
STDE	Standard Deviation
t	Time
T	Temperature
TKE_{ijk}	Turbulence kinetic energy
u	East–west component of wind
u_w	Wind speed from the simulations
u_r	Wind speed for the wind resource only
u_i	ith component of velocity
U	Air velocity
U_s	Velocity deficit
U_0	Hub-height velocity
v_i	Wind speed for the time step i
v	North–south component of wind

V	Volume
$\|\mathbb{V}\|_{ijk}$	Velocity vector over the rotor area
W	Wake width
w	Vertical component of wind
x	East–west space coordinate
y	North–south space coordinate
z	Vertical space coordinate
z_k	Height under the wind turbine rotor
z_{k+1}	Height over the wind turbine rotor
Greek Symbols	
α	Dimensionless parameter which
Δ	Change or difference in some quantity, operator
δ	Wind energy yield relative error
γ	Vertical lapse rate of temperature
γ_d	Dry adiabatic lapse rate of temperature
η_{elmech}	Loss factor due to mechanical friction within the wind turbine and electrical losses caused
θ	Counter clockwise angle between the mean wind vector and the turbine
θ_o	Offset of the angle
θ_{mm}	Angle measured at the met-mast
θ_{AEG}	Angle measured at each of the wind turbines
θ_c	Corrected angle
θ_m	Angle which appears more often for each wind turbine offset
ρ	Air Density
ρ_{rh}	Air Density at rotor height
ρ_{lo}	Reference Density
ρ_0	Reference Density
ϕ	latitude
Ω	Rotational frequency of Earth
Abbreviations	
AEG	Wind Turbine
ASOS	Automated Surface Observing Systems
ASTER	Advanced Spaceborne Thermal Emission and Reflection Radiometer

CFD	Computational Fluids Dynamics
CFE	Comisión Federal de Electricidad
CIMIS	California Irrigation Management Information System
CSF	Computational Shared Facility
DECC	Department of Energy and Climate Change
DOE	Department of Energy's
GFS	Global Forecast System
GDEM	Global Digital Elevation Model
IIE	Instituto de Investigaciones Eléctricas
INEGI	Instituto Nacional de Estadística y Geografía
LSM	Land Surface Model
MYJ	Mellor-Yamada-Janjic
MYNN	Mellor-Yamada Nakanishi and Niino
MYNN2	Mellor-Yamada Nakanishi and Niino level 2.5
NAM	North American Mesoscale
NARR	North American Regional Reanalysis
NASA	National Aeronautics and Space Administration
NCEP	National Centre for Environmental Prediction
NCWCP	NOAA Center for Weather and Climate Prediction
NW	Northwest
NWP	Numerical Weather Prediction
NREL	National Renewable Energy Laboratory
PBL	Planetary boundary layer
QNSE	Quasi-Normal Scale Elimination
RANS	Reynolds Average Navier Stokes
RUC	Rapid Update Cycle
SCADA	Supervisory Control and Data Acquisition
SIGEA	Sistemas Integrales de Gestión Ambiental
SL	Surface Layer
SODAR	Sonic Detection and Ranging
TEMF	Total Energy - Mass Flux
TKE	Turbulent Kinetic Energy
USA	United States of America
UTC	Coordinated Universal Time
W	West

WECC	Western Electricity Coordinating Council
WRF	Weather Research and Forecasting
WSW	West-Southwest
YSU	Yonsei University scheme

Chapter 1 Introduction, motivation and aims

The energy supply for the country of Mexico during 2011 depended vastly on fossil fuels (88.69%) (Fig. 1.1) (Alemán-Nava et al., 2014). During the same period, the renewable energy mix provided almost 7% of annual energy production. The portfolio of renewable energy sources in Mexico includes hydropower, geothermal, biomass, solar and wind power. Less than 0.15% was produced from solar and wind power, and there is an opportunity for increased energy supply from these technologies. The Renewable Energy Target for 2018 (DOF, 2015) defines a goal of 5% installed capacity of wind and solar. Additionally, the General Law of Climate Change (CDHCU, 2015) sets a target for the energy supply from renewable sources of 35% in 2024. Reaching that percentage in such a short amount of time will be a great challenge, requiring high investments in the renewable energy sector. It is estimated that investment of $14 billion USD would be required to increase wind energy installed capacity from 2,551 MW to 9,500 MW (Reuters, 2015) by 2018. This plan to increase the installed capacity by more than three times in Mexico will be a significant challenge.

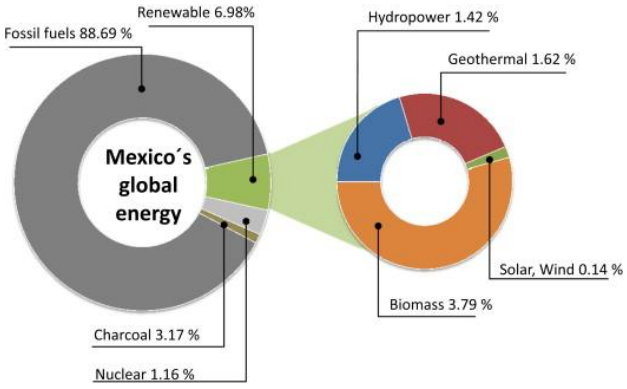

Figure 1.1 Mexico's energy global production, 2011 (Alemán-Nava et al., 2014).

In Mexico, many potential sites have been identified that may be suitable for wind farm deployment. These sites are typically in relatively complex terrain, in

mountainous regions, and potential sites may be in relatively close proximity (order of 10-20 km spacing). It is important to obtain accurate predictions of both energy yield from potential sites and the sensitivity of energy yield to future expansion of wind farms at sites in close proximity to the existing site.

This chapter provides an overview of wind energy systems (Section 1.1). The research aims are outlined in Section 1.2. Section 1.3 presents a brief description of the wind resource assessment. And Section 1.4 describes the structure of the Thesis.

1.1 Wind Energy

Historically, wind power has been converted into useful types of power such as transport in boats, mechanical power in wind-mills and electricity from wind turbines. The latter, provide electricity to communities or power networks which supply electricity to houses, schools, hospitals and the industrial sector amongst other users. Modern wind turbines can be considered in terms of five principal components: the rotor, the drive train, the nacelle, the tower and the machine controls.

Each wind turbine has a representative power curve, which defines the power output considering the operating speed at hub height (Fig. 1.2). This curve has three main points: the cut-in speed, which is the minimum speed to operate; rated power wind speed, being the value where the rated power is reached; and the cut-out speed, which is the maximum wind speed at which the wind turbine can operate.

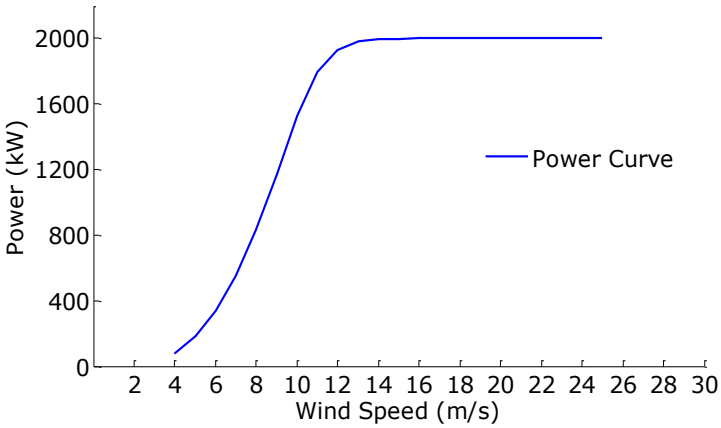

Figure 1.2 Gamesa G87 2.0 MW power curve (Gamesa, 2007).

Power extraction by wind farms results in a region of reduced wind speed, a wake, downwind. The wake recovers towards the ambient flow profile over a distance that is dependent on the rate of energy extraction, the unsteadiness of the ambient flow and on the local topography. These wakes could cause a deficit in the annual wind energy yield which may affect the accomplishment of monthly energy production, and hence the profitability of the wind farm. To ensure financial profitability of wind farms, careful consideration must be given to the siting, to minimise the influence of the wakes of upwind farms on power production and financial profitability. In some regions, constraints on wind farm siting would result in the installation of operation of farms located within the wake region of upwind farms. To establish power production of two wind farms located in close proximity and directly downstream one to the other, inter wind farm wake effects have to be examined.

At present, there is no legislation in Mexico or worldwide, which clearly expresses the distance that has to be set between two wind farms in order to avoid any shadowing due to the wake of the upwind farm. Wind resource assessments and micrositing analysis are performed over areas to maximise the performance of an individual wind farm, by locating the amount of wind turbines which provides the greatest capacity factor. Nevertheless, there has

been little analysis of the impact that future farms may have on the energy yield of existing farms.

1.2 Research Aims

Due to the renewable energy goals in the near future and the expected increase of wind energy installed capacity, wind farms will be installed in close proximity to each other within areas with feasible wind resource. This would impact on their performance due to the wake created downwind, which can extend beyond 16 km (Jiménez et al., 2015). In this case, to ensure fair energy yield production, an inter wind farms wake effects analysis will have to be performed considering effects from potential wind farms on existing farms.

The overall aim of this study is to identify the effect that future wind farms may cause over an existing wind farm. The focus of the analysis is a wind farm located in the area of La Rumorosa, in the Northwest of Mexico. As the Numerical Weather Prediction (NWP) models have been recently applied for wind resource assessment and wind turbine wake description, they can also be applied to evaluate the effects on the mesoscale, which will allow areas with multiple farms to be covered. This Thesis aims to better understand the wake interaction between wind farms, represented by NWP methods, such as the WRF model. The objectives identified to fulfil this aim are:

- To determine the accuracy of NWP models such as WRF for simulation of wind-speed and direction measurements from a met-mast.
- To determine the accuracy with which NWP models such as WRF may be employed to predict energy yield of a typical wind farm.
- To assess effects of different meteorological datasets on wind speed and wind-farm energy yield predictions.
- To assess sensitivity of wind speed and energy yield prediction to alternative WRF model parameterization model configuration.

- To quantify the influence of planned wind farm developments on the energy yield and power output of an existing wind farm that is located downwind within the same geographical region.
- To assess influence of wind farm proximity and specification on energy supply from the case study region.

1.3 Wind Resource Assessment

The rate at which energy is conveyed by wind is a cubic function of the wind speed. In this value lies the importance of the wind resource analysis, which is vital for the wind farm site selection and its annual energy production forecast. Wind energy is mainly originated from the sun's energy transmitted to the Earth; this solar radiation causes temperature and pressure differences, which produce the wind movement.

The instability of the wind is the main feature to analyse at energy production areas. The variation of the wind can be related to time and space. These changes have different applications for the wind power industry, from resource assessment, to site selection or even for wind turbine design (Spera, 1994) (Fig.1.3). All these fluctuations are mainly dependent on the height and geographic conditions of the area, such as the vegetation and the topography characteristics, which can present high roughness and high and low gradients in the elevation.

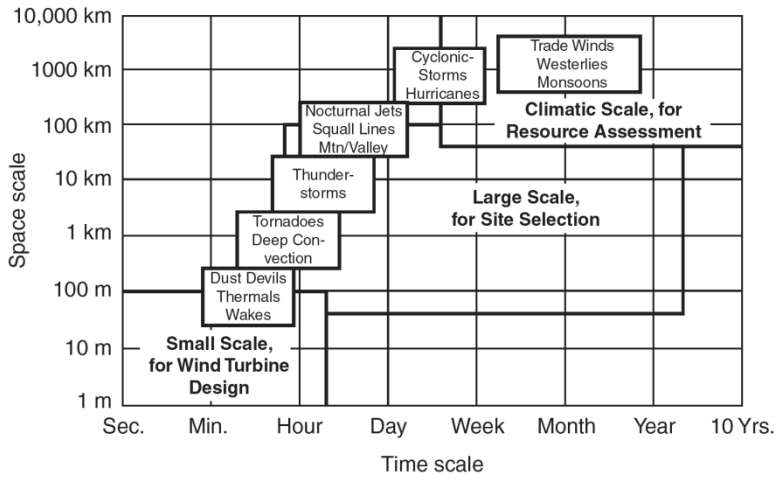

Figure 1.3 Time and space scales of atmospheric motion (Spera, 1994).

Time variation of wind speed can be considered over the following timescales: inter-annual, annual, diurnal and short-term (Manwell et al., 2002). Inter-annual oscillations are defined in time scales longer than a year and are applied for long period wind energy production, such as decades or more, which are important for economic viability assessment. An annual wind characteristic analysis is the most common for wind energy, because it helps to forecast monthly energy production based on the seasons of the year, which are more predictable than inter-annual forecasts.

The wind characteristics are different from day and night, due to the changes of the heat transfer to the atmosphere. These variations are important to programme the energy production and its integration into the electricity network. Finally, the short-term scale wind variation, also referred to as turbulence, is important to quantify the individual performance of the wind turbines, quality of energy produced and lifetime (Burton et al., 2001).

In this context, the forecasting and description of wind characteristics is vital in the decision making process, and can be divided into two areas: short-term variation prediction and long-term forecasts. The first forecasting methods are based on statistical techniques applied to wind speed data, often from a met-mast; whereas, the long-term forecast employs meteorological models. The

incorporation of both, atmospheric and statistical forecasts is able to provide highly effective wind energy production forecasts (Burton et al., 2001). In the following chapters, theory of the wind energy, the atmospheric structure and phenomena, and the NWP models methodology are presented.

1.4 Synopsis

Six more chapters are considered on this Thesis, described as follows.

Chapter 2 presents the background theory concerning operation of wind turbines and wind farms, prediction of energy yield from wind farms and provides background to a particular case study region and site for which resource and wind farm performance data are available. Also described are the atmospheric processes affecting the wind resource and the principal features of numerical weather prediction models, which describe computationally the atmospheric phenomena and are used to evaluate the wind resource over specified geographic regions and time intervals. This covers topics such as the domain resolution, different meteorological datasets studies, and sensitivity analysis for different atmospheric parameterization models.

Chapter 3 describes the Weather Research and Forecasting (WRF) model and the use up to date for studying the wind resource and performance and operation of wind farms. WRF is the state of the art for weather forecasting and atmospheric phenomena description, being widely used from daily forecast up to cyclone trajectory predictions; and as the objective of this research, as a tool to evaluate the wind resource and the wakes from operating wind farms.

Chapter 4 presents results from an analysis to evaluate the accuracy with which WRF predicts wind farm energy yield. Alternative meteorological datasets and boundary layer schemes are assessed in terms of the prediction accuracy of a short time interval from 2011 and an aggregated time interval from 2014, which

are selected to represent the annual wind resource statistics at the case study site.

Chapter 5 details an evaluation of the wind turbine parameterization model (Fitch et al., 2012). Met-mast and operating data from the wind turbines of La Rumorosa I wind farm were analysed based on the wind direction. Samples with a wind direction aligned to the farm layout were extracted to identify the wake effect along the wind turbines array.

Chapter 6 focuses on inter-wind farm effects. A four weeks aggregated period, considering on week per season time were selected, being representative on both wind speed and direction distribution to the annual data. The same sensitivity analysis was performed as in Chapter 4 and from the configuration with the best agreement, six future installed capacity scenarios were depicted, considering two wind turbines layouts and three different wind turbine rated power models.

Chapter 7 presents the conclusions and the recommendations to enhance this research in a broader area.

Chapter 2 Background Theory

In this chapter, basic concepts concerning wind energy are presented. The atmospheric processes and structure are described and background is given to the structure of Numerical Weather Prediction models. Section 2.1 provides an overview of Wind Energy systems. Section 2.2 explains the atmospheric structure and processes and Section 2.3 defines the numerical weather prediction models and their schemes.

2.1 Wind Energy

This Section provides a description of the characteristics of the wind resource and the methodologies employed to quantify wind turbine performance. The main features of wakes developed during wind turbine operation are described as are the steps taken to identify suitable locations for wind turbines and farms. Applications of wind energy and considerations to follow due to their grid connection are described. Typical wind resource assessment methodologies are briefly summarised. Section 2.1.1 presents the wind characteristics and resources, the aerodynamics and performance of wind turbines are described in Section 2.1.2 and the wake effects are covered in Section 2.1.3. Description of the wind turbine sitting is presented in Section 2.1.4 and the applications of the wind energy are covered in Section 2.1.5.

2.1.1 Wind characteristics and resources

The Sun is the primary source of renewable energy. Greater amounts of solar radiation are absorbed at the equator than at the poles causing different pressures at each location. This uneven heating results in pressure gradients within the atmosphere which generate the wind circulation around the globe. As well as varying with location, the amount of solar radiation to the Earth changes throughout the year resulting in seasonal variations. The wind

characteristics change in both time and space, these last are mainly due to the height and geographical conditions. Time variations can be over various timescales ranging from inter-annual, through seasonal, diurnal to turbulent scales. Diurnal variations are due to the Earth's rotation and may be significant particularly in mid-latitude locations such as the tropics for which high wind speed can occur during the day and low speed from midnight to sunrise. The variability of the wind can be described by sampling every second and averaging for ten minutes. The short-term variations describe the turbulence of the flow.

To quantify the available wind power, the mass flow of air crossing the area swept by a wind turbine rotor is considered. Following the continuity equation of fluid mechanics this flow is dependent on air density and velocity:

$$\frac{dm}{dt} = \rho A U \tag{2.1}$$

Were dm/dt is the mass flow of air, ρ is the air density, A is the swept area and U is the air velocity, assumed as uniform. The power of the flow is given by:

$$P = \frac{1}{2}\frac{dm}{dt}U^2 = \frac{1}{2}\rho A U^3 \tag{2.2}$$

And finally, the wind power per unit area or power density is given by:

$$\frac{P}{A} = \frac{1}{2}\rho U^3 \tag{2.3}$$

From equation (2.3), it has to be noted that the wind power density is proportional to the air density and to the cube of wind velocity. Within the atmosphere, the planetary boundary layer is the section that is located at the bottom and it is in direct contact with the surface of the Earth. In this layer the wind velocity, temperature and moisture vary over short spatial scales and short timescales. The change of the horizontal wind speed along the vertical axis is referred to as the vertical profile of the wind speed. Velocity is expected to be zero at the surface and increase with the height in this layer following a log-law or power-law profile. This profile is important to define the wind

turbine energy yield, as allows to extrapolate the wind speed at further heights than measured. The shear of the velocity profile sets the variability of the loading, which is a crucial factor in evaluation of turbine and blade design life.

Within this layer, part of the kinetic energy from the wind is dissipated into thermal energy through turbulent processes. Smaller eddies are constantly created and dissipated within short periods. This is mainly caused by two reasons: the roughness of the surface from the Earth and due to the vertical movement of air masses due to thermal effects, where the density is affected directly from the temperature. Warm air is less dense and rises up, while cold air is denser and sinks. The changes of the wind speed along the vertical profile define the stability of the atmospheric boundary layer, which can be classified as stable, neutrally stable, or unstable.

A met-mast has to be installed to gather the meteorological wind speed measurements from the potential wind farm site. Such masts support anemometers for the wind velocity, vanes for the wind direction, thermometers to measure the temperature and barometers to calculate the pressure. Generally, the data is measured every second and ten-minute averages are stored.

2.1.2 Wind turbine performance and energy yield

Wind turbines are machines which convert the kinetic energy from the wind into electricity. For a given flow-speed, energy yield from a wind turbine is dependent on the rotor geometry, operating strategy and generator rating. For wind power analysis, the wind can be described as a spatial and temporal mean over the rotor area and for a given interval. When a large amount of wind speed measurements are collected, the wind energy yield can be calculated from the corresponding power curve of the wind turbine. The energy yield E_w from the turbine is then:

$$E_w = \sum_{i=1}^{N} P_w(U_i)(\Delta t) \quad (2.4)$$

Where $P_w(U_i)$ is the electrical power output from the wind turbine for each steady flow of speed U_i, referred to as a power curve (see Section 1.1) Δt is the time interval of each sample, typically ten minutes and N is the number of wind speed measurements.

To perform accurate wind energy yield prediction for wind energy development, a reliable and detailed source of wind data is required. However, to obtain these data, met-masts tower, which are very expensive, have to be installed and operated, mesoscale modelling techniques or numerical weather prediction models, can be applied to identify suitable places to install these met-masts. Additionally, the numerical weather prediction models can be applied to predict and forecast the wind speed. These forecasts can be done for wind farm operational purposes, for forecast periods of minutes through to hours, or can be applied for wind power development planning, for forecast periods of days to weeks. For forecasts over long time periods, precursor meteorological forecasts are typically employed as input to extrapolate down to finer spatial scales over the region of interest for wind farm siting.

As energy is extracted from the mass of air passing through the rotor plane, the mean flow velocity is reduced. Since mass flux is conserved the stream tube, that delineates the flow passing the rotor from the ambient flow, increases in diameter. A pressure drop also occurs across the rotor plane. In this way, the wind after the turbine, once the energy has been extracted, has a lower speed and static pressure, this portion of the flow is named the wake. After a short distance downwind pressure recovers to the ambient atmospheric pressure. Further downwind flow velocity recovers as the wake mixes with the ambient flow through viscous processes.

The actuator disc concept defines the change in the velocity along the cross-sectional area of the wind turbine. Defining a smaller area for the stream tube

upwind than downwind. As the mass flow rate has to be consistent within these stages, and it is defined as:

$$\rho A_{\infty} U_{\infty} = \rho A_d U_d = \rho A_w U_w \tag{2.5}$$

Where ρ is the air density, A is the cross-sectional area and U is the wind speed. The suffix ∞ refers to far upstream conditions, d denotes the conditions at the disc and w defines a location within the far wake at which pressure has recovered to atmospheric pressure. The wind turbine performance is typically characterised in terms of the variation of power and thrust with time-averaged wind speed. From these variables, the power produced over a time period defines the amount of energy produced from the wind turbine, while the thrust determines the structural design of the wind turbine and supporting tower. It is appropriate to identify performance indexes in a non-dimensional form, to facilitate comparison of alternative turbine designs. The power coefficient (C_P), which is a relation of the power generated from the wind turbine and the power in the wind over the rotor's area.

$$C_P = \frac{P}{\frac{1}{2}\rho U^3 A} = \frac{Rotor\ power}{Power\ in\ the\ wind} \tag{2.6}$$

Where P is the power from the rotor, ρ is the density of the air, U is the velocity of the wind and A is the circular area swept by the rotor. In this way, the C_P expresses the amount of the energy flux conveyed by the wind which is converted to useful electrical power by the wind turbine. In an analogous manner to the power coefficient, the thrust coefficient (C_T) describes the thrust of a wind turbine with a non-dimensional value:

$$C_T = \frac{T}{\frac{1}{2}\rho U^2 A} = \frac{Thrust\ force}{Dynamic\ Force} \tag{2.7}$$

where T is the Thrust and all other parameters are as equation (2.6).

2.1.3 Weibull Probability Density Function Analysis

It is known that a Weibull probability density function provides a reasonable approximation to the probability of occurrence of mean wind speeds at a particular location over a long time interval. Application of such distributions represents the wind speed as a random variable, and combined with a power curve facilitates calculation of the annual energy yield from a wind turbine at a given location. The Weibull probability density function *f(v)* and the cumulative distribution function *F(v)* are described by the following equations:

$$f(v) = \frac{k}{c}\left(\frac{v}{c}\right)^{k-1} \exp\left[-\left(\frac{v}{c}\right)^{k}\right] \tag{2.8}$$

$$F(v) = 1 - \exp\left[-\left(\frac{v}{c}\right)^{k}\right] \tag{2.9}$$

where k is the scale factor, c is the shape factor and v is the wind speed. To estimate these parameters for the available data, the Maximum Likelihood method (Stevens and Smulders, 1979) was applied in this study. Scale and shape parameters were obtained by iterative solution of the following equations:

$$k = \left[\frac{\sum_{i=1}^{n} v_i^k \ln(v_i)}{\sum_{i=1}^{n} v_i^k} - \frac{\sum_{i=1}^{n} \ln(v_i)}{n}\right]^{-1} \tag{2.10}$$

$$c = \left[\frac{1}{n}\sum_{i=1}^{n} v_i^k\right]^{\frac{1}{k}} \tag{2.11}$$

where k is the scale factor, c is the shape factor, the wind speed for the time step i is represented by v_i, and the number of nonzero wind speeds by n.

The Weibull wind speed statistical distribution is a method from which the amount of wind energy yield can be calculated. Based on the wind turbine power curve (see Section 1.1) and the wind speed distribution from a site, the wind energy yield can be predicted for the length of time from which the statistical distribution is available.

2.1.4 Wakes

The wake is defined as the area downwind of the wind turbine that is affected due to the momentum extraction from the wind by the wind turbine (Landberg, 2015). As the wind passes through a wind turbine, the flow downwind will be affected due to the conversion of part of the kinetic energy into mechanical and electrical energy, decreasing the energy flux available to downwind turbines. As the flow goes away from the turbines, its kinetic energy gets mixed to the kinetic energy from the surroundings' flow. The velocity recovers with distance downstream at a rate that is dependent on the ambient flow turbulence (e.g. Ainslie, (1988; Sørensen and Shen, 2002).

Similar processes occur for large-scale wind farms, however the width and length of the wake from a farm of turbines are both larger than from a single wind turbine (Hansen et al., 2012; Crespo et al., 1999). The issue is up to which length will these wake last, and if there is another wind farm in a close proximity, how will this downwind farm be affected due to the upwind farm.

2.1.5 Wind Turbine Siting

As power producing systems, wind turbines play different roles, which can be as large farms, isolated systems or even as stand-alone sources of electrical power. Several issues have to be considered to identify areas suitable for wind farm development. Wind farm locations are normally defined in order to maximize the wind energy yield production from the farm. Minimisation of environmental impact and maximising economic viability are also important considerations. These activities can be divided into five stages (Manwell et al., 2002): Identification of high wind speed areas, Selection of candidate sites, Preliminary evaluation of candidate sites, Final site evaluation and Micrositing. The time and space resolutions range from low to high along these stages. From which the numerical weather prediction models can be applied for wind resource assessment. Wind speed results obtained from simulations, typically at

hub height, can be performed for any time of the year and time scale. These wind speed values can be obtained from minutes or days, while the spatial resolution can be set from hundred of metres up to kilometres.

2.1.6 Summary

In this Section, the characteristics of the wind have been described, including the method to calculate the performance of the wind turbines. A description of the wakes from the wind turbines over the flow has been performed, covering the stages to perform a successful wind turbine siting. Moreover, the application of the wind energy has been described and finally, the wind resource assessment methodology has been briefly introduced.

2.2 The Atmosphere

The following Section describes the structure of the atmosphere and provides an overview of the main features of atmospheric flow and the equations that are used to describe such flow. The processes that occur within the atmospheric boundary layer are explained and lastly, the general circulation models. Section 2.2.1 describes the atmospheric structure, composition and thermodynamics. Section 2.2.2 presents the components of the atmospheric motion. The structure of the atmospheric boundary layer is outlined in Section 2.2.3 and finally, Section 2.2.4 describes the general circulation models and their use

2.2.1 Atmospheric structure, composition and thermodynamics

An atmosphere that is formed from a mixture of gases surrounds the surface of the Earth. Its composition is a stable proportion up to 80 km of height. Since air is an extremely compressible fluid, about 50% of the mass of the atmosphere is located in the bottom 5 km. The atmospheric pressure has a logarithmic

decrease as the height increases, with a reference value of 101,325 Pa at sea-level elevation. The atmosphere's structure has four layers (Fig. 2.1); these are: the troposphere, which is the lowest, the stratosphere, the mesosphere and finally, the thermosphere. The first two are relatively warm, but the mesosphere is colder than the others.

In the troposphere, which is the lowest layer of the atmosphere, the climatic events and turbulence development are pronounced. Three quarters of the total atmospheric gaseous mass is contained in this layer. The temperature in this zone decreases with height at a rate of approximately 6.5°C/km (Barry and Chorley, 2009); this happens because of the air's compressibility and the increase of density with height, therefore, the air expands and its temperature decreases. Moreover, the atmosphere is principally heated by turbulent heat transfer from the earth's surface and not from direct absorption of solar radiation.

The next layer is the stratosphere, which continues above the troposphere to about 50 km and contains approximately 10% of the atmospheric mass. Considering that the stratosphere holds a great part of the total ozone in the atmosphere, it is in this layer where the absorption of the sun's ultraviolet radiation by ozone takes place. In this region, the air density is not as great as in the troposphere; for this reason, a small amount of heat absorbed per unit of volume, will increase the temperature in higher values compared to a different layer. Above this last layer the mesosphere is located. Here, the pressure is very low, with atmospheric values of 100 Pa at 50 km to 1 Pa at 90 km, moreover, here the average temperatures decrease to lowest values of 140 K at a height of 90 km (Barry and Chorley, 2009).

Finally, the upper layer is the thermosphere, where the density values are remarkably low. The composition of this layer is mainly atomic oxygen (O) and the temperature increases with height, because of absorption of ultraviolet

radiation absorption by oxygen; these values can reach theoretically from 800 to 1200 K at a height of 350 km (Barry and Chorley, 2009).

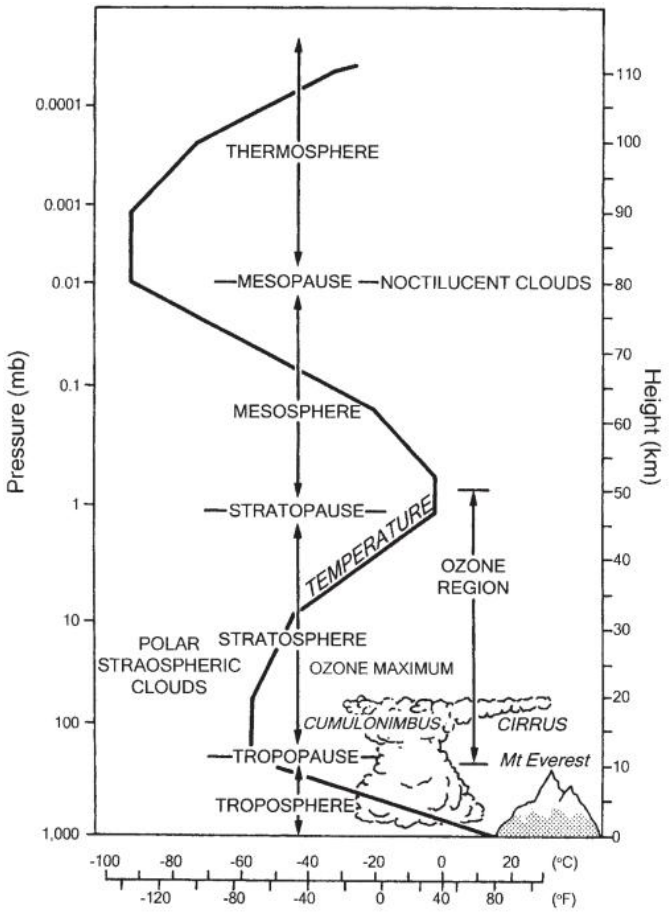

Figure 2.1 Generalized vertical distribution of temperature and pressure up to about 110 km. (Barry and Chorley, 2009)

2.2.2 Atmospheric flow

Movement of the air occurs mainly because of the constant change of velocity caused by the surface heating, resulting in mechanical turbulence. If the difference of the temperature with height differs from the adiabatic rate of temperature decrease, then fluctuations in the wind occur. Air composed mainly of nitrogen and oxygen, obeys fundamental laws as a feedback in the modification of pressure and temperature. Boyle's Law declares that, with a constant temperature, the volume (V) of a mass of gas changes in inverse proportion to the pressure (P), i.e.

$$P = \frac{k_1}{V} \tag{2.12}$$

where P is the pressure, V is the volume of air and k_1 is a constant value. Charles's Law states that, with a constant pressure, the volume changes according to the absolute temperature (T) quantified in degrees Kelvin:

$$V = k_2 T \tag{2.13}$$

where V is the volume of air, T is the temperature of air and k_2 is a constant value.

Considering these laws, it can be observed that the pressure, volume and temperature are coupled. In other words, changing the value of one of them will automatically produce an alteration in one, or both, of the others. Combining the gas laws leads to the following equation:

$$PV = RmT \tag{2.14}$$

where R is the gas constant for dry air (287 J/kg K), and m is the mass of air. To use this equation to analyse the atmosphere, the density (ρ = m/V) can be applied:

$$P = R\rho T \tag{2.15}$$

The energy input of the atmosphere comes from the Sun; this energy flux is determined by four causes: the solar energy output, the distance between the earth and the sun, the altitude of the sun and finally, the length of the day. Due to the high temperature of the sun (6,000 K) (Barry and Chorley, 2009), solar radiation is emitted in short wavelengths (4 nm). This energy flux varies during the day, and seasons of the year, due to the rotation and translation movements of the Earth. Its approximate value is defined between 1,366 and 1,370 W/m^2 (McIlveen, 1992). Due to the low temperature of the surface of the Earth, the energy flux that it irradiates is in a longwave radiation. This radiation is absorbed by the water vapour and carbon dioxide embedded in the

atmosphere, while they are transparent to the solar radiation; the accumulation of this heat causes the greenhouse effect.

A component of the atmosphere is moisture, which is water vapour and clouds; this amount of water is set mainly by evaporation, air temperature and the transport of moisture itself. One way to express the amount of water in the atmosphere is by the density of water vapour, which is the density of the molecules of water contained in the air. Another unit for moisture is the absolute humidity, defined by the quantity of water per volume of air, expressed by grams/m^3. In the meteorology field, the units in the mass mixing ratio are more convenient. In other words, the mass of water vapour is grams per kg of dry air. Another practical unit is the specific humidity (q), defined as the mass of vapour per kg of air, considering its moisture.

The following sets of equations are applied to describe the atmosphere:

Momentum equations for a spherical Earth:

$$\frac{\partial u}{\partial t} = -u\frac{\partial u}{\partial x} - v\frac{\partial u}{\partial y} - w\frac{\partial u}{\partial z} + \frac{uv\tan\phi}{a} - \frac{uw}{a} - \frac{1}{\rho}\frac{\partial p}{\partial x} - 2\Omega(w\cos\phi - v\sin\phi) + Fr_x \quad (2.16)$$

$$\frac{\partial v}{\partial t} = -u\frac{\partial v}{\partial x} - v\frac{\partial v}{\partial y} - w\frac{\partial v}{\partial z} + \frac{u^2\tan\phi}{a} - \frac{uw}{a} - \frac{1}{\rho}\frac{\partial p}{\partial y} - 2\Omega u\sin\phi + Fr_y \quad (2.17)$$

$$\frac{\partial w}{\partial t} = -u\frac{\partial w}{\partial x} - v\frac{\partial w}{\partial y} - w\frac{\partial w}{\partial z} + \frac{u^2+v^2}{a} - \frac{1}{\rho}\frac{\partial p}{\partial z} - 2\Omega u\cos\phi - g + Fr_z \quad (2.18)$$

where u is the component of the velocity in the x direction, v is the component of the velocity in the y direction, w is the component of the velocity in the z direction, x is the East–West space coordinate, y is the North–South space coordinate, z is the vertical space coordinate, t is the time, ϕ is the latitude, p is the pressure, Ω is the rotational frequency of Earth, Fr_x is the frictional acceleration in the x direction, Fr_y is the frictional acceleration in the y direction, and ρ is the density.

Thermodynamic energy equation:

$$\frac{\partial T}{\partial t} = -u\frac{\partial T}{\partial x} - v\frac{\partial T}{\partial y} + (\gamma - \gamma_d)w + \frac{1}{C_p}\frac{dH}{dt} \tag{2.19}$$

where T is the temperature, H is the rate of gain or loss of heat, C_p is the heat capacity at a constant pressure, γ is vertical lapse rate of temperature and γ_d is the dry adiabatic lapse rate of temperature.

Continuity equation for total mass:

$$\frac{\partial \rho}{\partial t} = -u\frac{\partial \rho}{\partial x} - v\frac{\partial \rho}{\partial y} - w\frac{\partial \rho}{\partial z} - \rho\left(\frac{\partial u}{\partial x} + \frac{\partial v}{\partial y} + \frac{\partial w}{\partial z}\right) \tag{2.20}$$

Continuity equation for water vapour:

$$\frac{\partial q_v}{\partial t} = -u\frac{\partial q_v}{\partial x} - v\frac{\partial q_v}{\partial y} - w\frac{\partial q_v}{\partial z} + Q_v \tag{2.21}$$

where q_v is the specific humidity, and Q_v is the gain or loss of water vapour through phase changes.

Ideal gas law:

$$P = R\rho T \tag{2.22}$$

In order to solve the set of equations (2.16 to 2.22), which are used to describe the weather processes, without excess numerical effort, certain approximations are considered. These typically include the hydrostatic, Boussinesq and anelastic. Each one of them simplifies the numerical processes required to represent the dominant physical processes allowing reliable forecasting results with the consumption of less computing resources.

The hydrostatic approximation does not consider the effect of sound waves, because it is not expected in the meteorological analysis; for this reason, the equation of motion (equation 2.18) is interchanged for an equation that only considers pressure terms related to gravity and vertical-pressure gradient. In a similar way, the Boussinesq and anelastic approximations directly filter the

sound waves from the equation (2.20). This is by decoupling perturbations of pressure from perturbations of density. These approximations are frequently considered for mesoscale and cloud-scale simulations (Warner, 2011).

The air in the atmosphere is driven by the differences of temperature between the equator and the poles. This heat energy is converted into kinetic energy, producing the movement of the atmospheric masses, which may be for periods ranging from seconds to weeks. Permanent activity in the atmosphere ranges from short scales and small breezes up to big storms throughout kilometres of distance, which may last days or up to a week. Despite the large movements that can occur in the horizontal direction, the vertical air displacement is limited because of hydrostatic equilibrium, defined as the balance between the gravitational force and the vertical pressure gradient. As a result, the horizontal component of wind speed can be orders of magnitude larger than the vertical component. This is typically the case with horizontal wind speed up to 100 times vertical wind speed, although exceptions may occur.

Due to heating of the atmosphere by solar radiation, potential energy is obtained, converted subsequently into kinetic energy, due to the ascending movement of warm air and the descent of cold air. Eventually, the air movement is affected by friction and turbulence. The atmospheric circulation is maintained by the balance of the kinetic energy generation and dissipation rates. Moreover, the distribution of the temperature at different heights sets the variation of pressure along this elevation: if the air column is warm, the high pressure structure will increase; on the other hand, if the vertical mass of air has a cold temperature, the low pressure system will be stronger; in this manner, the characteristics at the surface level are generally: low pressure with warm temperature and high pressure with low temperature.

By definition, an ideal air mass is a body of air with isobars (lines with the same pressure) and isotherms (lines with the same temperature) parallel to each other

and to the ground. The thermodynamic and dynamic processes created by the air movement change this parallelism. These processes could be air heating and cooling and the moisture transfer with the surface.

2.2.3 Atmospheric boundary layer

Meteorologically, the air movement is more affected by local phenomena, than with the global forces summarised in the preceding Section. During the day, the wind velocity patterns are set based on the small and large scale characteristics. However, at night, under normal conditions, the velocity decreases because of the reduction of heat transfer between the surface and the air. Within the planetary boundary layer, with an approximate thickness of 1 km, different physical processes occur, which permit mass, momentum and energy transfer between the surface and the lower atmosphere. In this layer the diurnal heating and nocturnal cooling causes airflows to occur and the friction with the surface creates the logarithmic vertical velocity profile. The importance of these flows depends on the amount of terrestrial energy and how it changes its value and direction, whether it is day or night, throughout the year.

The horizontal movement close to the earth is defined for the most part by four physical phenomena, these being the pressure-gradient force resulting from the change of pressure as a result of the variation of the surface heat transfer, and, as stated before, air density and pressure; the Coriolis force, which is the effect of the rotation of the earth applied to the movement of the air; the centripetal acceleration, which is the force towards the centre of rotation when following a curved path; and finally, the frictional forces between the surface of the earth and the wind; the thickness of the atmosphere affected by friction is defined as the planetary boundary layer (PBL), which shows an exponential decrease of wind speed close to the surface.

To represent the meteorological systems on a global scale, the flow divergence, vertical motion and vorticity play significant roles. The divergence is presented

when the distance between the streamlines increases and there is vertical stretching of the profile, which is caused by the compressibility of the air; it can also exist as convergence, when the streamlines show confluence in a section and also they shrink their vertical profile, compressing the air mass.

The vertical motion is represented by the air flow up and downward in order to compensate the horizontal flow at lower heights; regarding the system pressure, in low pressure systems, air converges near the bottom and tends to go upward, while in the upper layers it diverges, and vice versa for high pressure systems; however, on a large scale, this vertical motion is very slow compared with the horizontal movement.

Finally, vorticity refers to the rotational movement of the fluid. This motion has three components: magnitude, direction and sense of rotation, which is based on the earth's rotation, if they go in the same sense, it is positive; if not, it is negative. This flow may be caused by the curvature of the streamlines, by the unbalanced distribution of the wind's current strength, or because of both.

2.2.4 General Circulation Models

The general circulation model solves the dynamic and thermodynamic processes, including the interchange of mass and radiation with the surface; the main ways to discretize the governing equations of the atmospheric phenomena to find a solution are the finite difference, the finite element and the finite volume methods:

Finite difference methods approximate the field of a variable from the differential equations, in order to comply with the function of its derivatives, considering the values at their end, also known as boundary conditions. This is done using finite difference approximations, which replace the derivatives in the governing equations.

In the finite element approach, the computational domain is divided into finite adjacent domains, defined as elements, where the dependent variables are calculated through spatially varying functions, including time-dependent coefficients.

Finite volume methods employ three-dimensional, finite control volumes to balance the mass, energy and momentum fluxes. A mesoscale convective system (MCS) is defined as a mass of air with geographical dimensions of tens of kilometres and a time scale of a few hours. A large number of cells may be located in a MCS, in the direction of a large-scale wind.

In order to represent the values of each grid point over the studied domain in an accurate way, which may range from tens of kilometres to hundreds of metres, there are different methods to reduce the global information to a smaller scale. As an example, the studied domain can be nested on a global model database, from which the initial and boundary conditions will be taken from a global scale and re-calculated, using the model, to the desired spatial scale applied in the local domain to solve the processes considered for simulation. Global databases such as the Global Forecasting System (GFS) (NCWCP, 2013), the North American Mesoscale (NAM) model (Mesinger et al., 2006), and the North American Regional Reanalysis (NAR) (NESDIS, 2013) supply the meteorological information every 3 or 6 hours, covering temperature, pressure, humidity and wind on a worldwide scale.

The results of the simulations obtained are averaged over each node of the domain, because the meteorological characteristics for a specific point within the node may differ for the measured local values.

The atmospheric circulation processes can be described using different numerical models. Some of these models are tools able to calculate the convective and radiative mechanisms, and energy balance, and can be coupled with regional scale models. In the 1960s, numerical models were only applied to

forecast the weather. More recently, their features have been improved to predict anomalies in weather and also to analyse the current and future changes in the climate around the world.

Nowadays, there are different tools to perform weather prediction analysis, which are available to the meteorological community and the general public. Weather can be predicted for a period of 1 to 2 hours, for a week, from season to season and even for years. The characteristics of the models to predict the weather over different time horizons vary. Some models are suited to a national scale, like 1,044 km by 884 km (Schultz et al., 2014), while others are applied to a much smaller region or zone.

The opportunity to operate ever more powerful computers, and the development of more accurate atmospheric models, have led to the inclusion of specific features for these models; some of these are applied in the agriculture, health and safety, transport, military, environmental and renewable energy sectors.

2.2.5 Summary

This Section has provided an overview of the composition of the atmosphere and how it responds to different phenomena, considering the Earth's rotation, heat transfer from the Sun, ground heat absorption and release to the lower atmosphere. The equations by which these effects are governed have been given, as well as a brief description of how general circulation models can be applied to solve these equations.

2.3 Numerical Weather Prediction Models

The development and principal features of numerical weather prediction models are described in this Section. This includes the methodology for the numerical solution of the conservation equations and a description of the initial

and boundary conditions required. A description of the surface and boundary layer processes is also given. The importance of performing a validation of the model and the results is highlighted, and finally, a description of the methodology to design sensitivity analysis cases is presented.

Section 2.3.1 presents a background and introduction of the numerical weather prediction models. Section 2.3.2 describes the numerical solution of the governing equations of Section 2.2.2. Section 2.3.3 covers the explanation of the boundary and initial conditions for the model. Section 2.3.4 describes the processes modelled at the surface and boundary layers. Section 2.3.5 includes the importance of the model verification. And finally, in Section 2.3.6 the steps to design of sensitivity analysis are explained.

2.3.1 Introduction

Weather forecasting models have been developed since the 1850's, when weather characteristics were collated from disparate locations via telegraph, analysed and presented as synoptic charts, which defined the distribution of the weather characteristics over the domain analysed. Weather forecasts are categorized as short-range: those that last up to three days; medium-range: those that predict up to two-weeks of weather; and long-range for those which forecast a month or up to a season of the year (Barry and Chorley, 2009).

The atmospheric circulation processes can be described using different numerical models. Some of these models are tools able to calculate the convective and radiative mechanisms, and energy balance, and can be coupled with regional scale models. In the 1960's, numerical models were only applied to forecast the weather. More recently, their features have been improved to

predict anomalies in weather and also to analyse the current and future changes in the climate around the world (Lo et al., 2008).

Various models are available for simulating atmospheric processes. Reviews of atmospheric models are given by Hartmann (1988), Machenhauer et al. (2009) and Skamarock and Klemp (2008). Numerical models range from simple approaches that balance the fluxes at a single spatial co-ordinate, up to general circulation models that solve the momentum and continuity equations governing fluid flow with appropriate boundary conditions within three-dimensional domains.

Many industries are reliant on accurate weather forecasting. Agriculture depends on the rain forecasts, while the energy produced from the utilities is based on the daily temperature prediction; furthermore, sailing and fishing boats rely on the meteorological storm prediction. Additionally, the supermarkets base their food stock on weather forecasting as well (Inness and Dorling, 2012). In order to provide a forecast of the atmospheric conditions, a numerical weather prediction (NWP) model is applied; which requires observed data to forecast the weather based on the computerised representation of the atmosphere. NWP models are useful tools to accurately solve the equations that describe the meteorological phenomena.

Foley et al. (2012) described the recent growth of global installed capacity of wind turbines and performed a literature review on the methods of and advances in forecasting wind power generation. A supplementary approach to NWP is ensemble forecasting, which considers the results of different NWP models to assess the differences in the results provided by them. Methods have been used to analyse data from meteorological databases, grouped into dynamic and kinematic models. Weather resources can be analysed statistically, linking the historical energy production with the weather. Finally, to analyse the accuracy of the results, different methods can be applied to quantify the

difference between the predicted and the measured values, these being the mean absolute error, the correlation coefficient and standard deviation of the errors, among other methods. The authors concluded by explaining that one way to promote wind energy development is by increasing the NWP models' accuracy, developing more reliable and easier tools to forecast the wind power energy production.

Miller et al. (2013) reviewed the most recent advances in numerical simulation applied to wind energy. The topics covered are the wind turbine micro-siting and optimization of a wind farm layout, the simulation of wind flow and the behaviour of the atmospheric boundary layer, flow modelling of wind turbine effects in a precise manner, and finally, the trends of the computing tools applied to the numerical simulation. The authors explained the steps followed to select the optimal wind turbine location and described the distribution in a wind farm as micro-siting, which can be developed through NWP and Computational Fluid Dynamics (CFD) methods by studying the wind flows and their interaction with complex orography. Moreover, models such as WRF, can be used together with different tools to analyse the cost, distribution and inter-turbine effects within the domain. The authors referred to a study performed by Liu et al. (2011), where the WRF was coupled with a LES model to forecast and describe the wind resource, aided with the nested grid technique. Furthermore, they highlight the importance of modelling the atmospheric boundary layer to calculate the wind power generation. This work can be done with the aid of CFD, predicting the effects of the wind turbines on the wind flow in a precise way. In addition to this, wind forecast models describe the natural flow phenomena on a large scale, and by connecting these two tools, the results obtained are better than analyzing separately.

The opportunity to operate ever more powerful computers and the development of more accurate atmospheric models, have led to the inclusion of

specific features for these models. Lately, these have been applied in the renewable energy sectors, particularly for the wind resource assessment and wind turbine representation (Jiménez et al., 2015).

2.3.2 Numerical solutions to the equations

The conservation equations (2.16 to 2.22) are solved numerically. The numerical approximations considered to obtain a solution for the governing equations are very important topics in weather forecasting. Four of the main frameworks to work with the modelling of the space dependence, in the non-linear partial differential equations of atmospheric dynamics and thermodynamics are: the finite difference (LeVeque, 2007), spectral (Le Matre and Knio, 2010), finite element (Reddy, 2014) and finite volume (Versteeg and Malalasekera, 2007).

In order to obtain a numerical result from the model, the equations must be solved for every node of a domain for each time step, until the converged result is obtained. If the domain contains a very large number of nodes and the time step is very small, the simulation will take longer than if the domain is not highly refined and the time step is not particularly small. Based on this situation, the development of numerical methods to obtain quick and accurate solutions has been the main interest to NWP researchers.

The points of the model where the equations are solved are located with different distances between them, in quasi-regular grids; this is because latitude-longitude coordinates might be used, or due to the implementation of a higher density mesh, which might be required over important or strongly graded places. Within the computational mesh, the scales of the horizontal domain are larger than for the vertical domain. The spacing distribution of the vertical levels may follow a cosine or logarithmic distribution, to increase the resolution within regions of high velocity gradient, such as near the surface.

For the wind resource assessment, the spatial scales used range from 4 km (Deppe et al., 2013) up to 333 m (Horvath et al., 2012). To save computational

resources, these fine resolutions domains are nested within a coarser resolution domains. These lower resolutions domains capture initial and boundary conditions over a bigger area to bring it to the nested domain. The recommended numerical time step for the computational solution, is six times the size of the cell in km, e.g. 1 km cell will requires 6 seconds time step, 500 m cell, will require 3 seconds time step. Throughout the increase of the resolution, the time steps decreases linearly, in such way, the time for solving a simulation will increase as well, for which the computational cost, will be higher.

Finite difference methods can be utilized to approximate the time and space derivatives; these approaches add non-physical properties to the problem solution and help to obtain a stable computation, limiting the time step.

The following flow diagram (Fig. 2.2) describes the main activities to set up a model; however, there are more points, such as the parameterization. For the following steps, it is considered that the time step has been set already for the simulation.

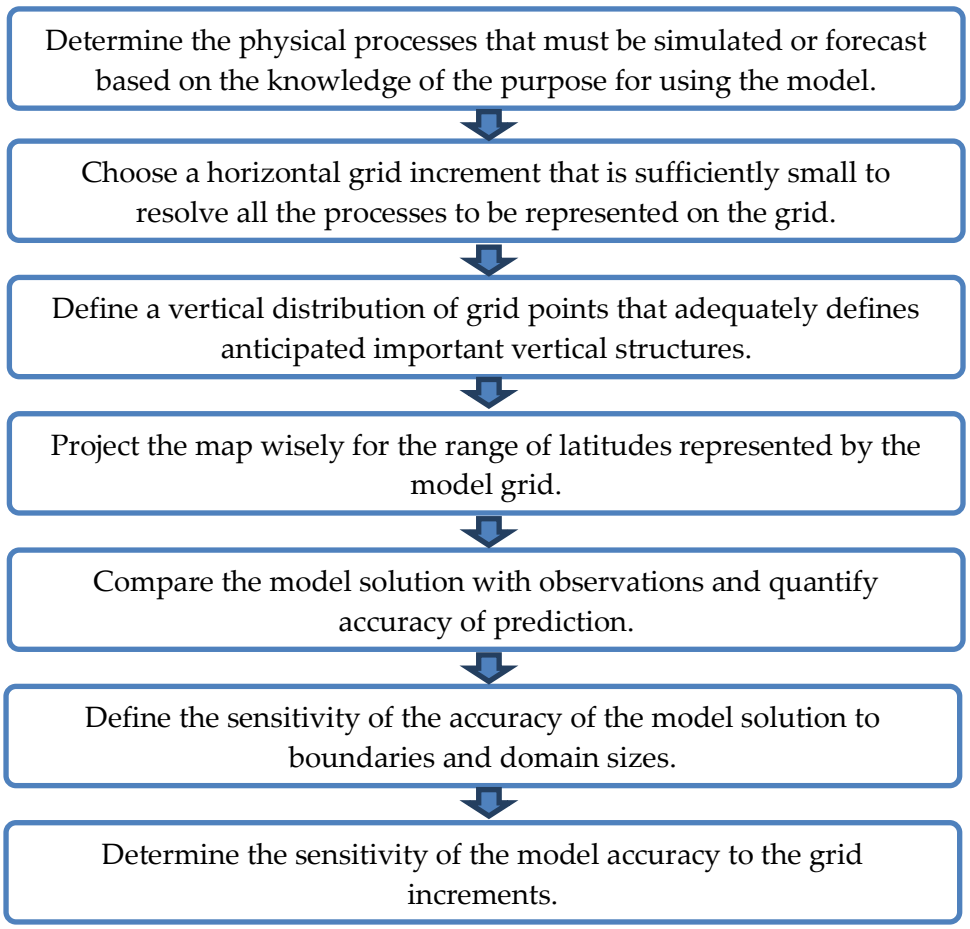

Figure 2.2 Flow diagram of main stages in development of NWP model (Warner, 2011).

2.3.3 Initial Conditions

In order to solve the governing equations (2.16 - 2.22), the initial and boundary conditions must be provided. The initial conditions are the values of dependent variables at the beginning of the simulation; this process is also referred to as initialization. The values selected to initialize a model must accurately represent the characteristics of the local weather. The temperature, pressure and velocity fields should be dynamically consistent, in other words, they must accomplish with a hydrostatic and geostrophic balance.

The meteorological information provided for the model initialization can be taken either in situ or remotely. In situ values comprise the use of sensors to

measure the variables locally; whereas, remote measuring considers the use of devices which evaluate the resource from a distance, aided with active or passive mechanisms. Weather stations measure the site temperature, humidity, pressure, wind speed and direction, as well as precipitation. The remote passive methods use the analysis of natural radiation emitted by the flow. Furthermore, the remote active methods are based on the assessment of the response of the weather to radiation emitted from the device to the atmosphere.

The tools to obtain initial meteorological conditions have been improving in accuracy. However, soil measurements have not been as developed as the rest and they affect the development of the vertical velocity profiles at the planetary boundary layer.

Numerical weather prediction models have improved their proficiency in representing the small-scale atmospheric phenomena, which affect the large-scale circulations over the evolution at bigger scales. Unfortunately, these small scale processes such as sea winds, rainstorms and snow bands, among others, cannot be quantified through weather stations in order to be included as initial conditions in the model.

This initialization can be implemented in two ways, called static initializations and dynamic initializations. Static initialization takes the initial data and begins with the simulation process once it has been located in the model grid; it is also referred as "cold start" (Warner, 2011). Dynamic initialization simulations are performed in the same way similarly to those with static initialization, but from 12 to 24 hours in advance of the desired time for the forecast to begin. This development time (Warner, 2011) allows the model to run for a pre-forecast period. The variables initialized are temperature, velocity field (u, v), relative humidity, terrain elevation, surface pressure, sea-level pressure, soil moisture, and temperature and snow depth.

2.3.4 Boundary Conditions

As the computational domain is placed within sides, it is required to define the values for the dependant variables over the border. These values are also named boundary conditions, and are defined at the lateral, top and lower boundaries' conditions for the solution of the model equations.

From the boundary conditions, the lateral values are used to limit the domain in the horizontal axis. To avoid the influence from these boundaries over the results from the simulation, it is recommended to locate the boundary as far as possible from the part of the domain of interest. To increase the size of the computational grid is one technique to reduce the effect from the lateral boundary. These values must be designated outwardly for each of the dependent variables at this location. In the research field, these values are taken from meteorological archives, larger scale simulations or global observations.

The top boundary conditions, define values at the highest horizontal layer of the domain. In a similar way as the lateral boundary conditions, they have to be defined as far as possible from the elevation of interest. One method is the rigid top, which defines the vertical velocity as zero, however this boundary constrains the flow. Another top boundary condition is the impermeable surface, which moves based on the atmospheric motion and it is considered as a more realistic top boundary condition. In contrast, the porous top boundary condition, allows the mass to flow through it, however this boundary is not applied within the numerical weather prediction models.

From the three types of boundary conditions, the bottom condition is the one with a physical meaning. Besides, the fluxes through it (i.e. heat and moisture) are important to define the low atmospheric flow, and accurate representation of the ground characteristics is crucial for its accurate representation.

2.3.5 Spatial discretisation

Domain size and resolution in NWP models is defined by three constraints: The dimensionality of the forcing, spatial scale of the physical response of the forcing and the computer resources available.

For the solution of the fluid flow equations over the earth, different approaches have been developed to set and arrange grid points in an organized manner over the domain considered for study. These methods deal with the use of map projections, the employment of grids based on the latitude and longitude and spherical geodesic meshes. These methods vary in their application according to the size of the domain and the need to reduce the difficulty of the code modification for the research field. These grids may have or lack structure. Grids where the arrangement of cells organized in a periodic sequence in two or three dimensions, known as structured grids; whilst unstructured grids are represented by a group of elements, such as triangles, which are unevenly distributed.

The grid resolution used over the studied domain requires a higher density at important locations, such as complex terrain or where steep gradients are located, where small-scale processes occur; in the case of the meteorological forecast models, the grid resolution is increased when a specific meteorological characteristic is studied, therefore, the resolution of the mesh nodes is intensified at these locations.

An approach used to obtain different horizontal grid resolutions is to insert a high resolution domain, consisting of a limited area within a global model containing a lesser resolution mesh; in these models, the global domain, which is solved first, provides the boundary conditions for the inner domain, which may have a mesh density from three to five times higher. However, most of the models have the same number of vertical planes for the entire domain, global and limited area.

2.3.6 Modelling surface and boundary layer processes

The description for some physical processes in the meteorological analysis demands a more elaborate procedure and increases the complexity of the model. In these cases, the parameterization is the description of a physical process, which is not resolved directly on the scales of the computational domain used, considering the link to dependent variables solved on the mesh arrangement.

Such parameterization is performed with three main intentions; these processes are not well known or understood to be represented directly with a physical connection, the scale in which the process is performed is finer than the scale used for the model, and finally, the computational resources needed to calculate these processes in a more exact way may be extremely large.

The parameterizations are for processes which are from a smaller scale compared against the domain resolution, or which are too complex to model, computational expensive, or cannot be solved directly from the model.

The most important processes in weather prediction are the physically interactions, such as turbulent heat transfer, water vapour and momentum mix (Nakanishi and Niino, 2006). Additionally, the representation of the moisture convection (Park and Bretherton, 2009), along with processes to describe the radiative heat transfer from the sun, atmosphere and surface (Dudhia, 1989) require a considerable arithmetical analysis compared to the remaining variables (Stensrud, 2009).

For the case of convective parameterizations, a considerable number of approaches and assumptions to the problem are taken into account (Warner, 2011); in order to achieve accurate results, these must be applied to match the problem requirements.

Some parameterization cannot be generalized for all the same circumstances, such as geographical area or parameter ranges. Not all physical processes can

be reproduced using numerical models, whether a fine resolution is applied or not. Nevertheless, parameterization is the method to describe these processes, which are essential to obtain proper results and cannot be solved with the numerical models. The importance of these schemes relies on the vertical linking between them to quantify the variables of the model as accurate as possible.

These parameterization schemes are applied to land surface processes, vegetation effects, planetary boundary layer and turbulence mechanisms, to represent the convection and microphysics development, such as to apply the effects of the radiation through clear and cloudy skies. For example, the surface heat flux is heavily affected by the vertical wind profile over the surface. To quantify these heat transfer mechanisms between the surface and the atmosphere, some approaches consider the surface temperature, while others only deal with the air temperature (Stensrud, 2009). These two schemes satisfy mass continuity, although the results obtained will vary. This is an example of the importance of identifying the appropriate parameterization scheme to obtain accurate results from the numerical model.

The vegetation located over the surface can be parameterized, in order to analyse appropriately. Work by Henderson-Sellers et al. (1993) analysed 25 land surface schemes to compare the results against the local measurements, finding difficulty in representing the effects of the vegetation over the atmospheric flows accurately. Consequently, it is important to specify correctly the land surface model, taking into account the local characteristics of the terrain.

To represent adequately the development of the planetary boundary layer through time and space is essential. Physically and numerically, it leads to weather phenomena which are representative of the atmosphere (Nakanishi and Niino, 2006). As the atmospheric changes are due to the turbulence effects, it is quite complicated to represent them computationally. During the daytime,

the heat flux between the surface and the lower atmosphere builds the turbulence; subsequently, at night this turbulence is caused by the mean wind profile shear and it changes abruptly. As these turbulence processes are represented by the planetary boundary layer, it is essential to select an appropriate scheme to obtain results that reflect reality.

The boundary layer behaviour is determined by the surface heat flux. During the day, the heat source is governed by the solar radiation; meanwhile, during the night, the boundary layer and wind profile changes are ruled by the long wave radiation interchange from the surface and the atmosphere. As with the other parameterization schemes, the selection of an appropriate scheme for the boundary layer which will provide reasonable results is not an easy task.

Parameterization schemes for either the short and long wave radiation contributions have been developed to provide refined and low-cost values. For each of the domain cells, these schemes calculate the net surface radiation, to quantify the surface heat flux (Dudhia, 1989). Moreover, the quantity of radiation absorbed will be defined by the geographical characteristics of the surface and sky clearness. Any variation on these fluxes will affect the structure and depth of the boundary layer, thus applying appropriate radiation parameterization schemes is highly significant in favourably representing the atmospheric phenomena using the numerical weather prediction models.

2.3.7 Model Validation

The importance of a wind resource assessment analysis lies in the accuracy of the forecast. For this reason, to obtain confidence on predictions, for a particular location and region, the validation is typically performed against full scale measured data. It also helps to improve the development of the model

If the model provides good agreement with the measurements, it can be used at times when there are no measurements available. When parameterizations are applied, the selected arrangement of these schemes must be compared in order

to be validated. For a comparison between different models, it is necessary to verify the results objectively, so that the advantages and deficiencies of the models can be understood.

The validation of a numerical simulation by observations can be listed in two groups: subjective evaluation or point to point quantitative validation. For the subjective verification, a qualitatively comparison is performed from the predicted values against the observations. Whereas, if measured data is available, the point to point validation includes the Root Mean Square Error analysis from the number of predicted values and the results to define the skill of the model (Pielke Sr, 2013).

2.3.8 Design of sensitivity analyses

Aspects from the meteorological phenomena, such as wind resource assessment, are frequently studied from the numerical weather prediction model simulations for short time intervals. One of the reasons is to have a better understanding of the wind speed and power predictability, which is based on the parameterisation models and/or initial and boundary conditions.

Additionally, it is important to compare the models available, in order to select the most accurate to simulate the wind turbine performance for the local conditions. Doing this will save time and money.

To perform these analyses, a selection of meteorological datasets and parameterization models, amongst other variables, is performed. Then, simulations for all the combinations of this selection are performed. Throughout these sensitivity studies, the effect of these combinations, to reproduce certain variable at a given point or area of interest can be evaluated.

The literature has to be reviewed in order to identify the impact of the mesh resolution, numbers of domain, parameterization models and length of the

simulations. From this review, the most representative options can be shortlisted and evaluate the amount of the combinations amongst them.

Besides, the methods to validate the results have to be review, to identify the best statistical tools to define the accuracy of the model part of the sensitivity analysis. These can include comparisons from punctual values, time series or statistical distributions. Performing a sensitivity analysis increases the reliability from the results.

2.3.9 Summary

This Section has presented a background to numerical weather prediction models, the methodology to solve numerically the governing equations of atmospheric flow and the boundary and initial conditions required for these models. The processes modelled at the surface and boundary layers are described. The importance and a method to verify the model is included and finally, the design of sensitivity analyses is explained.

Chapter 3 Literature Review on Wind Resource WRF Model

This chapter provides a review of the literature concerning the use of the Weather Research and Forecasting model (WRF) for wind resource assessment. Background to this Numerical Weather Prediction (NWP) model is presented, followed by a review of the WRF model's accuracy for wind resource assessment. The computational size, resolution and meteorological datasets for initialization are subsequently considered. The parameterization models to configure the model are discussed, with a particular focus on suitability for onshore regions with large variations of terrain elevation. Finally, the models to represent the effects from the operating wind turbines over the flow are described. From this review, configurations of the WRF model suitable for wind farm energy yield simulation are outlined.

3.1 Introduction

Kimura (2002) described the background of NWP and the WRF model, by recounting their historical developments. Nowadays, these models are widely used in terms of purposes and locations, to describe the weather through computational analysis. Due to activities such as fishing and war, weather prediction gained more importance and different methods were developed based on meteorological observations. An early study of NWP was by (Richardson, 1922) who solved the Navier-Stokes equations on an atmospheric scale based on initial conditions from meteorological observations. Later, von Neumann developed ENIAC in 1950, the first electronic computer, and with the aid of both this computational resource and the progress in weather description, he succeeded in providing a one-day-ahead forecast. Since this achievement, the NWP method has been studied and developed by meteorologists. Advances of computer resources have enabled forecasts over intervals from two days up to 50-years (Clark et al., 2001).

Lynch (2008) reviews the history of weather prediction and climate modelling methods from 1890 to 2000, namely, the proposition of a mathematical approach to perform weather forecasting, which later included the use of observed data as initial conditions, followed by the use of laws of motion to model the weather behaviour. The work by Richardson (1922) provided the basis for the actual weather forecast simulations. Lynch then explained different stages of the modern NWP method. After Richardson's work, very important progress was obtained in different areas: the theoretical basis of atmospheric flows, numerical analysis methods, metrology, and computational techniques. All these improvements were used together by von Neumann (Macrae, 2000), who obtained results from Richardson's model of computational analysis. From whom a revolutionary development was describing the situation of the NWP methods. Existing models are widely used to describe daily weather conditions, both globally and locally. Finally, he described the WRF as a mesoscale NWP method able to provide accurate results for either operational or research needs, which can be applied in a range from metres to kilometres.

Studies covering statistical analyses of the wind resource, notably the Weibull distribution describing probability of occurrence of wind speed, are described in Section 3.2. The influence of alternative parameterization models on the accuracy of wind resource assessments is presented in Section 3.3. The analysis of the accuracy from different initialization data is presented in Section 3.4. Moreover, work covering the impact of the complex terrain on wind speed prediction accuracy is reviewed in Section 3.5. Section 3.6 presents published works which are focused on the use of the NWP models and the WRF model for the wind resource assessment. Examples of work on the computational domain and the resolution for this are summarized in Section 3.4. The evolution of the wind turbine parameterization models within WRF is described in section 3.8. Finally, the summary of this review is presented in Section 3.9, and the

configuration of WRF models which have been found to be suitable for wind resource assessment are tabulated in terms of their accuracy.

3.2 Probability Distribution of Wind Speed

As it was mentioned in Section 2.1.3, the Weibull probability density function allows to describe the wind speed distribution and the occurrence of mean values. This function requires the definition of two parameters, the shape factor, *k*, and the scale factor, *c*. Both factors are functions of the mean wind speed and the standard deviation.

The analysis of the scale and shape parameters for the Weibull distribution is very important for the wind energy assessment, and finding the method which provides the parameters for an accurate statistical description is important as well.

From the literature reviewed, six methods have been found, which are: the moment method, which is an iterative method. The empirical method, which is a special case of the moment method. The graphical method, which calculates the least squares concept. The modified maximum likelihood method, which is applied for data in the frequency distribution format. The energy pattern factor method, which applies the wind speed cubes and cube of the mean wind speed to calculate the shape parameter. And the maximum likelihood method, which is a method that needs extensive numerical iteration. Work on the literature has been found, were the accuracy of the Weibull distribution, from the scale and shape parameters calculated from different methods, has been evaluated.

Seguro and Lambert (2000) compared three methods, from which identified that the maximum likelihood method should be used with time series wind data.

Carta and Ramirez (2007), performed an analysis of the three methods more frequently used to estimate the five parameters of the two-component mixture

Weibull distribution. They concluded that if the data is independent, then the use of the maximum likelihood method is recommended.

Chang (2011) compared six numerical methods for the estimation of Weibull parameters for wind energy application. The results showed that, simulating random variables for the estimation of the Weibull parameters, the graphical method is the worst, followed by the empirical and energy patterns factor methods. Finally, they conclude that the maximum likelihood method performs in a better way than modified maximum likelihood and moment methods.

Soler-Bientz, et al. (2010), developed a study of the long-term wind characteristics of the Yucatan Peninsula in Mexico. The wind speed distribution was fitted with the Weibull distribution, and concluded that the scale and shape factor from the maximum likelihood method showed a good agreement.

From this review, it has been shown that the maximum likelihood method is suitable to calculate the scale and shape parameters from the Weibull distribution in order to represent the wind speed statistical distribution. In Section 2.1.3, the equations (2.8) and (2.9) present the Weibull and cumulative function, and equation (2.10) and (2.11) describe the scale and shape parameters, respectively.

3.3 Parameterisation models

When small scale physical processes are too expensive or complex to model, they can be represented within the code by algorithms or statistical methods that relate the variables calculated to their effect on the flow. For the case of convective parameterizations, a considerable number of approaches and assumptions to the problem are taken into account. The results provided from alternative parameterization models will differ, due to the local characteristics of the weather, topography and depending on the accuracy with which the simulated physical process is described.

From the literature, different WRF wind resource assessments have considered different numbers of domains and sizes, as parameterization models for the Planetary Boundary Layer, Surface Layer and Land Surface Model. The PBL describes the vertical profile of heat and moisture fluxes through the vertical extent of the boundary layer region (Section 3.3.1). The surface layer and land-surface models specify the ground friction and heat and moisture fluxes from the surface into the lowest levels of the atmosphere (Section 3.3.2). Additionally, there are different meteorological databases that can be used to set the initial conditions for the simulations. The following is a description of the literature review performed to describe the different assumptions used in published work to find the preferred parameterization model configuration for wind speed prediction at onshore locations with relatively complex terrain.

Considering different Land Surface Model (LSM) and Planetary Boundary Layer (PBL) Model implementation, Chavez et al. (2012b) analysed different models' results for a wind resource forecast in the northwest of Mexico. The models used were from the National Centre for Atmospheric Research (NCAR), the North American Regional Reanalysis (NARR) (Mesinger et al., 2006) and North American Mesoscale Analysis (NAM-ANL)(Rogers et al., 2009) , and from the University Corporation for Atmospheric Research (UCAR), the Weather Research & Forecasting Model (WRF-ARW) (Skamarock et al., 2005). The WRF code was parameterized with the following models: Land Surface Model, Noah Land Surface Model; Planetary Boundary Layer, Mellor-Yamada-Janjic; and finally, Cumulus Parameterization, Kain-Fritsch scheme. Two domains were selected, 9 km and 3 km, with 31 vertical levels, from which four were located in the first 150 metres. The length of the simulation was 72 hours, with a spin-up of the first twelve hours. For the 10 metre height wind speed forecast, all initialisation datasets resulted in overprediction of wind speed. However, the NAM-ANL provided quite precise wind distributions, with a bias range of 0 to 1 m/s. Nevertheless, for the 80 metre height wind speed forecast,

the WRF model forecast the zone with a high wind in the northwest described as “La Rumorosa”, compared with the other two models, NAM and NARR, which underpredicted this area.

3.3.1 Planetary Boundary Layer Model

The planetary boundary layer (PBL) model calculates the sub-grid-scale fluxes along the vertical axis. The vertical profiles of these fluxes within the boundary and stable layers are defined from the PBL, to characterize the temperature, moisture and horizontal momentum. These schemes operate only on the vertical dimension.

To represent the Planetary Boundary Layer (PBL) WRF provides 13 PBL schemes, the Yonsei University scheme, Mellor-Yamada-Janjic (MJY) scheme, MRF scheme, ACM2 PBL, Quasi-Normal Scale Elimination PBL, Mellor-Yamada Nakanishi and Niino Level 2.5 PBL (MYNN Level 2.5), Mellor-Yamada Nakanishi and Niino Level 3 PBL, BouLac PBL, UW (Bretherton and Park) scheme, Total Energy - Mass Flux (TEMF) scheme, LES PBL, Grenier-Bretherton-McCaa scheme, and finally, the Topographic correction for surface winds. Of the PBL models reviewed, the most widely used is the Mellor-Yamada-Janjic scheme, even for small domain sizes (Chin et al., 2010; Horvath et al., 2012). Nevertheless, the MYNN Level 2.5 has shown a better wind speed vertical profile for larger domains (Wang et al., 2011; Draxl et al., 2010) work from (Deppe et al., 2013) calculated a mean absolute error for the wind speed of 1.43 m/s for average values of 10 m/s from the MYNN Level 2.5 PBL.

3.3.2 Land Surface Model

The function of the land surface models (LSM) is to calculate the heat and moisture fluxes from the surface to the lowest layer of the atmosphere. This balance is performed based on the radiation, precipitation and the characteristics of the surface. These heat and moisture fluxes are transferred to the planetary boundary layer (PBL) throughout the surface layer model (SL).

In order to describe the effect at the land surface, the seven parameterization models available in WRF are: the 5-layer thermal diffusion, Noah Land Surface Model, RUC Land Surface Model, Pleim-Xiu Land Surface Model, Noah-MP (multi-physics) Land Surface Model, SSiB Land Surface Model, and CLM4 (Community Land Model Version 4), which vary the effects between the land and the atmosphere. Taking into account the literature reviewed (Deppe et al., 2013; Carvalho et al., 2012), the Pleim-Xiu LSM has been demonstrated to provide better prediction of wind speeds for the Southern California area compared with the Noah LSM and 5 layer thermal diffusion scheme (Wilson, 2012). However, considering a small domain configuration, the RUC Land Surface Model has provided a RMSE of 2.5 m/s the corresponding mean wind speed is not reported (Chin et al., 2010).

3.3.3 Surface Layer Model

The surface layer schemes (SL) define friction velocities and exchange coefficients at the surface, for the LSM to calculate the heat and moisture fluxes, and provide the surface stresses characteristics to the PBL, it is worth mentioning that the representation of these surface mechanisms is an indispensable element of the weather simulation code. WRF provides 8 parameterization models to represent the surface layer characteristics. These models are: MM5 Monin-Obukhov, Eta similarity, Pleim-Xiu surface layer, QNSE surface layer, MYNN surface layer, TEMF surface layer, Revised MM5 surface layer scheme and Land thermal roughness. The MM5 Monin-Obukhov was found to be the most representative model for complex terrain (Hu et al., 2013), and within a domain with a more refined mesh (Carvalho et al., 2012).

3.4 Meteorological datasets for Initialisation and Boundary conditions

In order to solve the governing equations (2.16 – 2.22), the initial and boundary conditions must be provided. The initial conditions are the values of dependent variables at the beginning of the simulation, this process is also referred to as

initialisation. Performing a proper initialization will enable an accurate forecast to be obtained. Different sources of meteorological information were considered from the works reviewed, the most common was the Global Forecast System (GFS) (Deppe et al., 2013; Hu et al., 2013; Bei et al., 2013; Draxl et al., 2010; Hu et al., 2010), as well as the North American Regional Reanalysis (NARR) (Chavez et al., 2012a; Chavez et al., 2012b; Horvath et al., 2012; Capps et al., 2012; Wilson, 2012), and finally the North American Model (NAM) (Deppe et al., 2013; Wilson, 2012; Gilliam and Pleim, 2009). Another study applied the National Centre for Environmental Prediction/Department of Energy's (NCEP/DOE) database (Zhang et al., 2009). Deppe et al. (2013) comparing the GFS and the NAM models in the centre of the United States; in their results, the NAM initialization provided a lower mean absolute error. However, for the Southern California area, Wilson (2012) compared NAM and NARR models, finding the NARR the best option based on the temperature, wind speed and dew point bias.

3.5 Terrain complexity

Chenghai et al. (2011) analysed the low-level wind behaviour in a complex terrain through the WRF model. They considered four different PBL schemes, which were the MYJ (Mellor-Yamada-Janjic (Eta) TKE scheme, and Monin-Obukhov (Janjic Eta), MYNN2 (Mellor-Yamada Nakanishi and Niino level 2.5 BL, and MYNN), QNSE (Quasi-Normal Scale Elimination BL, and QNSE), and finally, YSU (Yonsei University scheme, and Monin-Obukhov scheme). As the domains were nested, the studied area had a main mesh and two domains embedded. The computational domains applied were 112 by 91, 94 by 85 and 100 by 82, respectively. For these domains the horizontal resolutions were 45 km, 15 km and 5 km. Moreover, the vertical domain contained 33 levels with 5 heights within the bottom 200 m. In a general evaluation, the QNSE model worked better compared with the other three, providing a mean wind speed of 10.1 m/s and a standard deviation of 5.9 m/s, in comparison with the observed

weather with a mean wind speed of 8.6 m/s and a standard deviation of 5.5 m/s. The wind speed and direction time series obtained from the simulation agreed with the observations. However, the speed values predicted were generally higher than the measurements. More specifically, from 12 to 19 h the results are coherent with the meteorological information, for the rest of the day there are some discrepancies. Finally, the authors concluded that the QNSE scheme was a good tool to describe the wind power forecast in China for arid weather, in hilly landscapes and without any vegetation.

3.6 WRF applied to wind resource assessment

Al-Yahyai et al. (2010) reviewed different NWP models for wind energy assessment. Due to the lack of weather stations on potential sites for wind energy development, NWP models are nowadays widely used to describe the wind resource on these sites. They stated the three main characteristics of NWP models are the ability to increase the vertical and horizontal resolution from coarse (of >40 km horizontally) to refined meshes, (of <1 km horizontally) providing more accurate results for wind farm siting assessment. NWP models are an attractive option as source of wind data, since working with them is cheaper than installing a weather station. Interpolation can be performed over the terrain, obtaining different levels of weather information, all the data can be collected in a period of time without losing information. A weather forecast over a particular time interval can be achieved in less time than using measurements, and finally, NWP can assimilate real measurements to provide more accurate results. However, NWP models are an approximation of the real conditions; they simplify the atmospheric physics to some extent and the initial state is an estimate of the meteorological conditions (See Section 2.3.6). Al-Yahyai et al. (2010) have summarized the work performed by Chagas et al. (2009), where the WRF mesoscale model was applied to analyse the wind

resource in a coastal region, using resolutions of 6 and 3 km and 42 planes in the vertical direction; the parameterization characteristics applied were the Ferrier microphysics for the Cloud and Precipitation scheme. The Planetary Boundary Layer (PBL) physics were described from the Yonsei University (YSU) scheme. The results provided 5% or less difference from measured data, aided with statistical filters to provide more accurate results.

Capps et al. (2012) conducted a wind resource assessment and wind energy yield prediction analysis, for a region in southern California. By comparing predictions of wind speed against detailed wind speed measurements at multiple locations. The authors worked with the WRF model with a set of parameterizations for the outer domains, the Mellor-Yamada-Nakanishi-Niino (MYNN) as a scheme for the boundary layer and the Kain-Fritsch cumulus parameterization. Three nested domains of 27, 9 and 3 kilometres with meshes of 58 by 51, 103 by 85 and 214 by 109 nodes were used, respectively. Additionally, 44 numerical layers in the vertical direction were applied. Hourly wind speed values were calculated at heights from 40 to 160 m with increments of 20 metres. WRF results were compared against Sonic Detection and Ranging (SODAR) wind speed measurements from 55 weather stations, obtaining a RMSE for daily mean wind speed of 0.53 m/s, in contrast to the California Irrigation Management Information System (CIMIS) for a 5 m/s averaged wind speed value. From these results, heights of 80, 100 and 120 m were selected as hub heights to analyse the energy yield, two rated power models were chosen, 1.6 and 2.0 MW, and finally, two sizes for the rotor diameter were taken, 82.5 and 100 m. Annual energy production was calculated considering the differences of hub height, diameter, rated power and wind speed forecast at different heights. From these results, the rotor diameter increases the energy production per dollar capital cost, followed by the rated power investment and finally the hub height.

Carvalho et al. (2012) performed a sensitivity study of the WRF model for a site in Portugal. The authors analysed two numerical simulation characteristics, the grid nesting and integration time. The numerical results obtained were examined in contrast with the measurements of three weather stations, through Root Mean Square Error (RMSE), Standard Deviation (STDE) and Bias. The results described the wind resource locally, however, the wind speed values were underestimated. They found that the integration time should not be greater than two days to achieve a good agreement with the measured wind speed. From this analysis, the WRF model simulation with a 1.2 km resolution, which provided better results was defined with the MM5 Monin-Obukhov for the surface layer model; the Yonsei-University for the planetary boundary layer model and the Noah for the land surface model, which provided a RMSE of 3.16 m/s, a Bias of -2.18 m/s and a STDE of 2.29 m/s for the wind speed, compared against to one of the 60 m height met-masts with a mean wind speed of 7.3 m/s. As has been mentioned, with finer terrain information, fluid flow can be described with more accuracy. In this case, the information on complex terrain sites was poor. From a study like this, it can be shown that when performing tests with different numerical and physical configurations, results can be obtained with little error, if a good description of the surface is available.

Chavez et al. (2012a) assessed the wind energy potential in the northwest of Mexico with the WRF regional model and downscaled the results to a CFD WindSim code for a 200 m resolution domain. The whole of year 2009 was analysed, running 146 simulations, each for intervals of 72-hours, eliminating the first 12 hours of each for model initialisation (referred to as spin-up). The grid used was of 3 km size, which was nested within a domain of 9 km resolution. 35 vertical levels were considered, of which 4 were located within the first 150 m of height. The parameterization models used were Noah for the Land Surface Model (LSM), and the Mellor-Yamada-Janjic scheme for the Planetary Boundary Layer (PBL) model. The 3 km resolution results from WRF

were applied as initial and boundary conditions to perform the CFD analysis (WRF-CFD method). The WindSim CFD code was used to solve the microscale flow, solving the Reynolds Average Navier Stokes (RANS) equations over an approximately 100 km domain, with a grid size near 200 m, and 10 layers in the vertical direction within the first 150 metres above ground level. Finally, the results were compared qualitatively from data of three Automated Surface Observing Systems (ASOS) weather stations, located within the domain, where the wind resource was better represented using the WRF-CFD method over the hilly zones, compared against interpolated values from the 3 km resolution results from WRF, which overpredicted the wind speed for the three met-masts.

3.7 Computational domain size and resolution

In order to describe the methodology to define a suitable number, size and resolution of nested domains, the literature has been reviewed to highlight configurations applied in wind resource analysis by the Weather Research and Forecasting (WRF) model. To refine the analysis over a designated area, a greater resolution can be applied. To represent small scale processes in high gradient zones, greater horizontal resolution is desired. Working on three dimensional computational volumes allows implementation of different methods to increase the resolution.

A popular method, and the one planned to implement in this study, consist in nesting a higher resolution domain, while the outer domain provides the boundary conditions for the nested one. First the global forecast is executed and then one for the nested domain. In order to avoid abrupt changes from nested meshes, a factor from 3 to 5 might be used to increase the nested domain resolution (Liu et al., 2008). A factor of 3 is used for this research.

Rife et al. (2004) applied four nested domains over the Great Salt Lake in Utah, to analyse the wind transport and dispersion of pollution. The resolution of the

domains was of 36 km, 12 km 4 km and 0.333 km, with a mesh size of 70 by 82, 82 by 82, 82 by 82 and 97 by 64 nodes, respectively. The number of vertical levels was 36. The u and v velocity components were compared from the WRF results against met-mast data successfully.

Chin et al. (2010) applied five nested domains over a wind farm in California with horizontal resolution of 36km, 12 km, 4 km, 1.33 km and 0.444 km, the computational domain considered 41 vertical levels. Simulations were validated against measurements. From the results obtained, the authors concluded that the forecast error decreases while the grid resolution is increased. The size of the domain or number of nodes is not provided. Simulations were performed for 54 hours, with 6 hours for spin up and 48 hours for analysis. RMSE was calculated for all the stations over the domain at each of the resolutions studied. As the resolution increases, RMSE decreases, however, there is not much difference from 1.33 and 0.44 km resolutions.

Carvalho et al. (2012) evaluated WRF over a complex terrain in Portugal. Four nested domains with horizontal resolution of 90 km, 18 km, 3.6 km and 1.2 km were applied to simulate the near-surface wind. For the model, 50 vertical levels were configured. Results were compared against three weather stations data at 60 m above ground level, by speed histogram and wind energy rose. From the results obtained, the authors concluded that WRF reproduces accurately the wind speed and direction. However, there is a significant underestimation of the wind speed.

Horvath et al. (2012) applied a telescoping horizontal grid resolution of 27 km, 9 km, 3 km, 1 km and 0.333 km. Data at 50 m height from four weather stations in Nevada from July to December 2007 were used to validate the results. WRF overestimated the wind speed at levels from 10 to 50 m. Three domains of 0.333 km resolution were located within the 1 km resolution domain. The computational sizes of these domains were 50 by 50 to 70 by 70 grid points,

being 16.7 by 16.7 km and 23.3 by 23.3 km, respectively, all of them with 37 vertical levels. Authors concluded that a mesh resolution of about one kilometre is required to reproduce wind speed near the surface over complex terrain. WRF results from each domain are compared against the met-masts data, from this analysis, the authors concluded that as the resolution increases, the difference of mean wind speed and RMSE reduces.

From additional WRF analyses found in the literature, it was found that the number of domains varies among the different studies, from 1 domain (Gilliam and Pleim, 2009; Stylianou et al., 2015), 2 domains (Deppe et al., 2013; Hu et al., 2013; Chavez et al., 2012a; Chavez et al., 2012b; Fitch et al., 2012), 3 domains (Wilson, 2012; Capps et al., 2012; Chenghai et al., 2011; Draxl et al., 2010; Zhang et al., 2009; Michelson and Bao, 2008), 4 domains (Bei et al., 2013; Carvalho et al., 2012; Jiménez et al., 2010; Hu et al., 2010), and finally 5 domains (Horvath et al., 2012; Chin et al., 2010). The number of domains helps to increase the computational mesh density in the nested domains.

From the work reviewed, the dimensions of the nodes in the different domains range from 0.333 to 1 km for the inner domain (Bei et al., 2013; Fitch et al., 2012; Horvath et al., 2012; Chin et al., 2010; Stylianou et al., 2015), from 1.2 to 4 km (Deppe et al., 2013; Carvalho et al., 2012; Chavez et al., 2012a; Chavez et al., 2012b; Wilson, 2012; Capps et al., 2012; Jiménez et al., 2010; Draxl et al., 2010; Hu et al., 2010; Michelson and Bao, 2008), the largest node ranges from 4.5 to 12 km (Hu et al., 2013; Chenghai et al., 2011; Gilliam and Pleim, 2009; Zhang et al., 2009). The smaller size of the nodes will increase the resolution of the results, as well as increasing the computational time and resources for the simulations. In order to find a domain dimension which provides valid results without requiring a lot of time, a sensitivity analysis will be required, as well as setting the number of vertical layers, which is described next. It is worth mentioning

that for wind resource assessment over complex terrain, the domain dimension used had to be from 333 to 444 m (Horvath et al., 2012; Chin et al., 2010).

The number and location of the vertical levels in the computational domain are important to provide an accurate description of the flow at given elevations, such as a wind turbine rotor height. From the work analysed, the range of vertical levels was from 81 to 80 (Fitch et al., 2012; Stylianou et al., 2015), from 51 to 41 (Deppe et al., 2013; Hu et al., 2013; Carvalho et al., 2012; Wilson, 2012; Capps et al., 2012; Chin et al., 2010; Hu et al., 2010; Michelson and Bao, 2008), finally, the smaller number of vertical levels ranges from 27 to 39 (Bei et al., 2013; Chavez et al., 2012a; Chavez et al., 2012b; Horvath et al., 2012; Chenghai et al., 2011; Jiménez et al., 2010; Draxl et al., 2010; Gilliam and Pleim, 2009; Zhang et al., 2009). It is important to note that the levels within a rotor height can be increased (Fitch et al., 2012), considering 8 levels for a 100 m hub height.

3.8 Wind turbine parameterization models

Wind turbines rotor diameters are typically smaller than the resolution of the domain, therefore, the effect on the flow is not resolved on the computational domain directly. Wind turbines produce a wind speed deficit due to the conversion of the kinetic energy of the flow to mechanical power and hence electrical power. For this reason, the wind experiences a deceleration, causing a wake. Different parameterization models to represent the effects of the wind turbines within the WRF model are described next.

One of the models available to calculate the wind turbine effects on the flow, considers a permeable surface normal to the free stream flow (Singer et al., 2010), which prescribes the deceleration that the fluid particle experiences when the wind turbine is encountered, calculated with the deceleration equation (3.1).

$$a_i = \begin{cases} -A|\sin(\theta)|\,(1-d/L)^{\alpha} u_i^{\,2} & for\ d < L \\ 0 & for\ d \geq L \end{cases} \quad (3.1)$$

where the deceleration is a_i; the zonal, meridional and vertical directions are represented by i = 1, 2, 3, respectively. The deceleration of the i^{th} component of momentum is indicated with a_i, the i^{th} component of velocity from u_i, the counter clockwise angle between the mean wind vector and the turbine is described by θ, α is a dimensionless parameter which controls the shape of the attenuation of the deceleration as a function of distance from the rotor plane. Finally, the amplitude of the deceleration is characterized with the parameter A. The perpendicular distance from a computational grid point to the actuator disk is d and the perpendicular distance over which the deceleration is applied is L.

Another model to represent these effects is the wind turbine energy extraction scheme (Blahak et al., 2010). This parameterization for the specific momentum behaviour and the horizontal wind components is developed from the power output curve P from wind turbines (3.2).

$$\dot{E}_{kin,pc}|_{wp} = -\frac{P(v_{rh}) f_{ij} \rho_{rh} \Delta x \Delta y}{\rho_{l0} \eta_{elmech}} \quad (3.2)$$

where $\dot{E}_{kin,pc}$ is the energy removal given by the power output curve (rate of power produced), $P(v_{rh})$ is the kinetic energy flux through the rotor area, f_{ij} is the horizontal density function of wind turbines per area (local number of wind turbines per area), ρ_{rh} is the actual air density at rotor height, Δx and Δy are the horizontal grid distances of the model, ρ_{l0} is the reference air density (1.255kg/m^3), and finally, η_{elmech} is the loss factor due to mechanical friction within the wind turbine and electrical losses.

The wake effects of the wind turbines can also be described by a momentum sink on the mean flow (Fitch et al., 2012). This parameterization method represents the stirring of the ambient flow by the turbines, which produces a perturbation both within the wind farm and downstream where the PBL mixes.

The drag of the wind turbines can be represented by the kinetic energy extracted from the atmosphere and quantified by the thrust coefficient (C_T) and fraction of energy converted into electricity, defined by the power coefficient (C_P), assuming negligible mechanical and energy losses. The fraction of energy transformed into turbulence kinetic energy (TKE), is then obtained from C_T - C_P, calculated with both the Power extracted by the turbines (3.3) and the Turbulent Kinetic Energy (3.4):

$$\frac{\partial P_{ijk}}{\partial t} = \frac{\frac{1}{2} N_t^{ij} C_P\left(|\mathbb{V}|_{ijk}\right)|\mathbb{V}|_{ijk}^3 A_{ijk}}{(z_{k+1} - z_k)} \tag{3.3}$$

$$\frac{\partial TKE_{ijk}}{\partial t} = \frac{\frac{1}{2} N_t^{ij} C_{TKE}\left(|\mathbb{V}|_{ijk}\right)|\mathbb{V}|_{ijk}^3 A_{ijk}}{(z_{k+1} - z_k)} \tag{3.4}$$

where in equation (3.3) (Fitch et al., 2013), $\partial P_{ijk}/\partial t$ is the rate of power extracted by the turbines, which is converted into useful electrical energy, N_t^{ij} is the horizontal density of wind turbines (number of turbines per square metre), C_P is the power coefficient as a function of $|V|_{ijk}$, the velocity vector incident to the rotor. A_{ijk}, is the cross-sectional rotor area of one wind turbine bounded by model levels k, k+1 in grid cell i, j (wind turbine must be located between two levels, and the horizontal velocity vector is assumed to be uniform over the rotor area), $\Delta z = (z_{k+1} - z_k)$, with z_k the height at model level k. For equation (3.4), $\partial TKE_{ijk}/\partial t$ is the rate of power extracted by the turbines which is not converted into electricity, C_{TKE}, is the fraction of energy converted into *TKE*, as mentioned above, obtained from $C_{TKE} = C_T - C_P$, where C_T is the thrust coefficient as a function of the onset velocity, this is just one way to represent the *TKE*, which is stated in the literature (Fitch et al., 2012). The variations of both C_P and C_T with wind speed are input based on manufacturer data for a particular wind turbine model.

The Fitch model neglects interactions between Nt turbines located within the same cell resulting in overprediction of thrust for such configurations. To

address this, Volker et al. (2012) developed a velocity deficit equation based on the thrust from the wind turbines. This velocity deficit is defined by:

$$U_s = \frac{U_0}{\sqrt{2}}\left(1 - \left(1 - \frac{C_t A_0^2}{\sqrt{\pi} W l}\right)^{\frac{1}{2}}\right) \tag{3.5}$$

where in equation (3.5), U_s is the velocity deficit, U_0 is the hub-height velocity, C_t is the thrust coefficient, A_0 is the swept area of the rotor, W is the wake width, which is assumed to be equal to the horizontal grid spacing, and finally, l is the length scale, which describes the velocity over the far wake region (Tennekes and Lumley, 1972).

This section has presented a brief description of the alternative approaches for wind turbine effects within the WRF model. The suitability of the Fitch et al. (2012) wind turbine parameterization model for wind farm power output and wake prediction is reviewed in Chapter 5 and Chapter 6.

3.9 Summary

From the literature review performed for the WRF wind resource assessment studies, the most suitable configuration options have been identified for the purpose of simulating wind resource and wind farm performance at onshore sites with complex terrain (Table 3.1). Five nested domains will be considered, with horizontal resolutions going from 32.400 km for the coarser domain; increasing the resolution with a factor of three gives the following resolutions of 10.800 km, 3.600 km, 1.200 km and 0.400 km; the computational size will be 78 by 78 nodes, with the same centre. In the vertical, 45 layers will be considered.

Three meteorological datasets have been found as the most suitable for the area and for the application, these being, the Global Forecasting System (GFS) (NCWCP, 2013), the North American Mesoscale (NAM) (Rogers et al., 2009) model and the North American Regional Reanalysis (NARR) (Mesinger et al.,

2006). In order to model the mechanisms in the Planetary Boundary Layer, such as the turbulence that affects the momentum, thermal and humidity characteristics of the weather, Mellor-Yamada Nakanishi and Niino Level 2.5 PBL (MYNN Level 2.5) (Janjić, 2002) are appropriate. Additionally, the sensitivity of the schemes to represent the processes at the land surface, these being the surface fluxes of heat, moisture and momentum, will be analysed using the Pleim-Xiu LSM model (Xiu and Pleim, 2001; Pleim and Xiu, 2003) and with the Rapid Update Cycle (RUC) LSM (Smirnova et al., 2000). Finally, the surface layer turbulent effects, such as those caused by the convection and vertical shear, will be represented by the MM5 Monin-Obukhov Surface Layer parameterization model (Monin and Obukhov, 1954; Obukhov, 1971). The Fitch et al. (2012) wind turbine parameterization model will be applied to represent the effects of the wind turbines over the fluid flow

Table 3.1 Parameterization models selected to perform an accuracy analysis with WRF for wind resource assessment.

<table>
<tr><th>Number of domains</th><th>Domain Resolution (km)</th><th>Vertical levels</th><th>Initial Conditions</th><th>Planetary boundary layer model</th><th>Land surface model</th><th>Surface layer model</th></tr>
<tr><td rowspan="5">5</td><td>0.400</td><td rowspan="5">45</td><td rowspan="2">GFS</td><td rowspan="5">MYNN Level 2.5</td><td rowspan="2">Pleim-Xiu LSM</td><td rowspan="5">MM5 Monin-Obukhov</td></tr>
<tr><td>1.200</td></tr>
<tr><td>3.600</td><td rowspan="2">NAM</td><td rowspan="3">RUC LSM</td></tr>
<tr><td>10.800</td></tr>
<tr><td>32.400</td><td>NARR</td></tr>
</table>

These values have to be combined and an accuracy analysis performed in order to identify the most suitable parameterization combination, applied to the local topography and weather conditions from the selected case study region. This analysis is described in Chapter 4.

Chapter 4 Energy yield case study: Baja California

This chapter addresses the accuracy with which the Weather Research and Forecasting (WRF) model predicts values of wind speed and energy yield measured at an operational wind farm of 10 MW rated capacity. Accurate prediction of energy yield from a planned wind farms is of crucial importance to the investment decision. Energy yield of a wind farm is typically estimated based on the time series of wind speed at the turbine hub height considering the power curve from a wind turbine manufacturer. Such wind speed time series can be obtained from met-mast data near the site where the wind farm is to be located. Methods such as measure-correlate-predict (MCP) (Landberg et al., 2003; Rogers et al., 2005) are used if data is not directly available for a suitable time subset at the precise location of interest. The wind resource at planned, or existing, wind farm locations may also be predicted by, Numerical Weather Prediction (NWP) models. The WRF model has been improved in recent years simulating complex atmospheric phenomena that influence the wind resource at potential wind farm sites. Various studies have demonstrated that prediction accuracy can be suitable for wind farm resource assessment (Jiménez and Dudhia, 2011; Deppe et al., 2013).

The ability of the WRF model to represent wind speed over complex terrain has been performed up to horizontal resolutions of 2 km (Jiménez et al., 2013), 1.3 km (Yang et al., 2013) and 1 km (Horvath et al., 2012). For these studies, the elevation range is 2,000 m, 3,250 m and around 3,000 m respectively within domain dimensions of 200 km by 200 km. From these cases, the corresponding maximum slope was of 24.50%, 29.07% and 42.61%. The present study considers a domain of 31.2 km by 31.2 km in the area of La Rumorosa (Fig. 4.1), with elevations from 800 to 1,450 metres above the sea level, the maximum slope for this case is 21.78%. Besides, around 10% of the region has gradient (meters/length) greater than 6%. This is similar to the domains studied by Yang

et al. (2013) and Jimenez et al. (2013), although the mean gradient of the remainder of the domain is greater at 2.70% compared to 2.47% and 2.23%. Horvath et al. (2012) studied a domain with higher average gradient (4.13%).

The availability of annual data from two met-masts over the same year, plus full scale measurements from an operating wind farm, opens the opportunity to extend the WRF model accuracy evaluation to represent the wind resource over a complex area, such as La Rumorosa. To the author's knowledge, the WRF wind resource analysis over complex terrain with a horizontal resolution up to 400 m, combined with two met-masts data and Supervisory Control and Data Acquisition (SCADA) information from an operational wind farm, presented in this Thesis, is the most complete and latest wind resource assessment over the area of Baja California.

Herein the accuracy of both wind speed and wind turbine energy yield predictions obtained using WRF are evaluated by comparison to data available from two met-masts on a 10 MW wind farm, located at La Rumorosa. The topography over the area is mountainous and complex, with elevations from 800 m up to 1,450 m with a distance of 23 km apart. Details of the farm and topographic characteristics of the region are described in Section 4.2. The statistical analysis of the met-mast data to identify date ranges for direct comparison to WRF model simulations is presented in Section 4.3. The wind energy yield data, taken from the Supervisory Control and Data Acquisition (SCADA) system for each of the selected date ranges is described in Section 4.4. A summary of the WRF simulation configuration and the criteria employed for assessing simulation are described in Section 4.5. Finally, the discrepancy between measured and simulated wind speed and energy yield are presented and discussed in Section 4.6.

4.1 Background to the Case Study Site

The State of Baja California has a huge wind resource in the area of La Rumorosa (Fig. 4.1). In order to take advantage of this renewable resource, a 10 MW wind farm has been installed which provides electricity for the public lighting system of the city of Mexicali. Since installation in 2010 this wind farm has generated annually an average of more than 26 GWh per year. This energy supply avoids emissions of more than 17,000 tons of greenhouse gases in the same period (FB&EI, 2012).

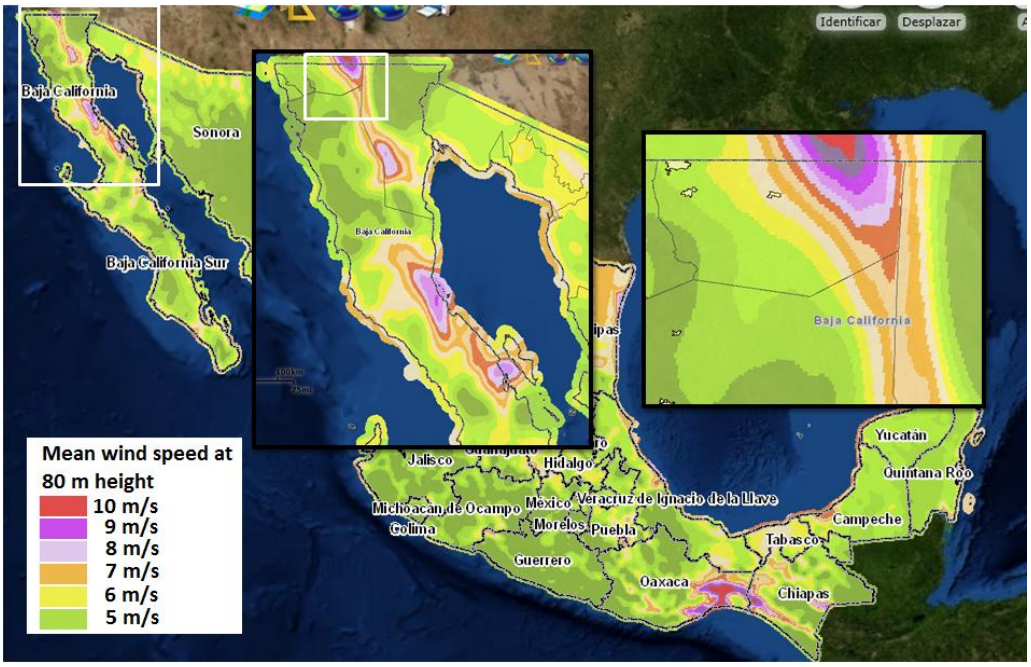

Figure 4.1 Wind resource from Mexico, Baja California and the area of La Rumorosa (IIE, 2016).

4.1.1 Background to Wind Farm Development in Baja California

The state of Baja California is located in the Northwest of Mexico; its boundaries are the Pacific Ocean to the West, the Cortez Sea to the East, the State of South Baja California to the South, and the United States of America (USA) to the North; its area is 71,756 km^2 with a population of 3,155,070 citizens (INEGI, 2012). Its electricity system is not connected to the electricity network of Mexico;

however it is tied to the Western Electricity Coordinating Council (WECC) that connects Mexico, USA and Canada. The state generates all its electricity energy requirements and gives the opportunity to import and export electricity from and to the USA and Canada. The use of renewable energy sources in the region, such as wind energy, will help to preserve the non-renewable energy resources (fossil fuels), promoting sustainable development in the state of Baja California (Ávila et al., 2011; Muñoz et al., 2012).

4.2 La Rumorosa Wind Farm: Site and Data

The town of "La Rumorosa" is located at Lat 32°32'06" N, Long 116°03'00" W, with an elevation of 1,232 meters above sea level. The town is within the Tecate municipality and holds a population over 2,000 people. The region experiences wind speed up to 115 kph (32 m/s) (CFE, 2014), and it is recognized for its high wind energy potential (Puga, 2008).

The National Renewable Energy Laboratory (NREL) of the U.S. Energy Department developed a wind assessment map in the Baja California Border region at 50 m height. The map (Fig. 4.2) shows the wind resource potential of the Baja California region (NREL, 2004) in terms of mean annual wind speed. Wind speed reaches values of 8.8 m/s at 50 m height and a wind power density of up to 800 W/m^2. Over the area studied the wind resource is of class 3, being classified as Fair (NREL, 2004), with annual average wind speed values at 50 m height in the range 6.4 to 7.0 m/s and annual average wind power density in the range 300 to 400 W/m^2.

Based on the results of the NREL wind power assessment, the region of La Rumorosa (red rectangle, Fig. 4.2) has been identified as a suitable area for wind

farm development to generate electricity from the wind resource. The proximity of transmission lines across the state and tied to the Western Electricity Coordinating Council (WECC) also simplifies wind farm connection.

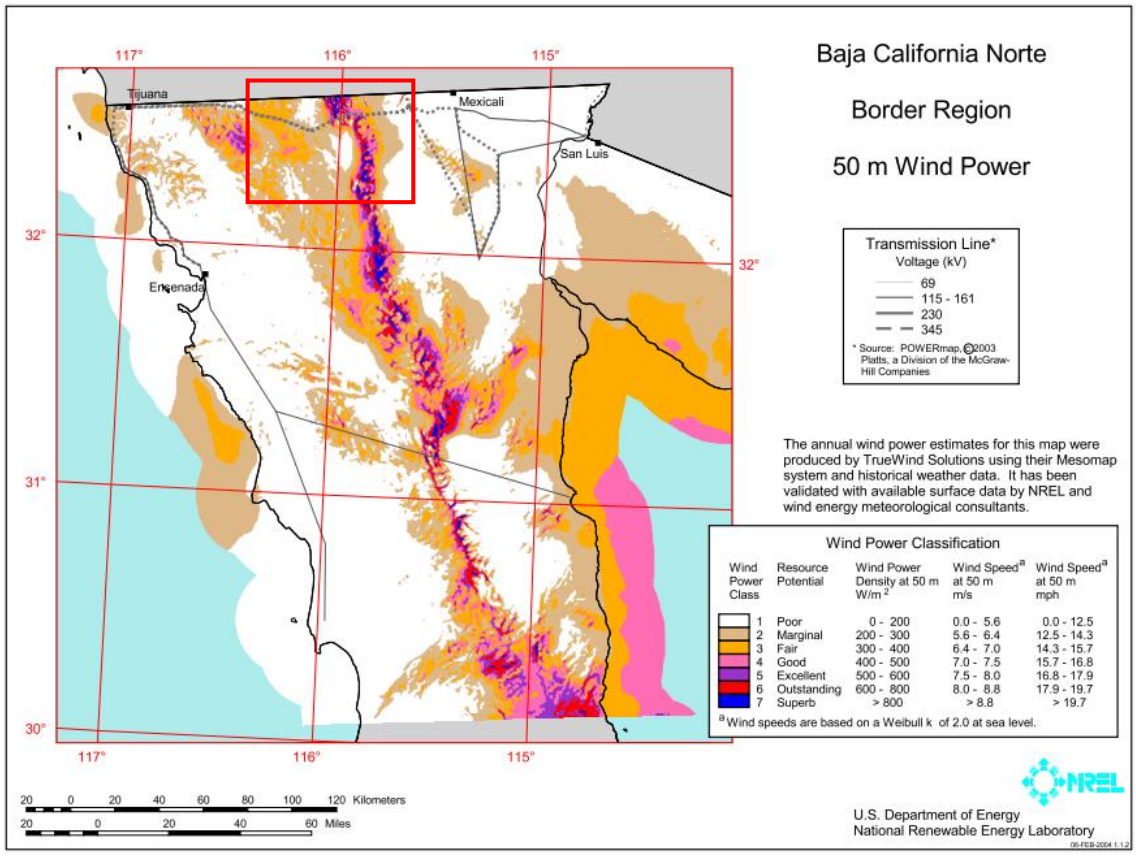

Figure 4.2 Baja California Border Region 50m Wind Power, (NREL, 2004).

To take advantage of the renewable energy local resources, the "La Rumorosa I" wind farm was built. It is a 10 MW wind farm, located on Lat 32°29'47.55" N, Long 116°05'21.01" W. It comprises 5 Gamesa G87-2.0 MW (Gamesa, 2007) wind turbines (Figs. 4.3), each with hub height of 78 m and rotor diameter of 87 m. The terrain is complex, as its elevation varies from 800 m to 1,500 m within a plan area of 30 by 30 km (NASA, 2011). The orientation of the farm is North-West to South-East (160.05°). The average spacing between the wind turbines is 198 m, which is approximately 2.25 times the rotor diameter (Fig. 4.3).

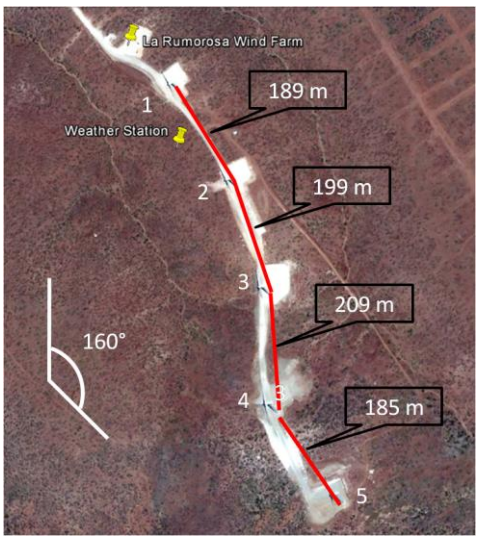

Figure 4.3 Distance between Wind Turbines (Google, 2012).

The power curve of this turbine (Fig. 4.4) indicates a cut-in speed of 4 m/s, rated speed of 16 m/s and cut-out speed of 25 m/s (Gamesa, 2007). During 2011 the average wind speed was 6.91 m/s and more than 27 GWh were produced by the farm; a mean power supply of 3.1 MW from the 10 MW installed capacity.

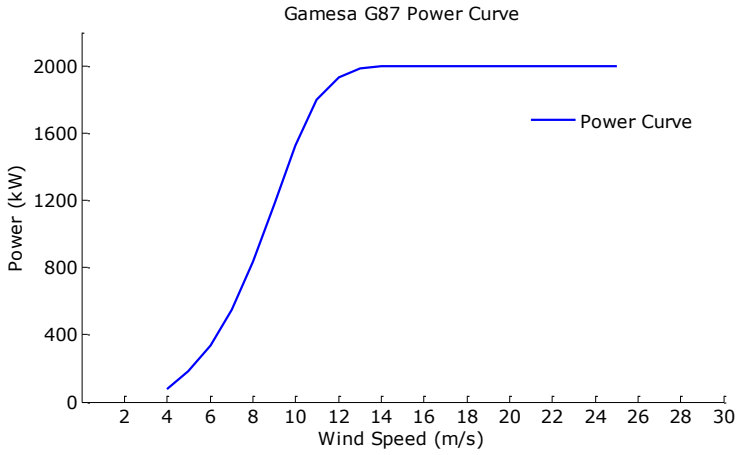

Figure 4.4 Gamesa G-87 2MW wind turbine power curve (Gamesa, 2007).

Data from a wind turbine SCADA system was analysed for the years 2011 and 2014, which was provided from the Baja California Energy Commission, which operates the "La Rumorosa I" wind farm. Met-mast data from the site of La Rumorosa from the 1st of January to the 31st of December, for both years 2011 and 2014 was kindly provided from the Federal Electricity Commission (CFE),

through the Geothermoelectric Projects Management Office. Data was also acquired, from the 1st of January to the 31st of December of 2014, from a met-mast located 16 km west-South-West of the La Rumorosa wind farm, near La Zacatosa. Both met-masts have cup anemometers and sample wind speed every second to calculate and record mean, maximum, minimum and standard deviation of wind speed at ten-minute intervals (Fig. 4.5).

Figure 4.5 La Zacatosa met-mast (left) and La Rumorosa met-mast (right) (Google, 2012).

4.2.1 La Rumorosa met-mast data

The met-mast from "La Rumorosa" is located at latitude of 32.498° and longitude -116.091° with an altitude of 1,358 m above the sea level. Available data is in full for the years 2011 and 2014, mean wind speed has been obtained at 50 m height from the three elevations available sampled every ten minutes. A 60 m height tower is installed 50 m west of the middle of the two northernmost wind turbines (AEG-1 and AEG-2), which has three cup anemometers at heights of 40, 50 and 60 m (NRG, 2010a), and a wind vane at 60 m (NRG, 2010b). These devices have a 95% of statistical confidence to provide true values within ±1.48% of the reading (NRG, 2015). Data is measured every second and after 10 minutes, average, minimum, maximum and standard deviation values are calculated and stored in the data logger (NRG, 2010c). As this system has its own power system, there is no gap between the readings. Typically 52,560 readings were gathered each year.

From the La Rumorosa met-mast at 50 m height, mean wind speed values were obtained of 6.72 m/s and 6.41 m/s for years 2011 and 2014, respectively and the annual standard deviation is 3.14 m/s and 2.97 m/s for the same years.

Fig. 4.6 compares the fitted Weibull distributions (see Section 2.1.3) from La Rumorosa met-mast, scale and shape parameters for the two years, for which data was available, the RMSE between the measurements and the Weibull distributions at 50 m height was of 0.021% for 2011, while for 2014 was of 0.025%. For year 2011 scale and shape factors of 7.57 m/s and 2.23 were calculated, while for year 2014, these values were of 7.23 m/s and 2.26, respectively.

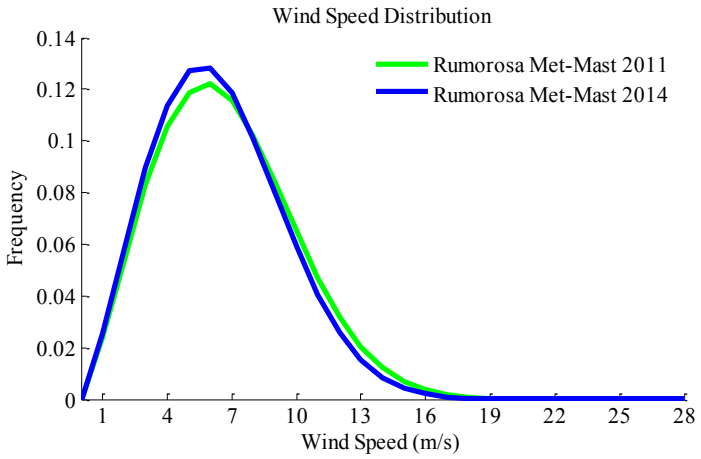

Figure 4.6 La Rumorosa met-mast at 50 m height annual distributions for 2011 and 2014.

4.2.2 La Zacatosa met-mast data

The other met-mast is located 16 km away from "La Rumorosa" on a West-Southwest direction, this is referred to as "La Zacatosa" met-mast, from which data is available from the 1st of January to the 31st of December 2014, at heights of 60, 70 and 80 m, with an altitude of 1,169 m above the sea level. Figure 4.5 shows a relative location within the domain. Similar to La Rumorosa met-mast, data from 2014 at La Zacatosa met-mast at 70 m height was analysed, with an

annual mean wind speed value of 6.42 m/s and an annual variation of 3.95 m/s. The annual Weibull distribution from La Zacatosa met-mast data was calculated following the same methodology as for the "La Rumorosa" site, considering the ten-minute met-mast data at 70 m height from the site and calculating the scale and shape parameter via equations (2.10) and (2.11). The resultant scale and shape factors were of 6.45 m/s and 1.66 for the year 2014 and the Weibull distribution defined by Equation 2.8 is shown in Figure 4.7, which presented a RMSE of 0.031% at 70 m height compared against the measurements. As this site is located in a valley and is 200 m below the altitude of the La Rumorosa met-mast, the energy at this site is smaller compared against the La Rumorosa site.

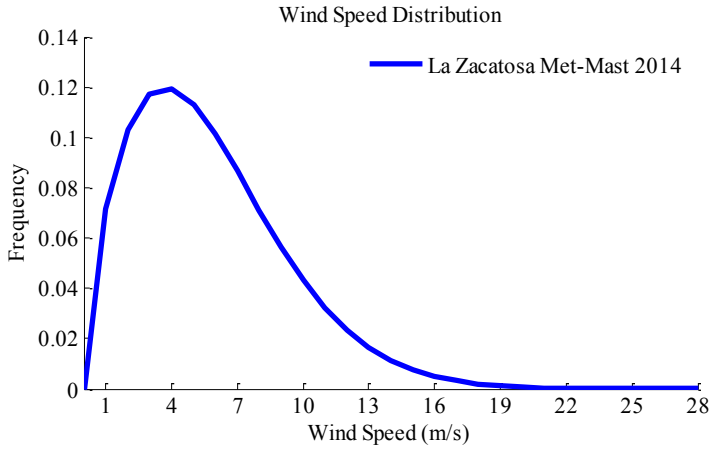

Figure 4.7 La Zacatosa met-mast at 70 m height annual distribution for 2014.

4.2.3 Wind farm Supervisory Control and Data Acquisition (SCADA) data

The SCADA system for each wind turbine sampled every ten minutes for the whole years of 2011 and 2014. The data recorded includes mean wind speed and direction, measured from an anemometer on top of the nacelle, and the electrical power output from the turbine. A cup anemometer located on top of the turbine nacelle provided wind speed. The mean power is defined by the energy yield during each ten-minute sample interval. The direction to which the wind turbine is oriented, as their yaw systems orientates them towards the

wind, is stored. Annual wind energy yield for 2011 was of 27.4 GWh, while for 2014 was of was of 25 GWh (Table 4.1).

The data from all the five wind turbines' anemometers at 78 m height were averaged to calculate the annual mean wind speed, these being 7.85 m/s for 2011 and 7.24 m/s for 2014 considering the wind speed from all the turbines at 78 m height, compared to 50 m height met-mast annual mean wind speed values of 6.72 m/s and 6.41 m/s for the respective years, from Section 2.1.3. Annual Weibull distributions were calculated for each wind turbine for years 2011 and 2014, to describe the probability distribution of the wind speed at hub height for each wind turbine. Weibull distribution of wind speed occurrence based on the wind speed dataset for each of the five wind turbines (AEG-1 to AEG-5) are presented in Figure 4.8 and Figure 4.9 for the years 2011 and 2014 respectively. Comparing wind speed and energy yield from one year to the other, it is clear to see that energy yield was greater in 2011, and throughout the wind speed distributions, it is shown that 2011 had also a better wind resource distribution.

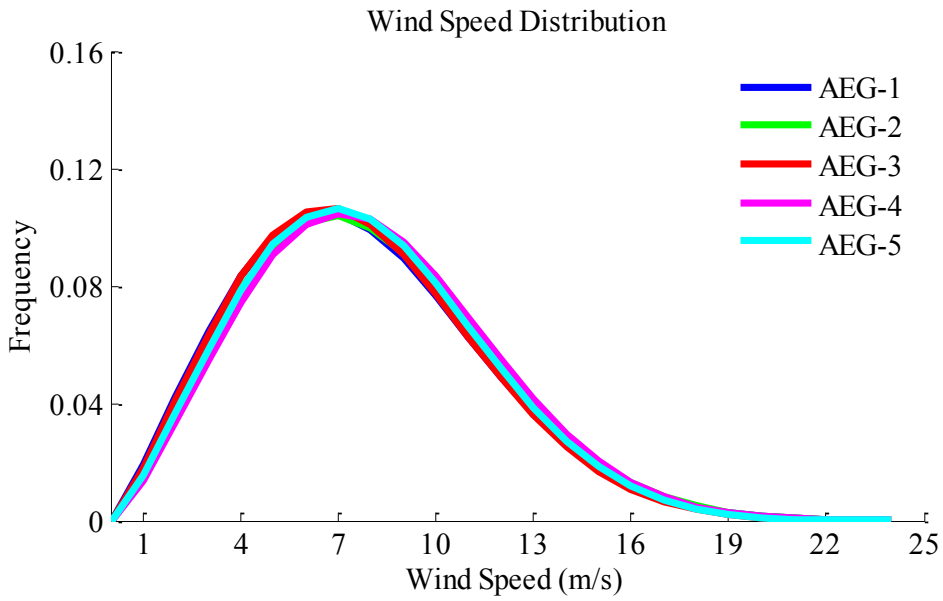

Figure 4.8 Annual turbines wind speed distribution 2011 at 78 m height.

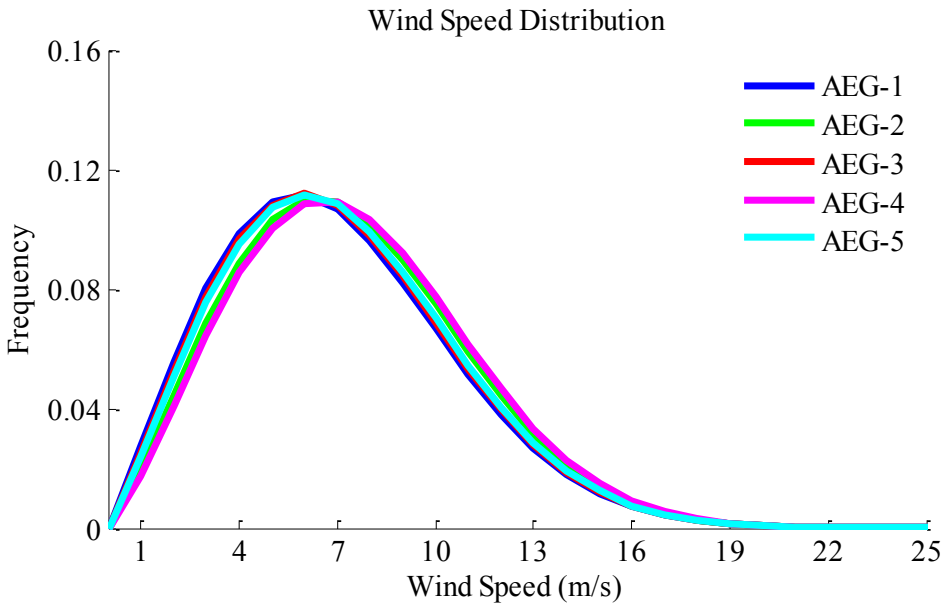

Figure 4.9 Annual turbines wind speed distribution 2014 at 78 m height.

Table 4.1 "La Rumorosa I" Annual energy yields per wind turbine (GWh).

Wind Turbine	2011	2014
AEG-1	5.525	5.005
AEG-2	5.536	5.002
AEG-3	5.499	5.017
AEG-4	5.374	5.006
AEG-5	5.444	4.975
Whole Farm	**27.378**	**25.006**

4.3 Data samples analysis for WRF simulations

The objective of this section is to identify the accuracy with which the WRF model is able to predict both wind speed and wind farm energy yield relative to the measured data. The basis for assessing prediction accuracy is briefly described in Section 4.3.1. The computational cost required to run a WRF simulation for a full year is prohibitive. As such a subset of the full dataset was

identified to represent the annual distribution of wind speeds. This process is detailed in Section 4.3.2.

4.3.1 Metrics for evaluation

To quantify the accuracy with which the wind speed during a selected time-interval represents the annual distribution and to quantify the accuracy of WRF results relative to the met-mast data, several metrics are considered. The Root Mean Square Error for a statistical distribution ($RMSE_f$) applied to compare two statistical distributions are (i.e. Weibull distribution, histogram):

$$RMSE_f = \sqrt{\frac{\sum_{u=0}^{U_{max}} \left(f_{u,m} - f_{u,p}\right)^2}{n_u}} \tag{4.1}$$

where $RMSE_f$ is the Root Mean Square Error for a statistical distribution, u is the wind speed bin, U_{max} is the maximum wind speed bin, $f_{u,m}$ is the corresponding frequency from each wind speed value from the met-mast $f_{u,p}$ is the frequency from the same wind speed value from the subset or the WRF result which is compared against the met-mast, and n_u is the number of wind speed bins.

Additionally, the wind direction can be included in this analysis, where the Root Mean Square Error for a wind rose distribution ($RMSE_\theta$), which compares the statistical distribution for each wind speed at their corresponding direction. Equation (4.2) describes it:

$$RMSE_\theta = \sqrt{\frac{\sum_{u=0}^{U_{max}} \sum_{\theta=0}^{360} \left(f_{1,u,\theta} - f_{2,u,\theta}\right)^2}{n_{u,\theta}}} \tag{4.2}$$

where $RMSE_\theta$ is the Root Mean Square Error for a wind rose distribution, u is the wind speed bin, U_{max} is the maximum wind speed, θ is the wind direction bin, $f_{u,1,\theta}$ is the corresponding frequency from each wind speed and direction value from the met-mast $f_{u,2,\theta}$ is the frequency from the same wind speed and direction value from the subset or the WRF result which is compared against

the met-mast, and finally, $n_{u,\theta}$ is the number of bins, obtained by multiplying the amount of wind speed bins by the amount of wind direction bins.

After WRF simulations are performed, the wind speed time series results are compared against the met-mast data for the same date range. This can be done by calculating the Root Mean Square Error (*RMSE*), which is described by equation (4.3):

$$RMSE = \sqrt{\frac{\sum_{t=1}^{n_t}\left(u_{1,t} - u_{2,t}\right)^2}{n_t}} \tag{4.3}$$

where *RMSE* is the Root Mean Square Error for a time series, *t* is the time step, n_t is the amount of time steps, $u_{1,t}$ is the wind speed value for a time step from the met-mast and $u_{2,t}$ is the wind speed value for the time same step from the WRF result which is compared against the met-mast.

In order to quantify how significant is the *RMSE* compared against the wind speed of the selected date range, the coefficient of variation (*cv*) is applied to link both values throughout the division of the *RMSE* by the mean wind speed from the met-mast for a given subset of data (Equation (4.4)).

$$cv = \frac{RMSE}{\bar{u}} \tag{4.4}$$

where *cv* is the coefficient of variation for a time series, *RMSE* is the Root Mean Square Error from equation (4.3) and $\bar{u}$ is the mean wind speed from the met-mast subset data.

Finally, to address the accuracy from the WRF model in terms of wind energy yield prediction, the wind energy yield relative error calculates the discrepancy between these two values in equation 4.5:

$$\delta = 100 \times \frac{E - E_{approx}}{E} \tag{4.5}$$

where δ is the wind energy yield relative error, E is the wind energy yield obtained from the SCADA system from the wind farm and E_{approx} is the wind energy yield calculated by extracting the wind speed values at each wind turbine hub-height and applying the manufacturers power curve.

4.3.2 Selection of time-interval for WRF simulation.

Computational simulations from NWP models, such as the WRF, are complex and require significant computational resources both in terms of memory during the simulation and in terms of data storage and analysis. Based on the spatial resolution of prior WRF studies of wind resource (Chin et al., 2010; Horvath et al., 2012) and farms (Jiménez et al., 2015), the computational cost to simulate a one week period on the available computer resources, Computational Shared Facility (CSF) from the University of Manchester, is expected to be around 36 hours on 128 processors. Simulation of a full-year for direct comparison to the met-mast data is therefore clearly impractical. Subsets of the annual time-series which describe accurately the statistical distribution over the year have shown to be a reliable tool to project WRF results for their corresponding years (Stylianou et al., 2015). Intervals are selected in terms of both: the similarity of the wind speed distributions between the subset and the met-mast annual data, and to have a length of the sample big enough for a statistical analysis; for the two weeks subsets, 2,016 samples are selected; whereas for the four weeks subsets 4,032 samples are chosen, from 52,560 ten-minute time steps.

4.3.2.1 Selection of date ranges based on La Rumorosa data:

For year 2011, a subset of two consecutive weeks from the "La Rumorosa I" wind farm met-mast data was chosen due to its accuracy to represent only the wind speed probability distribution and the annual wind speed histogram. The Weibull distribution (Eq. 2.8) was calculated from the met-mast ten-minute data and was considered as the representative annual wind distribution. The same

distributions were calculated for 351 two consecutive week periods from the same year, considered as the subsets. Each one of these subsets were compared against the annual representative distribution through the $RMSE_f$ (Eq. 4.1), from which, the smallest value was identified as the subset with the closest similarity in terms of wind speed distribution to the whole year. The WRF analysis was only performed to quantify its accuracy to forecast the wind speed over a subset which considers high and low values which happened throughout the year and how accurate the wind energy yield can be predicted.

This sample will be representative to perform WRF model simulations covering high and low speed values as happened during the year. Additionally, performing an accuracy analysis for a two weeks subset is less expensive in terms computational resources. The Weibull probability density function was calculated for the annual data from the La Zacatosa met-mast, and then the distribution for each two consecutive weeks from the 1st of January up to the 18th of December was calculated. The $RMSE_f$ was calculated for each two consecutive week subset, Figure 4.10 presents the histogram of the $RMSE_f$ for all the 351 subsets analysed where it can be seen that the predominant values range between 0.0165% and 0.0125% for the histogram.

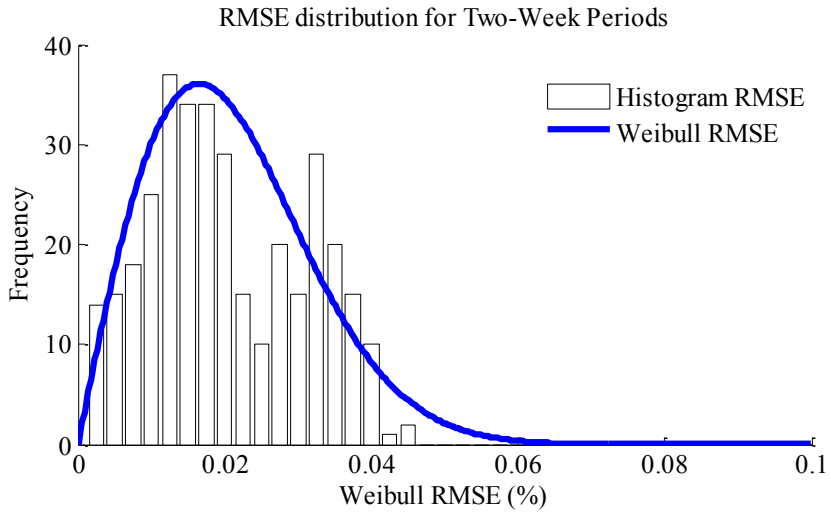

Figure 4.10 Histogram and Weibull distribution of the $RMSE_f$ values obtained for selected time-intervals during 2011.

The selected subset provided an $RMSE_f$ value for the Weibull distribution of 0.0962%, while for the same sample the histogram was 0.8162% within the frequency values; this means the difference from the subset in terms of the probability distribution are these values respectively. The subset which fitted better both Weibull distribution and histogram was from 26th of October to 8th of November 2011 (Fig. 4.11). Smallest $RMSE_f$ values ranged from 0.0871% to 0.2389% and from 0.6931% to 0.9046%, for the Weibull distribution and histogram, respectively for the closest 10 subsets.

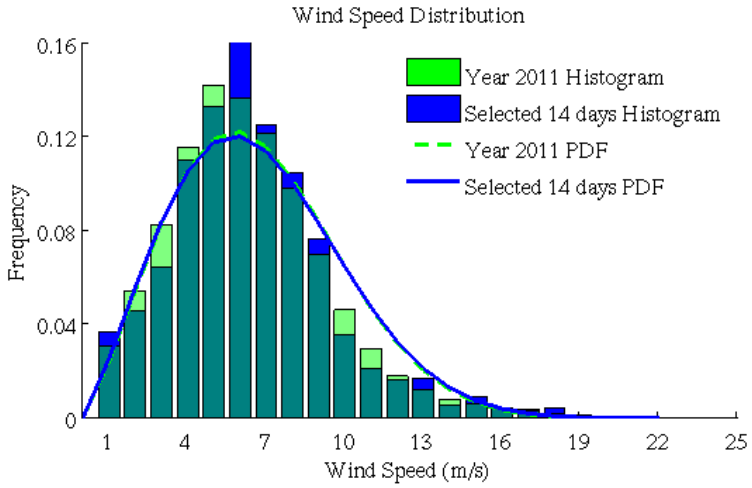

Figure 4.11 Wind speed distribution comparison for year 2011 and selected subset from La Rumorosa met-mast.

4.3.2.2 Selection of date ranges based on La Zacatosa data:

A subset from the La Zacatosa met-mast over 2014, which is located 16 km west-southwest from the La Rumorosa I wind farm, was selected based on both the wind speed and the direction distribution, due to the focus of the analysis to quantify the effect of a large scale wind farm in close proximity. In this term, the subset has to comply as accurately as possible, with the annual wind speed and direction distribution (wind rose distribution). As the complexity of the variables increases, samples have to be bigger to increase the accuracy with which the sample represent the annual wind speed and direction distribution.

A sample from the 2014 annual data was also selected based on four non-consecutive weeks. In this case, subset from La Zacatosa met-mast was aggregated considering each one of the four weeks to a season time of the year (i.e. one from spring, summer, autumn and winter).

Wind speeds from these four time-intervals were considered as an aggregated subset and their corresponding Weibull, histogram and wind rose distribution was calculated. These distributions were compared against the annual Weibull, histogram and wind rose distribution throughout the $RMSE_f$ and $RMSE_\theta$ for each one of the aggregated subsets from all the combinations of four weeks subsets selecting one week from each season.

From the aggregated subsets, the one with minimum $RMSE_f$ (Eq. 4.1) was from the 6th to 12th of January, plus 3rd to 9th of May, with 31st of July to 6th of August, and finally, 26th of November to 2nd of December 2014. Regarding the wind speed distribution from the aggregated subset compared to the annual data from the La Zacatosa met-mast (Fig. 4.12), the $RMSE_f$ for the histogram was 0.307% and for the Weibull distribution was of 0.405%.

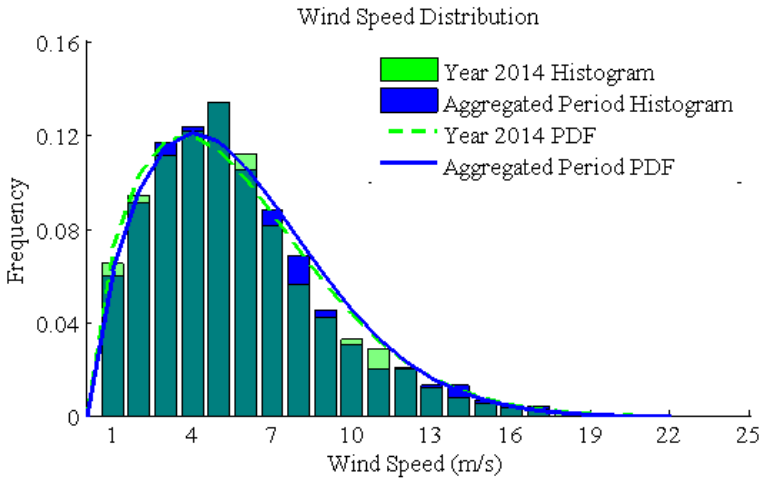

Figure 4.12 Wind speed distribution for four aggregated weeks from 2014 at La Zacatosa site met-mast.

Additionally, the aggregated wind rose distribution, which is a wind speed distribution binned on ten degrees direction, was compared against the annual distribution. Although the aggregated subset considers four weeks over the whole year, the description of the wind rose compared against the annual subset provided an $RMSE_\theta$ value of 9.242%, being the closest aggregated description (Fig. 4.13).

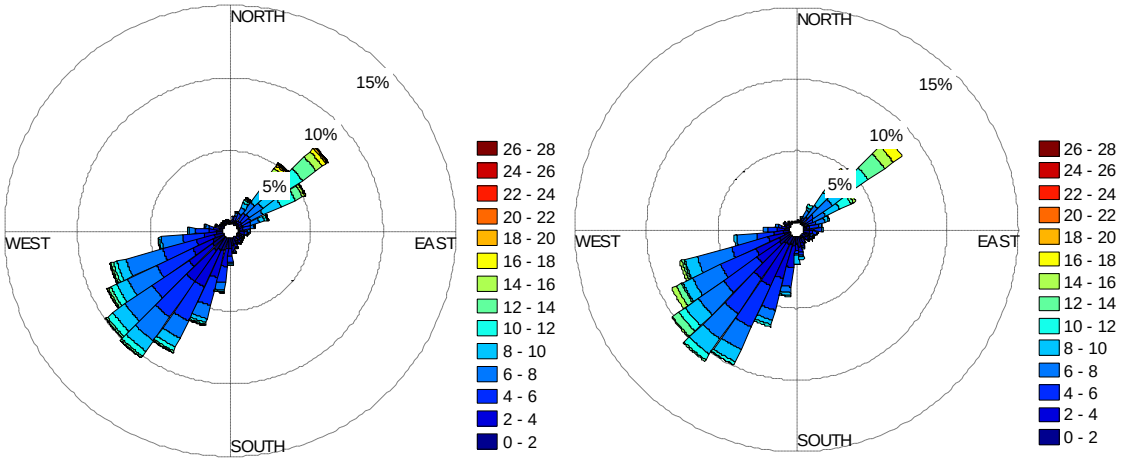

Figure 4.13 Annual (left) and Four aggregated weeks (right) wind rose distribution from 2014 at La Zacatosa site met-mast.

4.3.3 Analysis of SCADA data over selected date ranges

Considering the "La Rumorosa I" wind farm SCADA data, ten minute wind power data was extracted from each one of the five wind turbines, to present their respective time series and the amount of wind energy yield produced during each one of them.

The five wind turbines power time series for the 2011 subset has been extracted from the SCADA system. Figure 4.14 shows the power from each turbine, where the values go from zero to rated power along the subset. Table 4.2 summarises a production of 1.066 GWh for all the turbines during the subset, which once projected over the year, provides 27.810 GWh. This is 1.58% lower than the annual energy yield, compared to a -4.13% of difference based on the wind energy yield from the Weibull distributions from Figure 4.12.

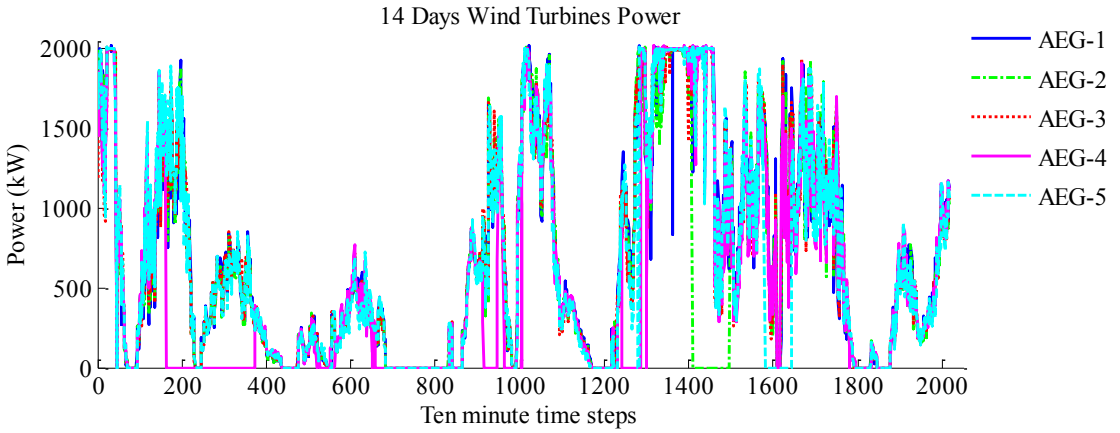

Figure 4.14 "La Rumorosa I" wind power time series from the 2011 subset.

In a similar manner, the data from each turbine during the aggregated subset from 2014 was extracted. Figure 4.15 presents the time series for each turbine power, values go from zero to rated power, highlighting a part when there was unavailability for all the farm. Table 4.2 presents a total energy yield production of 1,939,504 kWh for all the turbines during the subset, this wind energy yield projected to the corresponding year reached 25,282,815kWh, which is 1.11% less than the energy yield for the same year.

.

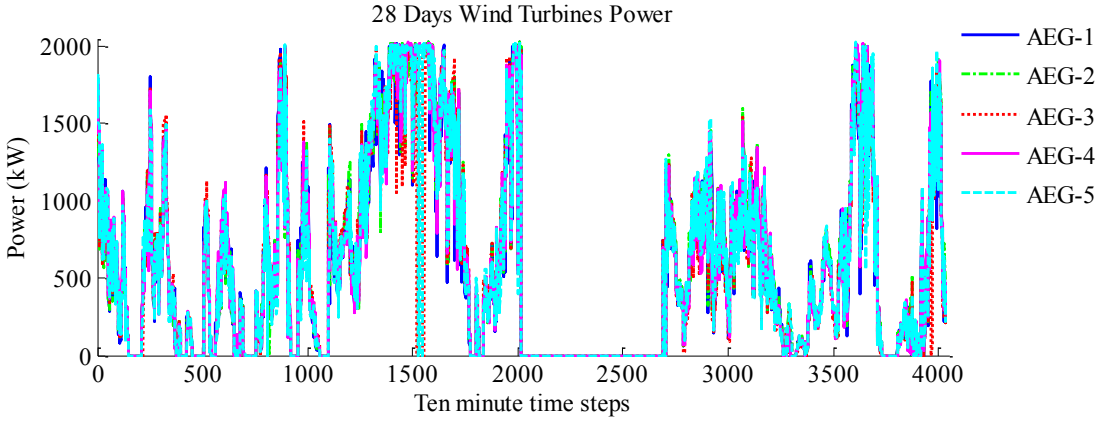

Figure 4.15 "La Rumorosa I" wind power time series from the 2014 subset.

Table 4.2 "La Rumorosa I" selected subsets from 2011 and 2014 energy yield per wind turbine (kWh).

WindTurbine	2011	2014
AEG-1	230,172	388,624
AEG-2	205,545	394,738
AEG-3	226,583	383,110
AEG-4	186,459	391,243
AEG-5	217,920	381,789
Whole Farm	1,066,680	1,939,504
Projected Year	**27,809,871**	**25,282,815**
Real Year	**27,378,000**	**25,006,000**
Difference	-1.58%	-1.11%

After selecting the representative subsets for each year, the process to configure the WRF accuracy analysis is presented in the next section.

4.4 Configuration of WRF simulations for La Rumorosa wind speed

The accuracy with which the WRF model predicts the wind speed is assessed relative to the time-history (Section 4.5.1) and to the Weibull distribution (Section 4.5.2) of wind speed and relative to the energy prediction measurements of (Section 4.5.1) over the same period. Energy production was only defined from the results of WRF wind speed distribution and wind turbine power curve. The WRF model was configured with five two-way nested domains (Fig. 4.16), with resolutions ranging from 32,400 m to 400 metres, the ratio between each domain was three; the computational size was of 78 by 78 each domain and 45 vertical levels were set, twelve of these vertical levels were located within the lowest 200 m as defined in Section 3.9. The centre of the

domains was defined at Latitude 32.4817° and Longitude -116.2192° (centre of domain in Figure 4.16), in this way, that the highest resolution domain (400 m) covers both met-mast locations, all five turbines of the "La Rumorosa I" wind farm and four polygons of land which have been advertised for wind energy developments (these sites are explained in Section 6.3). For each simulation a 12 hour spin-up time was employed after which the simulated wind speed was output at intervals of one hour. Six simulations were conducted with three different meteorological datasets as input and two combinations of parameterization scheme. Details on the WRF Preprocessing System (WPS) configuration namelist can be found on the Appendix A.

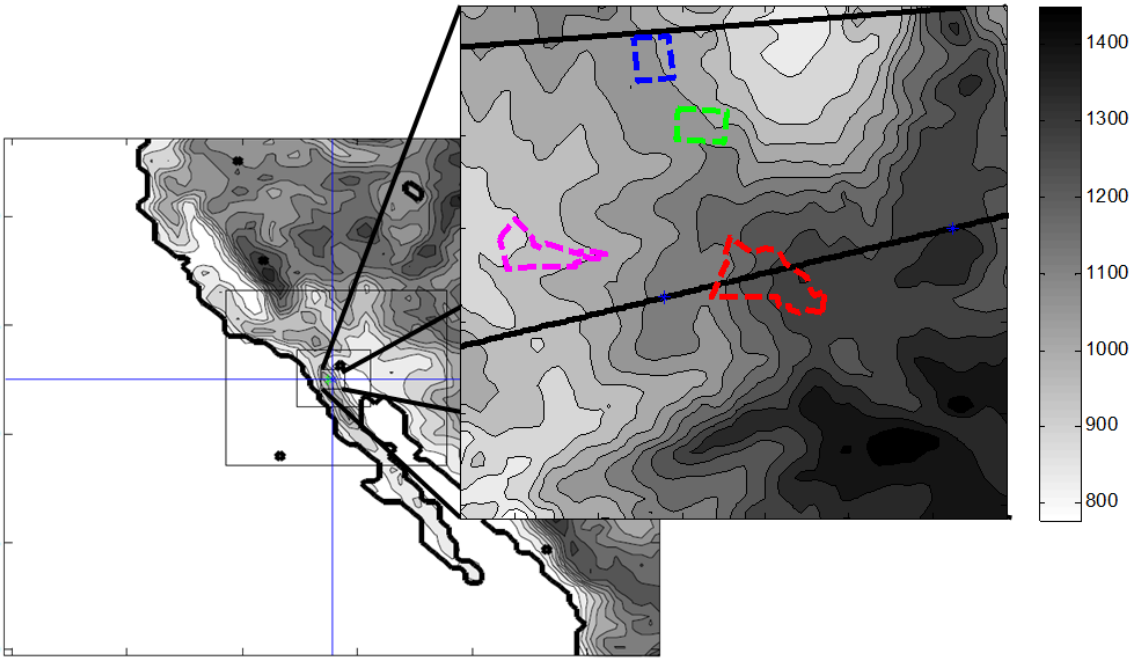

Figure 4.16 Computational Domains and Domain 5 with 400 m resolution, the colourbar presents the terrain elevation in metres (NASA, 2011).

Two variables were considered to perform the accuracy analysis: the meteorological dataset, which provides initial and boundary conditions for the simulation, and the Land Surface Model (LSM) parameterization scheme, which balances the data from the surface layer model with the radiative flow and precipitation information.

4.4.1 Local topography

The topography data was acquired from the NASA Advanced Spaceborne Thermal Emission and Reflection Radiometer (ASTER) Global Digital Elevation Model (GDEM) Version 2 (NASA, 2011). The surface characteristics of the fifth domain with a 400 m resolution are quite complex (Fig. 4.16), ranging with elevations levels from 800 up to 1,450 metres above the sea level.

4.4.2 Meteorological datasets

Simulations were configured with three different meteorological datasets, which provided the initial and boundary conditions to the model. These data were obtained from the Global Forecast System (GFS), North American Mesoscale Forecast System (NAM) and North American Regional Reanalysis (NARR).

4.4.3 Parameterization models

The WRF model is configured based on the parameterization schemes, which represent the fluxes balances within the atmosphere. The Land Surface Model (LSM) parameterization model balances the data from the surface layer model with the radiative flow and precipitation information, taking into account the characteristics of the surface to calculate the fluxes of heat and moisture over the terrain, which are later applied as a boundary condition for the PBL scheme.

Two LSM options were considered for this analysis. One is the rapid update cycle (RUC) Land Surface Model, which considers six soil levels and solves the moisture and heat transfer, it is based on the concept of solving the energy and moisture budgets. The highest ground layer covers half of the lowest half of the first atmospheric layer to update the heat storage based on the balance of the fluxes. The other, Pleim-Xiu Land Surface Model, considers only two soil layers. From which, the temperature and moisture are calculated based on the soil

moisture, radiation flux and air temperature. Due to the difference on the approaches of both LSM parameterization schemes, the simulations with the same initial and boundary conditions will provide a change on the wind resource profiles over the studied domain.

The Planetary Boundary Layer (PBL) model solves the vertical fluxes over the atmospheric column. It takes the fluxes calculated from the surface layer and land surface models to define the profile on the lower and higher boundary layer as well as the temperature, moisture and momentum quantities along the atmospheric column, working only over the vertical dimension. For this study, it was kept constant for all the simulations, being the option selected the Mellor-Yamada Nakanishi and Niino (MYNN) Level 2.5 PBL model. This PBL model is applied at the planetary boundary layer and over the free atmosphere by implementing an upper limit on the length scale, dependant on the turbulent kinetic energy, buoyancy and shear of the flow.

The Surface Layer (SL) model, which balances the heat and moisture fluxes between the LSM and PBL schemes, throughout the computation of friction velocities and exchange coefficients, was kept fixed for all six simulations. The revised MM5 surface layer scheme is the one selected for this parameterization model, which calculates the terrain exchange coefficients for momentum, heat and moisture. These last two are enhanced throughout the adoption of the convective velocity.

This analysis was performed in order to identify the WRF configuration which provides more accurate results. Three meteorological datasets have been combined with two combinations of PBL, LSM and SL parameterization schemes. Simulations have been performed for each one of the six configurations, and from the results, wind speed values have been interpolated at two different met-mast locations (e.g. La Rumorosa and La Zacatosa). Wind speed values have been also interpolated at the wind turbines from La

Rumorosa I wind farm, which with the corresponding power curve, the wind power and energy yield have been calculated. A *RMSE* analysis has been performed for the statistical distribution and the time series from the met-mast, while for the wind turbines, a wind energy yield error analysis has been performed.

Simulations are coded with the meteorological dataset (GFS, NAM or NARR), followed by the WRF model configuration which can be either 5-3-1 or 5-7-1, where 5, denotes the Planetary Boundary Layer option MYNN Level 2.5 PBL model. The 3 and 7 denote the Land Surface Model, Rapid Update Cycle (RUC) LSM (option 3) or by the Pleim-Xiu Land Surface Model (option 7), and the Surface Layer option, being the revised Monin-Obukov MM5 surface layer scheme. Details on the WRF configuration namelist can be found on the Appendix B.

4.5 Results and Discussion

In this section, the accuracy of the wind speed predicted by the six WRF models described in Section 4.4 are evaluated based on the metrics defined in Section 4.3.1. The wind speed time-series, statistical distribution, wind rose distribution and the wind energy yield are compared to measurements via equations 4.4, 4.1, 4.2 and 4.5, respectively.

4.5.1 Prediction of met mast time series of wind speed

From the 2011 two consecutive week subsets, WRF wind speed simulations provided a 10 minute intervals output at the met-mast point. Wind speed met-mast data is averaged at 50 m height and WRF accuracy analysis values were interpolated horizontally and vertically at the met-mast point. Wind speed met-mast from La Rumorosa data is averaged at 50 m height and WRF accuracy analysis values were interpolated horizontally and vertically at the met-mast point.

Consecutive samples of wind speed at 50 m height were averaged for direct comparison to the hourly time series from the met-mast (Fig. 4.17). Met-mast data provided a mean wind speed value of 6.85 m/s. From the GFS simulations, the 5-3-1 model provided a 6.94 m/s mean wind speed value, whereas the value from the 5-7-1 model is 6.48 m/s. The NAM dataset mean wind speed value for the 5-3-1 configuration is 6.70 m/s, while for the 5-7-1 it is 6.53 m/s. Finally, mean wind speed value for the 5-3-1 NARR dataset model is 6.61 m/s and finally, for the same dataset, the 5-7-1 parameterization model the mean wind speed is 6.25 m/s. For all methods mean wind speed was within 8.7% of measurement. Higher mean wind speed values and closer to the met-mast mean wind speed were found for the 5-3-1 model compared against the 5-7-1 model for each meteorological dataset, since the Rapid Update Cycle LSM (option 3) considers six levels on the ground, compared against three levels from the Pleim-Xiu LSM model (option 7). All the simulations follow the trend of the met-mast data, the NARR dataset appears to be closer to the measured data. Simulation NARR 5-3-1 is the one which shows more accurate values for the RMSE and coefficient of variation.

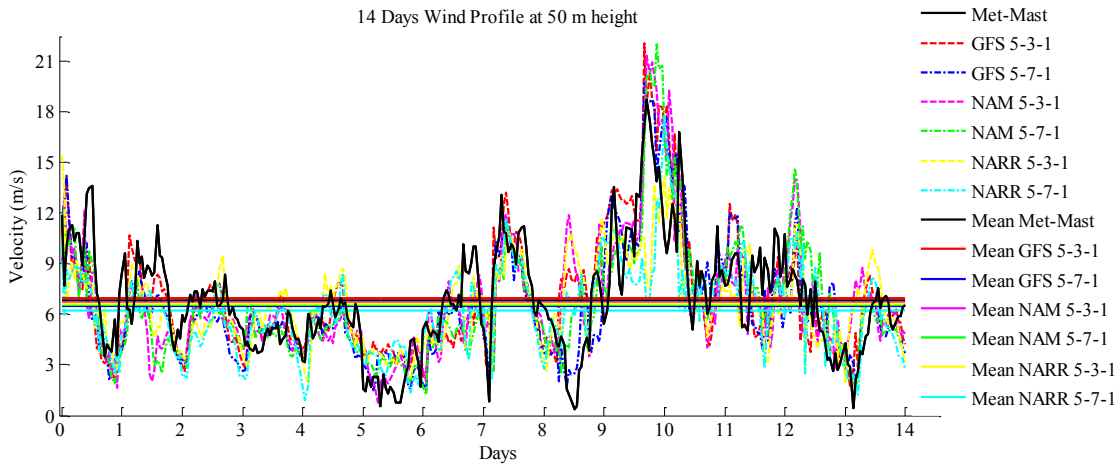

Figure 4.17 Hourly time series results from WRF from dataset compared against La Rumorosa met-mast data at 50 m height for 2011 two weeks period (black solid line).

A time offset analysis was performed to identify the amount of hours shifted from the local time at La Rumorosa met-mast to the Coordinated Universal Time (UTC), this is the one from which the meteorological datasets for the boundary and initial conditions work with. Specific date and UTC time was taken for the weekly simulation's initial conditions, from which wind speed results were interpolated at the met-mast height. The time series for the numerical results were compared against the met-mast data from 24 hours in advance up to 24 hours from the time of the initial conditions in hourly steps. The coefficient of variation (equation 4.4) was calculated for each of the WRF configurations results and each of the 49 hourly periods from the extended met-mast time series. The coefficient of variation (*cv*) for each of the WRF configurations was calculated for each time offset. Where the offset with the smallest *cv* was at -7 hours with a coefficient of variation of 9.57 % for the GFS 5-7-1 configuration.

Additionally, a spatial offset analysis was performed by defining points at distances of 100 m, 500 m and 1,000 m away from the met-mast point at directions from 0° to 330° with steps of 30° (Fig. 4.18). In total, 36 points were applied to calculate the coefficient of variation for the wind speed (equation 4.4).

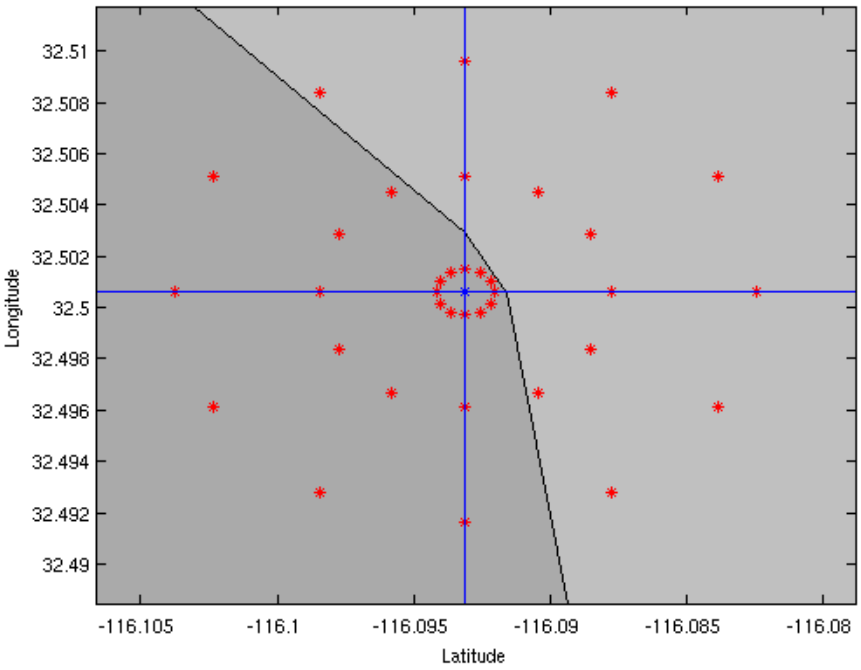

Figure 4.18 Points to analyse the coefficient of variation in a radial distribution.

Figure 4.19 presents the distribution of the coefficient of variation (equation 4.4) along the radial points mentioned before. These values vary from 4.38% up to 8% within a radius of 1 km. From which the interpolated point located 500 m north from the coordinates had the smallest coefficient of variation value of 4.38%, compared against 4.62% calculated at the coordinates of the met-mast. From this spatial offset analysis it is shown that the discrepancy from the WRF results at the neighbouring points from the met-mast coordinates can be smaller than the discrepancy from the met-mast coordinates itself.

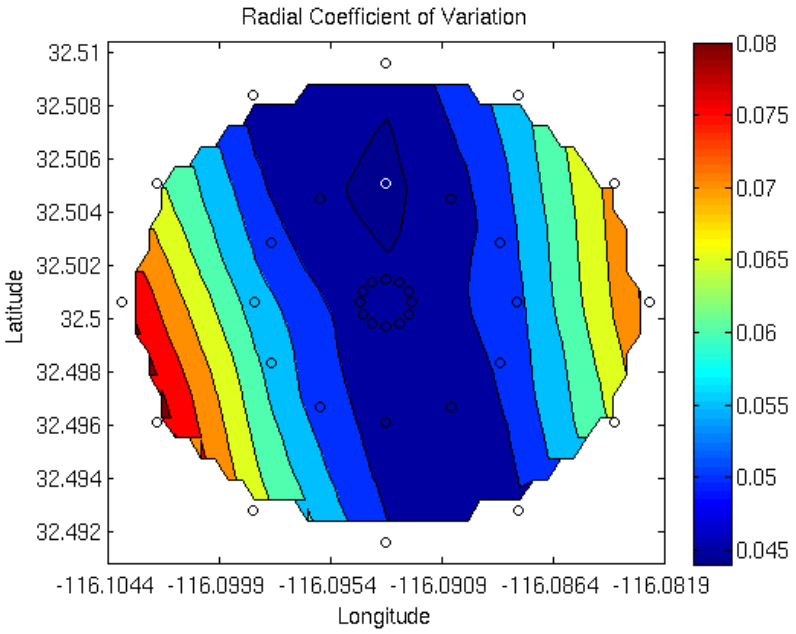

Figure 4.19 Coefficient of variation in a radial distribution.

The accuracy with which the WRF is able to predict the wind speed at 50 m height at La Rumorosa met-mast, was also performed over the four weeks aggregated period from 2014 (see Section 4.3.2.2). WRF predictions of wind speed obtained using alternative meteorological datasets and boundary layer models were evaluated against hourly samples from the met-mast (Fig. 4.20 (a-c)). Accuracy was evaluated in terms of prediction of mean wind speed, wind speed occurrence and time series. The mean wind speed value for the met-mast data is 6.44 m/s (Fig. 4.20 (a-c)). For the six simulations for this site, the mean wind speed was within 7.3% of the met-mast data. For all meteorological datasets the 5-3-1 model consistently returns higher mean wind speeds than the 5-7-1 model. For the GFS dataset (Fig. 4.20 (a)) the 5-3-1 model has a mean wind speed value of 6.52 m/s and the 5-7-1 model 5.97 m/s. The mean wind speed values for the NAM dataset were 6.31 m/s for the 5-3-1 and 6.00 m/s for the 5-7-1 configuration (Fig. 4.20 (b)). Finally, from the NARR dataset (Fig. 4.20 (c)) with the 5-3-1 configuration a mean wind speed of 6.66 m/s was obtained, while for the 5-7-1 model, the mean wind speed was 6.32 m/s.

The trend of time-variation of measured wind speed was followed by all the six simulations. The NARR provided RMSE for the distributions below 2% and the coefficient of variation was within 7%. Simulation NARR 5-3-1 (Fig. 4.20 (c)) can be considered most accurate prediction of the time-variation with RMSE and coefficient of variation of 0.6% and 7.0% respectively. The quantitative analysis for the frequency distribution and time series discrepancy is presented in Section 4.5.2 on Table 4.3.

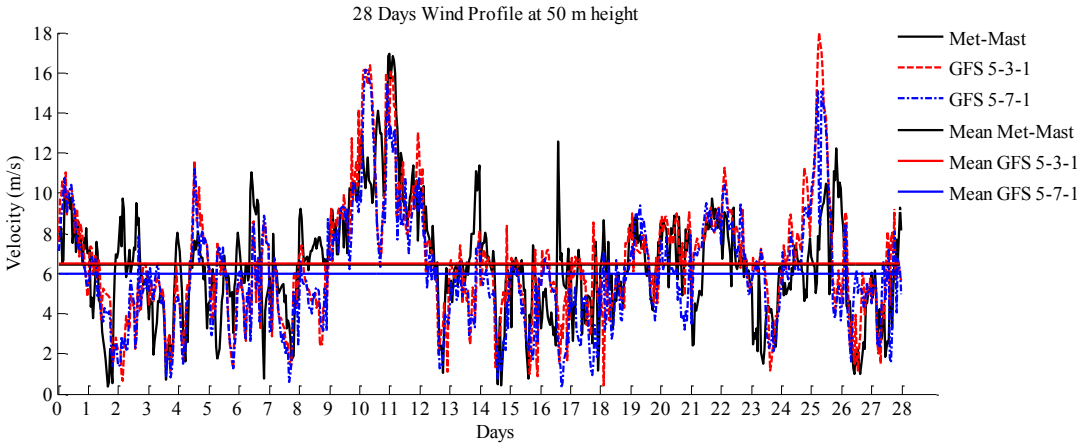

Figure 4.20 (a) Hourly time series results from WRF from GFS dataset compared against La Rumorosa met-mast data at 50 m height for 2014 aggregated period (black dashed line).

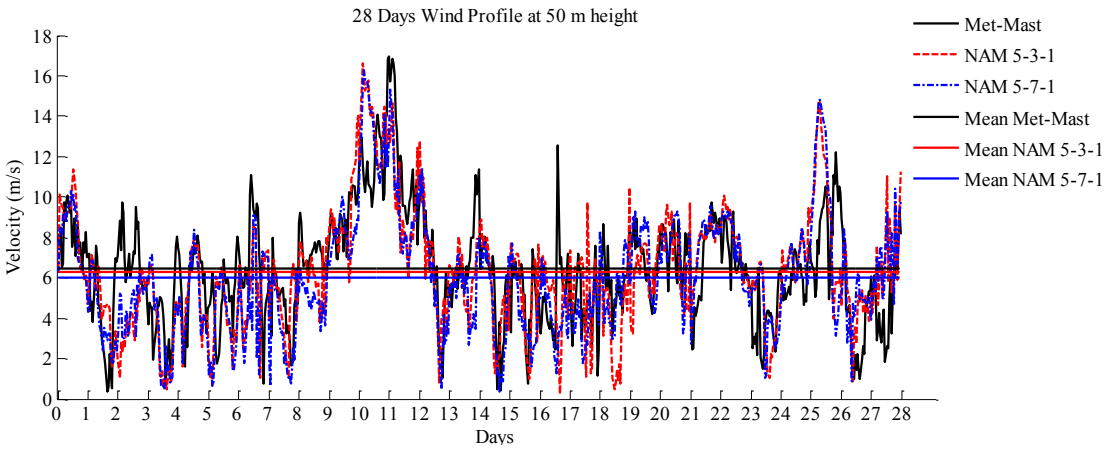

Figure. 4.20 (b) Hourly time series results from WRF from NAM dataset compared against La Rumorosa met-mast data at 50 m height for 2014 aggregated period (black dashed line).

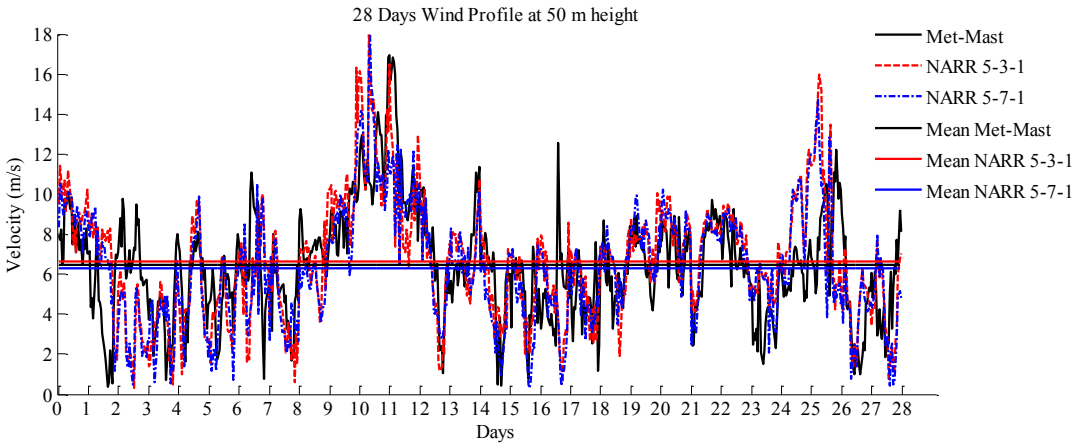

Figure. 4.20 (c) Hourly time series results from WRF from NARR dataset compared against La Rumorosa met-mast data at 50 m height for 2014 aggregated period (black dashed line).

Figure 4.21 (a-c) presents the hourly wind speed and mean met-mast data compared against the results from the WRF models per each meteorological dataset. The mean wind speed value for the met-mast data (Figure 4.21 (a-c)) was 5.85 m/s at 70 m height for the La Zacatosa met-mast. The mean wind speed values for the GFS dataset (Figure 4.21 (a)) with the 5-3-1 model was 4.91 m/s, whereas for the 5-7-1 model it was 4.74 m/s. For the NAM dataset (Figure 4.21 (b)) and the 5-3-1 model, the mean wind speed value was of 6.12 m/s, while the 5-7-1 model provided 6.07 m/s. Lastly, the NARR dataset (Figure 4.21 (c)) with the 5-3-1 configuration presented a mean wind speed value of 5.89 m/s and the 5-7-1 model 5.89 m/s. As for the point in La Rumorosa (Figure 4.20 (a-c)),the 5-3-1 model showed higher mean wind speed values compared against the 5-7-1 model for each of the meteorological dataset. For NAM and NARR datasets, mean wind speed was within 4.6% of measurement, whereas the GFS showed a discrepancy of up to 19.1%. The wind speed at 70 m height from the six WRF model configurations followed the met-mast data trend. From which, the wind speed did nit exceeded 14 m/s, lacking to describe peak wind speed values over the four weeks aggregated interval. Quantitative analysis is presented in Section 4.5.2 on Table 4.4.

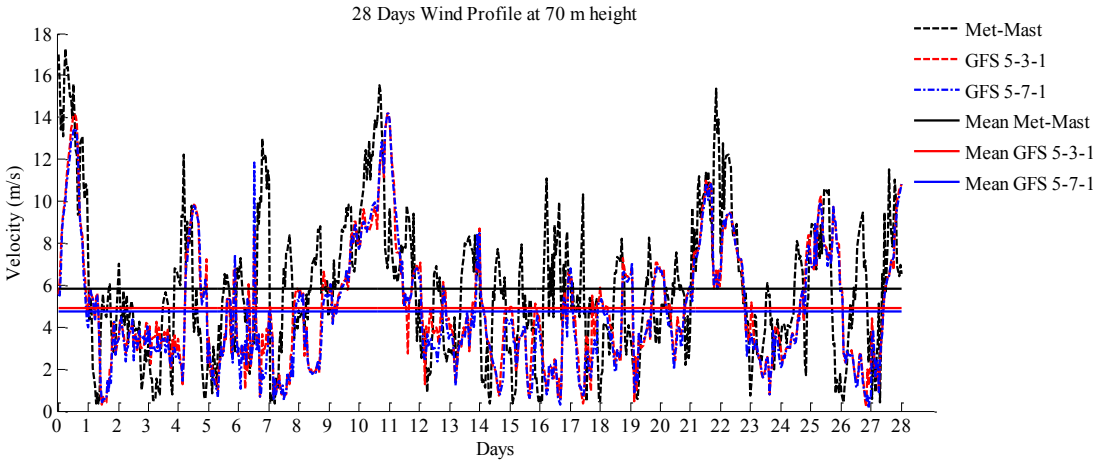

Figure 4.21 (a) Hourly time series results from WRF from GFS dataset compared against La Zacatosa met-mast data at 70 m height for 2014 aggregated period (black dashed line).

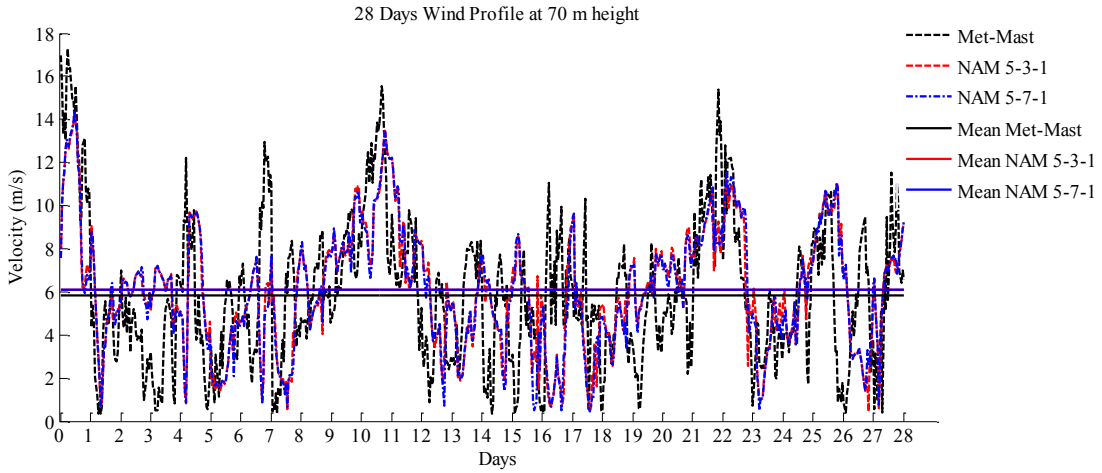

Figure. 4.21(b) Hourly time series results from WRF from NAM dataset compared against La Zacatosa met-mast data at 70 m height for 2014 aggregated period (black dashed line).

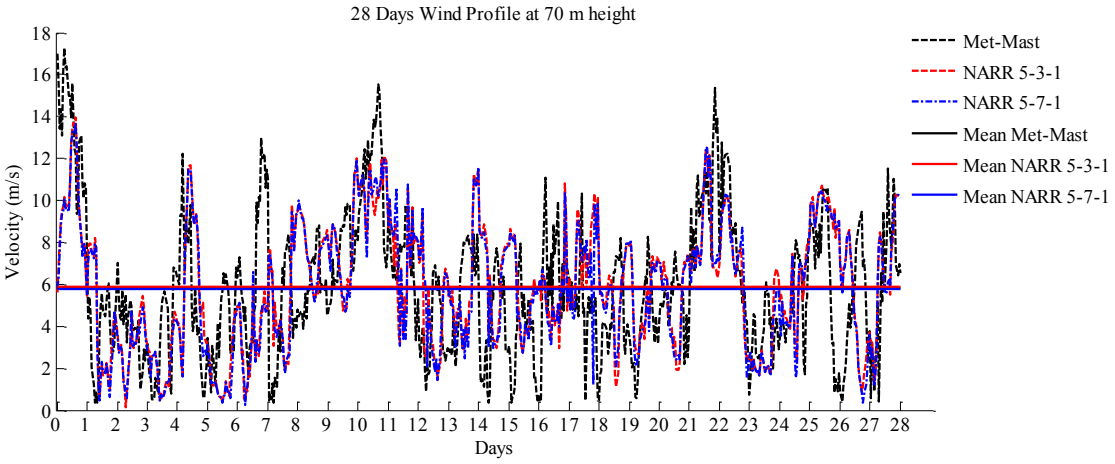

Figure. 4.21 (c) Hourly time series results from WRF from NARR dataset compared against La Zacatosa met-mast data at 70 m height for 2014 aggregated period (black dashed line).

4.5.2 Predicted occurrence of wind speed

A Weibull distribution (equation 2.8) was obtained by least squares best-fit between the predicted time-series of wind speed and the measured data at the corresponding met-mast over the same date range (Fig. 4.22). This indicates that the NARR dataset with both boundary layer models (5-3-1 and 5-7-1) underpredicts high wind speed values (12 – 20 m/s) and overpredicts medium values (5-9 m/s). Besides, both models with NAM as input described a more accurate distribution. However, there is a slight shift on the simulations Weibull distribution, compared against the met-mast data distribution.

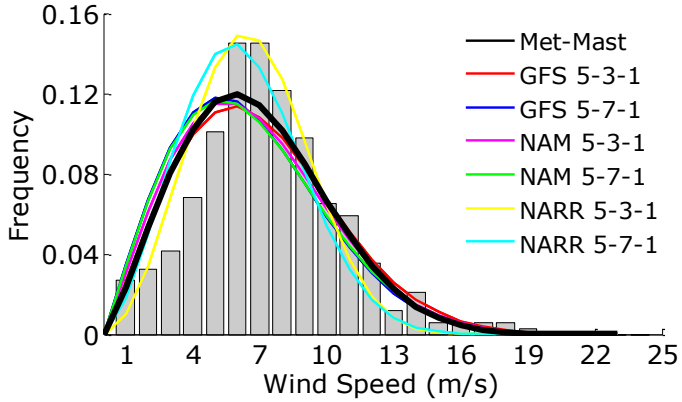

Figure 4.22 WRF Results and met-mast histograms comparison for the 2011 subset at La Rumorosa met-mast at 50 m height.

A summary of the *RMSE* defined as metrics for evaluation in equations 4.1 and 4.3, is presented in Table 4.3. The Weibull and histogram $RMSE_f$ (equation 4.1) and time series coefficient of variation (*cv)* (equation 4.4) were calculated from each one of the six time series obtained from the simulations against the met-mast data. The NARR data was the most accurate input dataset with the 5-3-1 configuration providing the lowest $RMSE_f$ of 1.8% for the histogram, while a 1.3% was obtained for the Weibull distribution and an 11.7% for the coefficient of variation.

Table 4.3 "La Rumorosa" met-mast 2011 $RMSE_f$ and *cv* analysis for WRF results.

Simulation	Histogram $RMSE_f$	Weibull $RMSE_f$	Time Series *cv*
GFS 5-3-1	2.2%	0.3%	11.8%
GFS 5-7-1	2.7%	0.6%	11.9%
NAM 5-3-1	2.3%	0.4%	11.7%
NAM 5-7-1	2.6%	0.6%	13.0%
NARR 5-3-1	1.8%	1.4%	11.7%
NARR 5-7-1	1.8%	1.1%	13.1%

The aggregated subset extracted from the La Rumorosa met-mast from the year 2014 is compared against the WRF simulations performed over these four weeks subset. Wind speed values have been interpolated at 50 m height and statistically distributed and compared against the met-mast distribution. Figure 4.23 presents the met-mast data Weibull distribution and histogram, compared against the Weibull distribution from each one of the six combinations of meteorological dataset and boundary layer model.

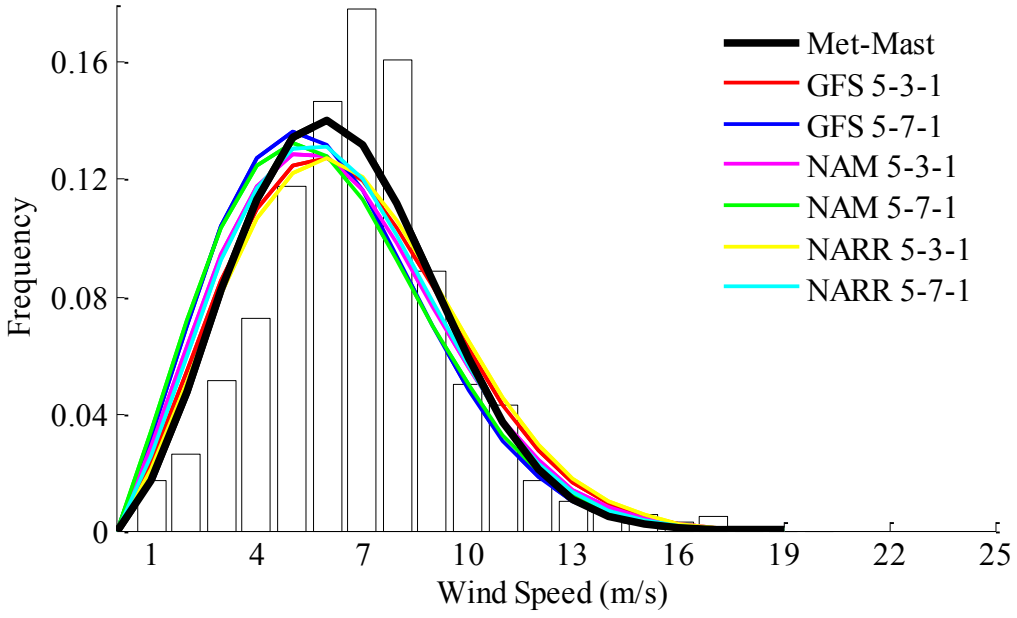

Figure 4.23 WRF Results and met-mast histograms comparison for the 2014 subset at La Rumorosa met-mast at 50 m height.

The $RMSE_f$ and *cv* metrics of evaluation defined in section 4.3.1 were applied to the WRF results for the aggregated subset from 2014 at the La Rumorosa met-mast location. For the histogram comparison (Fig. 4.23), the $RMSE_f$ (equation 4.1) presents the smallest value for the NAM 5-3-1 configuration, with a 1.2% of error for the probability. This compares to an error of 1.7% to 2.1% for all other simulations. Comparing the Weibull distribution fit, the NARR 5-3-1 results provided the smallest discrepancy with a 0.6% of error for the probability. Finally, the coefficient of variation was calculated for the time series, where the NAM 5-3-1 provided the smallest difference, of 6.2%.

A summary of the *RMSE* defined as metrics for evaluation in equations 4.1 and 4.4, is presented in Table 4.4. The Weibull and histogram $RMSE_f$ (equation 4.1) and time series *cv* (equation 4.4) were calculated from each one of the six time series obtained from the simulations against the met-mast data. The NARR data was the most accurate input dataset with the 5-3-1 configuration providing the lowest $RMSE_f$ of 1.7% for the histogram, while a 0.6% was obtained for the Weibull distribution and a 7.0% for the coefficient of variation. The NARR 5-3-1 is the WRF configuration which provides best fit in terms of the analysis performed.

Table 4.4 "La Rumorosa" met-mast 2014 $RMSE_f$ and *cv* analysis for WRF results.

Simulation	Histogram $RMSE_f$	Weibull $RMSE_f$	Time Series *cv*
GFS 5-3-1	1.2%	0.6%	7.3%
GFS 5-7-1	2.1%	1.1%	8.6%
NAM 5-3-1	1.2%	0.8%	6.2%
NAM 5-7-1	2.4%	1.2%	8.9%
NARR 5-3-1	1.7%	0.6%	7.0%
NARR 5-7-1	1.8%	0.6%	5.2%

As it has been mentioned, for the year 2014, data from two met-masts is available, so far, the WRF results have been compared for the data from La Rumorosa. Below, the analysis will be performed for the same subset of 2014 but for the met-mast located at La Zacatosa.

The aggregated subset extracted from the met-mast at La Zacatosa from the year 2014 is compared against the WRF simulations performed over these four weeks subset. Weibull distribution has been calculated for each one of the simulations and the met-mast data for the aggregated subset. A comparison of the Weibull distribution is presented on Figure 4.24, distributions seemed to be grouped by meteorological datasets rather than by parameterization models. Both GFS distributions tend to underestimate the wind speed values. Otherwise, the NAM datasets overestimate in greater percentage the met-mast distribution, compared against the NARR dataset which have the less discrepancy matching the measured data.

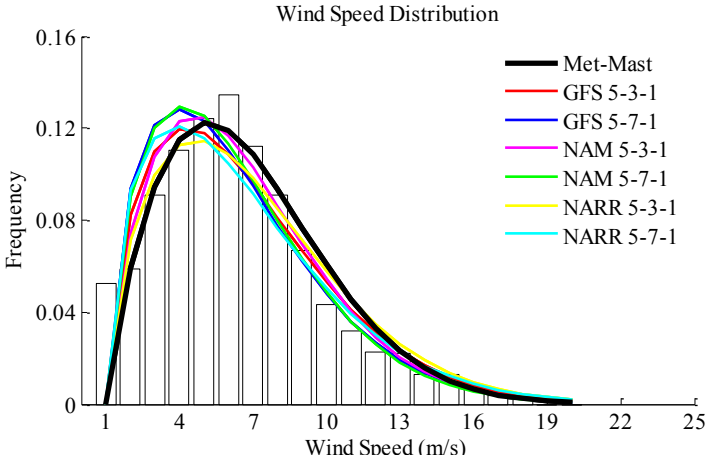

Figure 4.24 WRF Results and met-mast histograms comparison for the 2014 subset at La Zacatosa met-mast at 70 m height.

4.5.3 Predicted occurrence of wind speed and direction

The accuracy of the WRF model to reproduce both, met-mast wind speed and direction data is evaluated in this subsection. The wind rose distributions have

been calculated from the WRF simulations and $RMSE_\theta$ (equation 4.2) based on the La Zacatosa 80 m height met-mast wind rose distribution for year 2014 (Fig. 4.25). As these simulations were performed over a single domain, the wind rose distribution has a greater variation compared against the met-mast data. From the results, the NARR 5-3-1 was the one with the smallest distribution error, being 26.5% compared against the wind rose distribution from La Zacatosa met-mast shown on Figure 4.25.

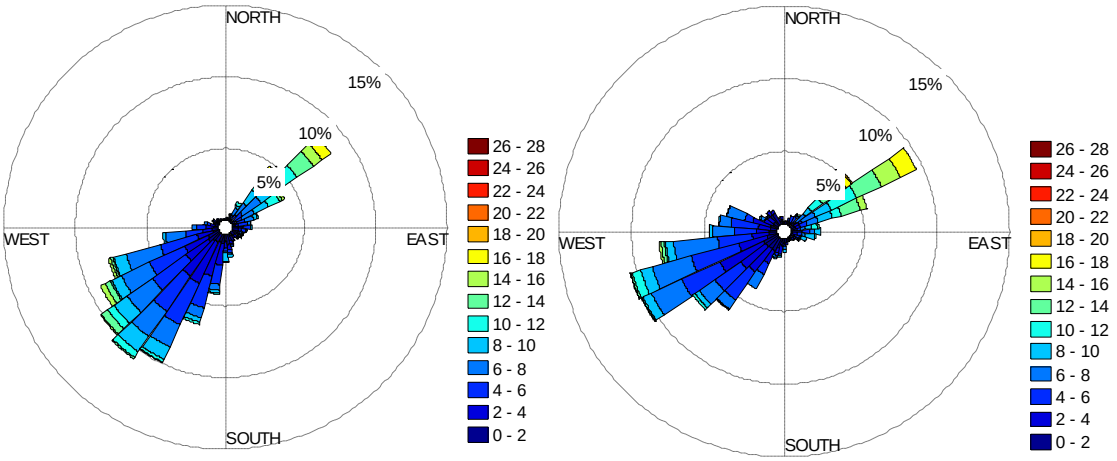

Figure 4.25 Wind rose distribution from the La Zacatosa met-mast data (left) and from the NARR 5-3-1 results (right) for the 2014 aggregated period.

Table 4.5 summarizes the discrepancy from each WRF simulation. As shown on Figure 4.24, the GFS results provided greater error, followed by the NAM simulations. Finally, the NARR analysis provided better agreement for all the indexes. Additionally, from this meteorological dataset, the NARR 5-3-1 configuration has been the optimum from those simulated.

Table 4.5 "La Zacatosa" met-mast 2014 *RMSE* analysis for WRF results.

Simulation	Histogram $RMSE_f$	Weibull $RMSE_f$	Time Series cv	Wind Rose $RMSE_\theta$
GFS 5-3-1	2.6%	1.4%	18.6%	45.4%
GFS 5-7-1	3.1%	1.7%	21.2%	46.6%
NAM 5-3-1	2.0%	1.6%	12.8%	41.5%
NAM 5-7-1	1.8%	1.4%	11.5%	43.4%
NARR 5-3-1	1.5%	0.9%	11.5%	26.5%
NARR 5-7-1	1.6%	0.7%	11.3%	28.1%

Based on the wind resource evaluated from the 2014 sample, the NARR 5-3-1 configuration will be applied to analyse the wake effect from potential wind farms (Chapter 6), by populating the pieces of land which have been showed on Figure 4.16 and by applying the Fitch (2012) scheme over those points.

4.5.4 Prediction of wind farm energy yield

The wind energy yield from each model configuration was calculated from the two consecutive weeks wind speed time series (Section 4.3.2) and the wind turbine manufacturer power curve (Section 4.2). Wind speed values were extracted at hub height from each wind turbine location. Wind energy yield relative error (equation 4.5) was calculated for each meteorological dataset and WRF model combination. Figure 4.26 shows discrepancy between the predicted energy yield and the measured SCADA data from 2011 (Section 4.3.3). The simulation case GFS 5-7-1 predicts aggregate energy output of 1.055 GWh, an error of -1.04% compared against the measured farm yield over the same date range.

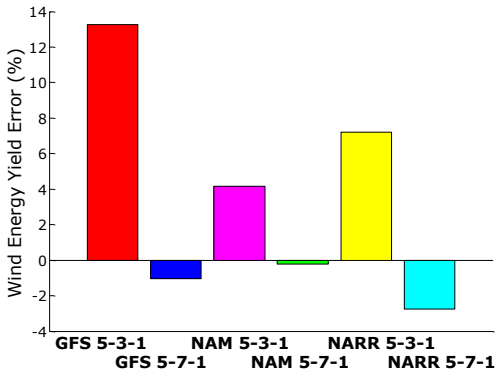

Figure 4.26 Energy yield difference from WRF simulations and real performance for the selected 2011 subset.

The same process was applied to the predictions for the four weeks aggregated subset from 2014 (Section 4.3.2). As it has been mentioned, meteorological data over the area of La Rumorosa for the year 2014 has been acquired for two locations 16 km apart, from which wind speed from the simulations for the aggregated subset have been analysed.

For this time-interval, the NARR 5-3-1 WRF model configuration (Table 4.4) is the one which has been identified as the best-fit case for the La Rumorosa met-mast data, which is located beside the "La Rumorosa I" wind farm. From this configuration (NARR 5-3-1), 2.047 GWh were calculated with a wind energy yield relative error (equation 4.5) of 5.25% compared against the measured wind energy yield from the "La Rumorosa I" farm for the same aggregated subset (Fig. 4.27).

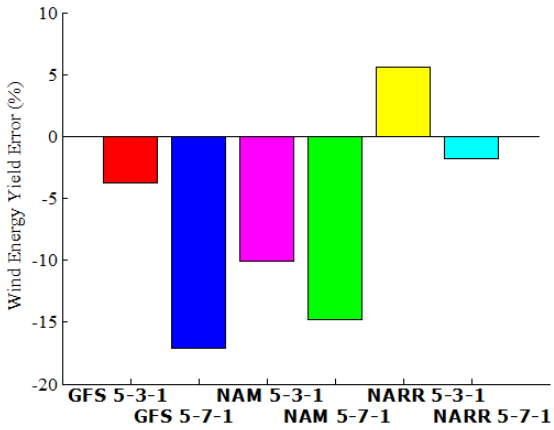

Figure 4.27 Energy yield difference from WRF simulations and real performance for the selected 2014 subset.

4.6 Conclusions

The WRF model has been evaluated in terms of accuracy of prediction of wind speed and wind direction and energy yield of a small wind farm by comparison to data from met-masts at a wind farm located in Baja California. A 31.2 km by 31.2 km area of La Rumorosa on the Northwest of Mexico has been studied for which data for up to two years is available from two met-masts and five wind turbines.

Date ranges of up to four week duration were identified during 2011 and 2014, for which the wind speed Weibull and wind rose distributions represented the annual and wind rose distribution. For 2011, two consecutive weeks were selected from 26th of October to 8th of November 2011; their Weibull distribution and histogram compared against La Rumorosa met-mast annual data were within 0.0962% and 0.8162%, respectively, which justified the basis for selecting this two week subset. For 2014 four different weeks, each one from a different season of the year, were selected based on the similarity to represent the wind speed and direction distribution from La Zacatosa met-mast annual data. These subsets were from the 6th to 12th of January, plus 3rd to 9th of May, with 31st of July to 6th of August, and finally, 26th of November to 2nd of December 2014.

Weibull distribution, histogram and wind rose distribution compared against annual data were within 0.405%, 0.307% and 9.242%, respectively.

WRF models with five nested domains have been run to assess accuracy of wind speed prediction at the La Rumorosa met-mast and energy yield prediction from the "La Rumorosa I" wind farm during the identified date ranges. Six different simulations have been compared, covering three different meteorological datasets as input and two different parameterization schemes for the land surface model option. The WRF simulation with the NARR 5-3-1 configuration provided the most accurate results, with a histogram RMSE of 1.8%, 1.4% for the Weibull distribution and a coefficient of variation of 11.7% for the time series. Wind energy yield was overpredicted within an 8% of error for the consecutive two weeks subset. This was expected, as WRF overpredicts low wind speed values during the two weeks period.

The four weeks aggregated subset from 2014 was compared against both La Zacatosa and La Rumorosa met-masts, and against the wind farm operational data. From the results compared at the La Rumorosa met-mast, the NARR 5-3-1 configuration model showed a 1.7% RMSE value for the histogram distribution, 0.6% RMSE for the Weibull distribution and a coefficient of variation of 7.0% for the time series.

This subset was compared against the La Zacatosa met-mast data, including a wind rose comparison. From the same configuration model, NARR 5-3-1, the wind speed values were interpolated at 80 m height and compared for this site. Values provided a 1.5% for the histogram RMSE, 0.9% for the Weibull RMSE and 11.5% for the coefficient of variation. Additionally, the wind rose distribution was described within a RMSE of 26.5%.

The wind energy yield was calculated at the location of each one of the five wind turbines from the La Rumorosa I wind farm. From the WRF simulations the wind energy yield for the 2014 four weeks aggregated subset was predicted

within a 5.25% of error. WRF wind rose results differed from the met-mast data, which can be a reason why this error is higher compared against the 2011 analysis.

The WRF configuration NARR 5-3-1 will be the one applied to analyse the intra and inter wind farm wake effects in Chapters 5 and 6, respectively, due to it provided a better agreement to describe both wind speed and direction statistical distribution (i.e. wind rose) compared against the 80 m height La Zacatosa met-mast for the aggregated period from 2014, which is directly upstream the existing farm for the predominant direction and the potential cause of wind energy yield deficit due to the operation of a potential wind farm within the vicinity of this point.

Chapter 5 Wind turbine parameterization model evaluation

The main objective of this chapter is to assess the wake effect over each turbine when the wind is blowing in a direction aligned to the La Rumorosa I wind farm layout, this being from an angle between 145° to 165° when blowing from the South-Southeast, or between 325° to 345° when blowing from North-Northwest. This is to quantify the effects from the upwind over the downwind turbines and compare WRF simulations addressing the effects of these turbines over the flow against operational data from a single row wind farm with wake interaction. Ten-minute met-mast wind speed and direction data are available (CFE, 2014), and wind speed, power and wind speed direction data from the wind farm SCADA system for each wind turbine from the year 2014 (State of Baja California, 2014). To get the data samples within these ranges of direction, 52,560 readings from the met-mast and wind turbine were examined.

5.1 Introduction

The wind turbines from La Rumorosa I wind farm are referred as AEG-1 to AEG-5 from North to South. From AEG-1 to AEG-5 there is a bearing of 155° (Fig. 5.1). Turbines' diameter is 87 m and their height is 78 m, on top of the nacelle from each turbine there is an anemometer and a wind vane, so the yaw is selected on the basis of the anemometer, which averages the wind speed and direction every ten minutes.

This chapter presents a review of work done to predict the wake from upstream to downstream wind turbines within the same wind farm, performed with Numerical Weather Prediction models, specifically the Weather Research and Forecasting model (Section 5.2). An offset angle was found for the wind direction time series from each wind turbine against the met-mast. To correct this angle, Section 5.3 presents the methodology and two cases to identify these offset values and align the wind direction based on the met-mast readings.

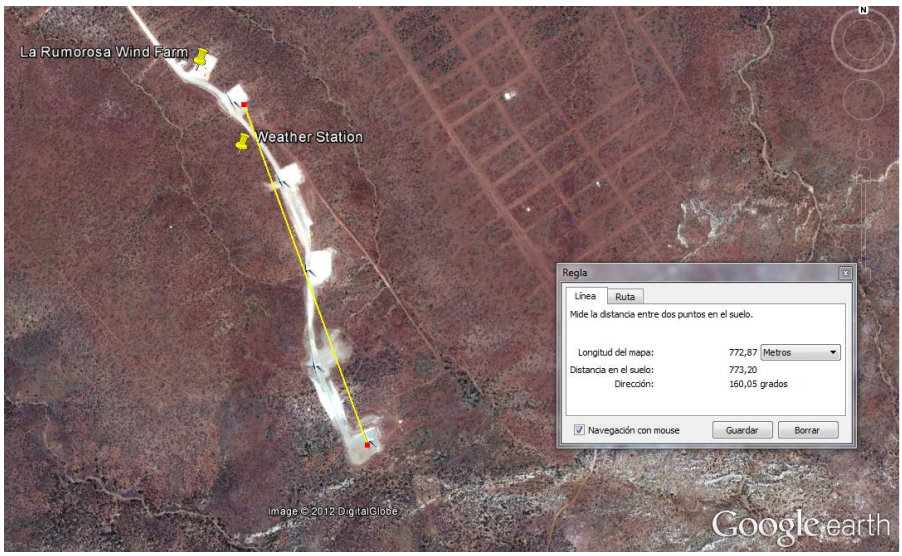

Figure 5.1 Wind turbines and met-mast layout (Google, 2012).

Section 5.4 presents the filtering of the data which showed wind direction aligned to the wind farm layout for both of the offset correction cases from Section 5.3.

Data from the South-Southeast wind direction are presented for mean and single time steps values tabulated and graphically to show the interaction within the farms based on the wind speed, direction and power from the turbines (Section 5.5).

A WRF simulation has been conducted to reproduce numerically the wind speed and direction from the cases above mentioned, results obtained are tabulated and presented graphically in Section 5.6.

Finally, conclusions on the analysis performed, advantages and limitations of the wind turbine parameterization scheme (Fitch et al., 2012) from the WRF model are summarized in Section 5.7.

5.2 Review of literature for wake effects within wind farms from WRF

As the WRF has been able to represent the wind resource at met-mast and hub heights, different methods to represent the effects of operating wind turbines over the wind flow have been implemented (Singer et al., 2010; Blahak et al., 2010; Fitch et al., 2012; Volker et al., 2012). Additionally, these schemes have

been applied to evaluate the interaction between wind turbines within a wind farm.

Lindvall et al. (2015) performed a sensitivity analysis on the horizontal and vertical resolution for an onshore wind farm. Nine days were selected, where the wind from the Southwest predominated. The high vertical resolution considered 10 levels at the lowest 250 m height with 333 m horizontal resolution, compared against 5 from the general 1km horizontal resolution. Results were compared against operational data and showed the importance of the horizontal grid to resolve the effects of each individual turbine. For the power calculations and internal wake losses the high horizontal resolution showed a better agreement against the observed wind farm data. Fractional production for distances away from the front row of turbines was better described with the high horizontal resolution than with the high vertical resolution simulation.

Following the methodology from Chapter 4, the Horns Rev offshore wind farm was considered for the year 2007, this has been reported by Stylianou et al. (2015). Wind fields at hub height over the wind farm were obtained for the year 2007 from the ERA-interim meteorological dataset, from which, an aggregated five weeks subset period was selected based on the similarity of the statistical distribution to the annual distribution, with a RMSE of 1.03% and 0.12% for the histogram and the Weibull distribution, respectively. For the corresponding aggregated periods, WRF model simulations were performed with four nested domains with resolutions from 30.240 km down to 1.120 km. The WRF wind turbine parameterization model (Fitch et al., 2012) was applied over the wind farm. The ERA-Interim data for 2007 overpredicted by 13% the annual energy yield, while the WRF model of 1.120 km resolution by 4% only. ¨Power curves were obtained using the PARK and Eddy Viscosity models in OpenWind to represent up to four turbines within a cell. The resultant energy yield was

reduced by 2.3% compared against use of the standard Fitch et al. (2012) model for the aggregated period.

5.3 Data processing to correct wind turbines direction

The wind vane at the top of each wind turbine nacelle has been set with different reference heading. In this way, after comparing the wind direction time series from each wind turbine against the met-mast data (which has been set with 0° to the North), an offset angle has been shown. In order to correct the offset from each wind turbine data set against the met-mast values, two approaches have been taken.

The first method calculates the offset for the time steps which provide a met-mast wind direction between 20° and 110°; they have been filtered for both the met-masts and for each one of the wind turbines (Subsection 5.3.1), secondly, for the time steps where the wind is blowing from an angle within 200° and 290° (Subsection 5.3.2), perpendicular to the wind farm layout, but with an opposite direction from the previous method.

For each of the approaches, the difference between the met-mast and each of the wind turbines direction is calculated (equation 5.1).

$$\theta_{o(i)} = \theta_{mm(i)} - \theta_{AEG(i)} \tag{5.1}$$

where θ_o is the offset of the angle in degrees, θ_{mm} is the angle measured at the met-mast in degrees, θ_{AEG} is the angle measured at each of the wind turbines (AEG-1 to AEG-5), and finally i is the time step corresponding to ten minutes readings.

Therefore, from each group of offset angle from each wind turbine, the value that appears most often from each wind turbine offset is identified as the corresponding mode. Finally, this mode is applied to correct all the sets of angle data from each wind turbine (equation 5.2).

$$\theta_{c(i)} = \theta_{AEG(i)} - \theta_m \quad (5.2)$$

θ_c is the corrected angle in degrees and θ_m is the angle which appears more often for each wind turbine offset in degrees.

5.3.1 Wind direction from 20° to 110°

Data were filtered considering the met-mast wind direction within the angles of 20° and 110° (Fig. 5.2) for all ranges of wind speed. An amount of 14,452 readings were obtained, corresponding to 27.5% of the annual data.

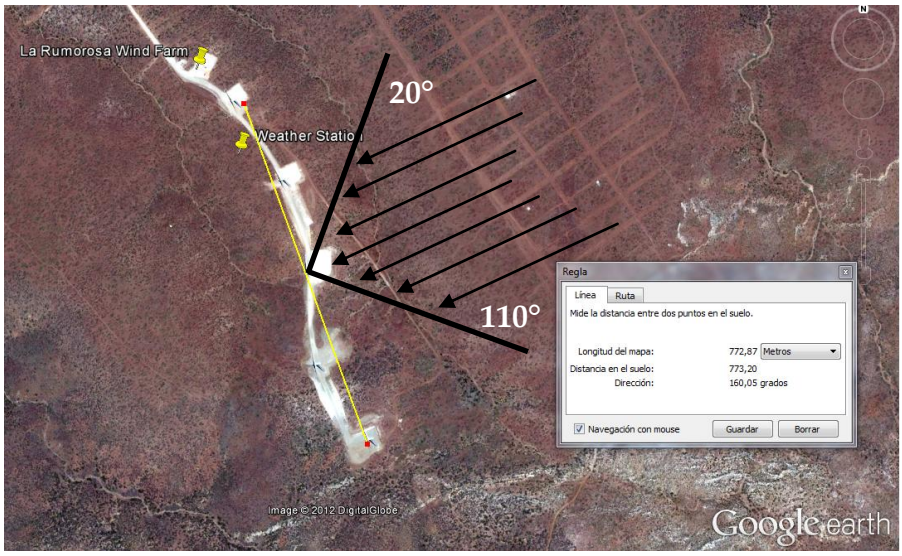

Figure 5.2 Met-mast wind direction selected for wind turbines direction correction.

After calculating the offset from each of the wind turbines against the met-mast from the range between 20° and 110°, the offset angle which is present most frequently for each wind turbine is -174° for AEG-1, -26° for AEG-2, -43° for AEG-3, 4° for AEG-4 and -35° for AEG-5 (Table 5.1).

As an example of the fit from the offset calculated, an angle of -35° was added over all the values from the AEG-5 data, and the corrected scatter plot is presented in Figure 5.3. By correcting the offset the set of values is displaced

downwards and brings the wind turbine angle values to diagonal linear correspondence.

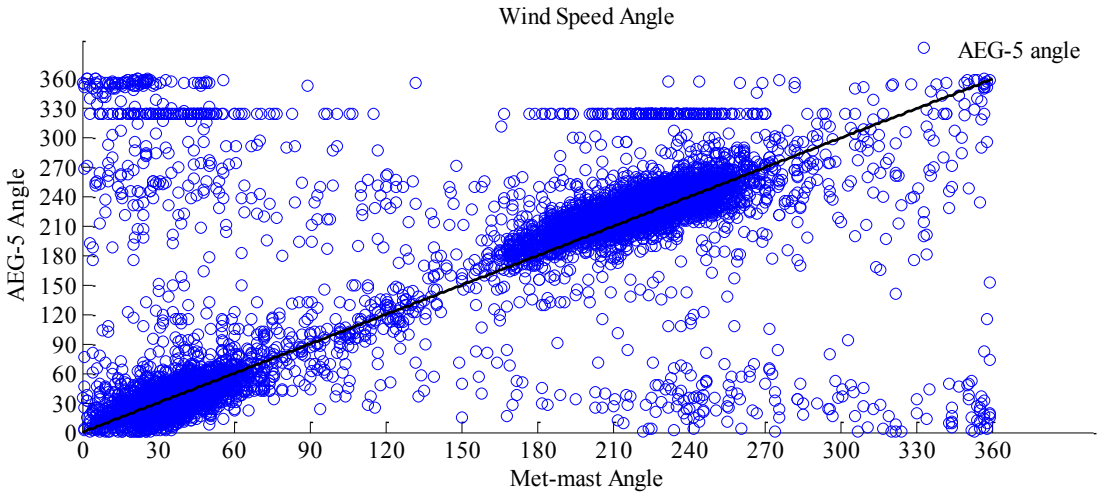

Figure 5.3 met-mast and AEG-5 scatter plot.

5.3.2 Wind direction from 200° to 290°

Similar to previous section, the met-mast data was filtered to identify the time steps when the wind was blowing form a direction between 200° and 290° for all the wind speed values recorded. For this approach 28,751 samples were found within this range of angles, conforming a 54.70% of the total readings.

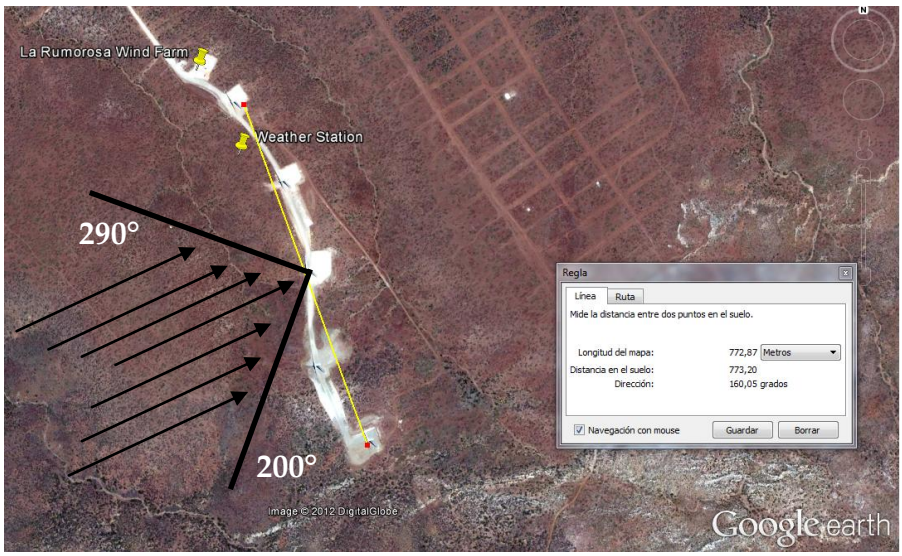

Figure 5.4 Met-mast wind direction selected for wind turbines direction correction.

The offset analysis methodology explained in Section 5.3 was applied for the met-mast readings with angle values ranging from 200° to 290° (Fig. 5.4), to calculate the offset angle from each wind turbine against the met-mast. The offset angle values obtained most frequently for each wind turbine were 32° for AEG-1, -31° for AEG-2, -52° for AEG-3, -3° for AEG-4 and -40° for AEG-5 (Table 5.1).

To illustrate the results of this method, the offset angle of -40° obtained for the AEG-5 by taking into account the met-mast values with an angle from 200° to 290°, was applied to the annual ten-minute time steps for AEG-5. The scatter plot which compares the corrected angle for the AEG-5 wind turbine is presented in Figure 5.5, where a linear dependence can be seen .

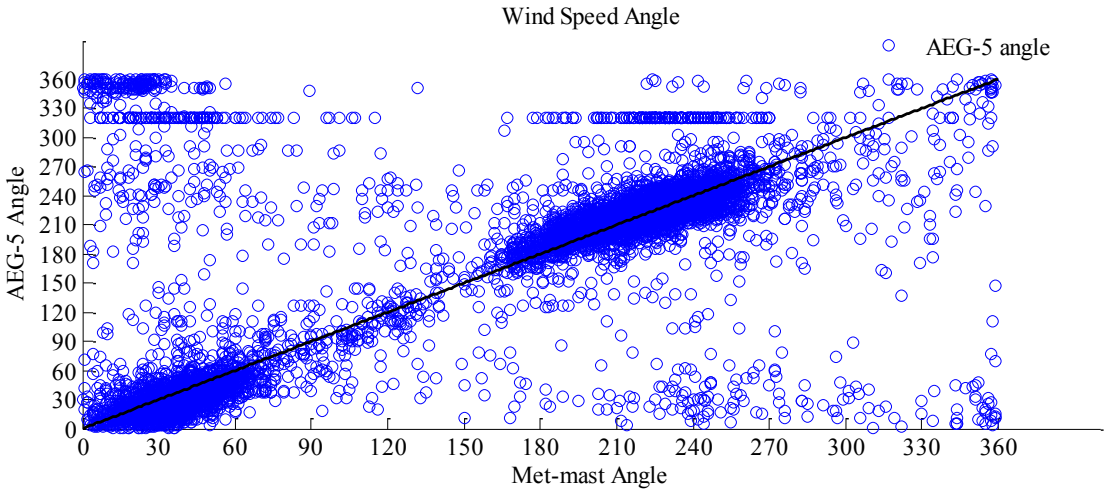

Figure 5.5 Met-mast and AEG-5 scatter plot.

Table 5.1 presents the value which appears most often from each wind turbine offset analysis. From the datasets filtered, the data set from the angles between 200° and 290° is the one with the largest sample size. The offset values from this approach will be considered in the following section to identify the time steps when the wind flow is aligned to the wind farm layout.

Table 5.1 Mode offset from each turbine against the met-mast for directions.

Wind Turbine	20° to 110°	200° to 290°
AEG-1	-174	32
AEG-2	-26	-31
AEG-3	-43	-52
AEG-4	4	-3
AEG-5	-35	-40

5.4 Wind direction aligned to the farm

After correcting the offset angle from each of the wind turbines (Subsection 5.3.1-5.3.2) samples were identified which satisfied the following criteria:

- heading in the range 145° to 165° and 325° to 345°, i.e. within 5° of the bearing between turbines 1 and 5.
- wind speed within the wind turbine operative range (4 to 25 m/s).

These values are grouped in three sections (Tables 5.2), the number of samples from the met-mast for each of the turbines with wind on these directions, the number of samples with the met-mast along with any 1 to 5 wind turbines and finally, the number samples with the met-mast along with the wind turbines AEG-1 to AEG-5. This last group is in order to identify the number of readings available from each direction with the met-mast and the corresponding front wind turbine, AEG-5 for the wind speed from 145° to 165 and AEG-2 for the angles between 325° and 345°.

5.4.1 Selection of samples with wind speeds within operating range and headings between 200° and 290°

From the offset correction methodology presented in subsection 5.3.2, the number of samples for both wind directions aligned to the wind farm have been selected. For the wind direction from South-Southwest (145° to 165°) 45 time steps were found matching the met-mast and the AEG-5 at the same time. On

the opposite direction, when the wind blows from the North-Northwest (325° to 345°), only 4 met-mast and AEG-2 time steps matched both wind directions (Table 5.2). In all cases there was at least one turbine not operating due to the low wind speeds.

The amount of readings from Table 5.2 varies because the offset angle values were close but not the same for both offset correction methodologies presented on Subsections 5.4.1 and 5.4.2.

Table 5.2 Amount of time steps after correcting wind turbines angle based on Section 5.3.1 for met-mast directions between 145° and 165°.

Criteria	Direction between 145° and 165°		Direction between 325° and 345°	
	Over all Speed Range	**Operative Speed Range**	**Over all Speed Range**	**Operative Speed Range**
***U* met-mast in range**	394	203	292	38
***U* AEG-1 in range**	363	149	538	100
***U* AEG-2 in range**	395	195	231	580
***U* AEG-3 in range**	330	166	285	75
***U* AEG-4 in range**	420	190	242	39
***U* AEG-5 in range**	377	149	169	63
***U* met-mast + 1 *U* AEG**	55	16	44	3
***U* met-mast + 2 *U* AEG**	18	16	22	3
***U* met-mast + 3 *U* AEG**	41	30	8	3
***U* met-mast + 4 *U* AEG**	16	12	9	1
***U* met-mast + 5 *U* AEG**	0	0	0	0
***U* met-mast + *U* AEG-1**	33	9	28	1
***U* met-mast + *U* AEG-2**	62	42	48	**4**
***U* met-mast + *U* AEG-3**	49	27	32	4
***U* met-mast + *U* AEG-4**	77	52	48	1
***U* met-mast + *U* AEG-5**	67	**45**	22	2

5.5 Variation of wind speed and power with turbine position

5.5.1 Mean during turbine operation

From the analysis to correct the offset angles presented in subsection 5.4.1, 45 time steps were obtained for the wind direction between 145° and 165°. Some of

these did not have all the five wind turbines operating, which were discarded, others had the wind speed values over the rated value, which were not taken into account, reducing to finally, from 22 time steps calculation of the mean wind speed and angle, as well as power and power coefficient for the wind turbines (Table 5.3). Additionally, from these readings, the AEG-1 turbine presented a predominant offset angle of 56°, from which it had to be applied to all the readings from AEG-1 to correct the wind direction, this correction was applied only for this subset of readings particularly for AEG-1.

Table 5.3 Met-mast and wind turbines averaged angle, speed, power and C_p values between 145° and 165°.

Source	Long	Lat	Height	θ_{AEG}	U	u	v	Power	C_p
Met-mast	-116.091	32.498	1,358	154.29	5.25	-2.28	4.73	n/a	
AEG-1	-116.091	32.499	1,358	154.60	5.93	-2.55	5.36	330.08	0.41
AEG-2	-116.090	32.498	1,371	155.06	6.16	-2.60	5.59	293.98	0.32
AEG-3	-116.089	32.496	1,361	152.76	3.79	-1.74	3.37	97.53	0.40
AEG-4	-116.089	32.494	1,385	149.85	6.37	-3.20	5.51	315.53	0.32
AEG-5	-116.088	32.493	1,371	159.13	5.88	-2.10	5.50	278.62	0.35

Figure 5.6 illustrates the variation of wind direction and turbine power output with position. For the averaged values, wind blows from the South-Southwest, AEG-5 is the first in line, which has a wind speed of 5.88 m/s and a power output of 278.62 kW, AEG-4 is not completely in line, which has a higher wind speed value of 6.37 m/s and 315.53 kW, this can be explained from two reasons, its elevation is 14 m over the AEG-5 and due to a small hill between the AEG-5 and the AEG-3, which deflects the wake. Both of these wind turbines and the hill affect the resource at AEG-3, which the corresponding hub height is located 10 m below the AEG-4 and gets a reduced wind speed value of 3.79 m/s just below the cut-in value. This occurs entirely in wake of the upwind AEG-5 and

AEG-4 turbines. However, there is still an average power output of 97.53 kW, which for such low mean wind speed would be expected to be zero. This is presumably due to significant variation of power output during the ten minute sample. At AEG-2, which its hub height is 10 m over the AEG-3's hub height, the wind speed value reaches 6.16 m/s and a power of 293.98 kW. Lastly, AEG-5 receives the wind flow affected due to the performance of AEG-2, with wind speed value of 5.39 m/s and producing 330.08 kW, which is averaged over a 10 min period. As these values represent the mean of each wind turbine speed and power for this wind direction, the power and speed might not be correspondent to the power curve.

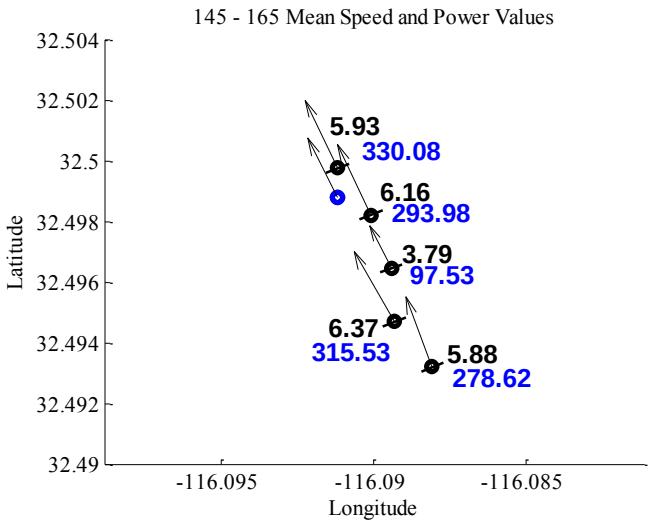

Figure 5.6 Met-mast (blue circle) and wind turbines (black circles) quiver, wind speed (black number) and power (blue number) for averaged values between 145° and 165°.

In a similar way, the distribution of the averaged power coefficient values is presented for each wind turbine (Fig. 5.7) where AEG-5 has a value of 0.35, and AEG-4 a similar value of 0.32, AEG-3 has a higher value 0.40 due to power for such a low mean wind speed value. AEG-2 has a 0.32 value for the mean of the power coefficients and AEG-5 has a value of 0.41.

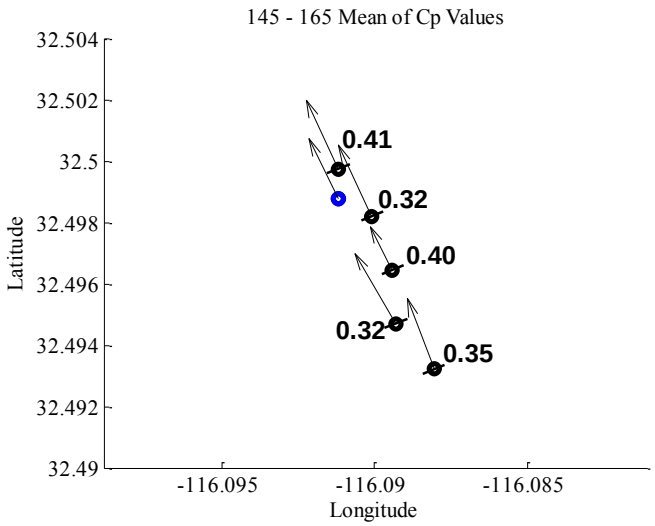

Figure 5.7 Met-mast (blue circle) and wind turbines (black circles) power coefficient for averaged values between 145° and 165°.

Table 5.4 presents the corresponding wind speed and the calculated power coefficient for the wind speed and electric power from each turbine, together with the manufacturer's power coefficient ($C_{P(u)}$) and thrust coefficient ($C_{T(u)}$). Averaged values present lower power coefficients compared against the manufacturer data, with exception of the AEG-3, for which the values of power and hence power coefficient are both zero, because the cut-in wind speed for this turbine model is 4 m/s, and its value is under the operative range.

Table 5.4 Wind turbines speed, Manufacturer C_p and Operation C_p for averaged values between 145° and 165°.

Wind Turbine	Speed (m/s)	Operation C_p	$C_{P(u)}$	$C_{T(u)}$
AEG-1	5.93	0.41	0.425	0.812
AEG-2	6.16	0.32	0.429	0.812
AEG-3	3.79	0.40	0.000	0.000
AEG-4	6.37	0.32	0.433	0.812
AEG-5	5.88	0.35	0.424	0.812

The analysis of these averaged values help to identify operative ranges for wind speed and power along the wind farm for wind speed values between the cut-in and rated power.

5.5.2 Single values over wind speed operative range

Additionally, from the identified time steps to calculate the averaged values in Subsection 5.6.1.1, a single time step was selected which shows a reduction on the wind speed from AEG-3 which is just above the cut-in value without causing the turbine to stop. As the wind turbines have a starter motor which spins them to begin energy production when the generator is activated, it also operates for a short period when the velocities decrease to avoid the generator being disconnected from the grid.

The ten-minute time step chosen presents the wind blowing from the South-Southwest with a wind speed and direction, wind turbines wind speed values range from 4.30 m/s to 6.31 m/s, with direction for the turbines from 153.30° to 161.08°. The power values go from 94.57 kW to 387.36 kW, with power coefficients from 0.33 to 0.43, for these respective speeds (Table 5.5), where u is the east–west component of wind and v is the north–south component of wind.

Table 5.5 Met-mast and wind turbines angle, speed, power and C_p values between 145° and 165° for a single time which reduces the power over AEG-3.

Source	Long	Lat	θ_{AEG}	U	u	v	Power	C_p
Met-mast	-116.091	32.498	157.00	5.00	-1.95	4.60		
AEG-1	-116.091	32.499	157.48	6.29	-2.41	5.81	387.36	0.43
AEG-2	-116.090	32.498	157.31	6.31	-2.43	5.82	302.33	0.34
AEG-3	-116.089	32.496	153.55	4.30	-1.91	3.85	94.57	0.33
AEG-4	-116.089	32.494	153.30	6.22	-2.79	5.56	297.63	0.35
AEG-5	-116.088	32.493	161.08	6.01	-1.95	5.69	273.57	0.35

For this ten-minute time step the met-mast wind speed and direction are 5 m/s and 157°, respectively. AEG-5 has a wind speed value of 6.01 m/s and a power of 273.57 kW, speed and power increase to 6.22 m/s and 297.63, which then decrease to 3.85 m/s at AEG-3 with a power of 94.57 kW. The last two wind turbines on the wind direction, AEG-2 and AEG-1 present wind speed values of

6.31 m/s and 6.29 m/s, and a power output of 302.33 kW and 387.36 kW, respectively (Fig. 5.8).

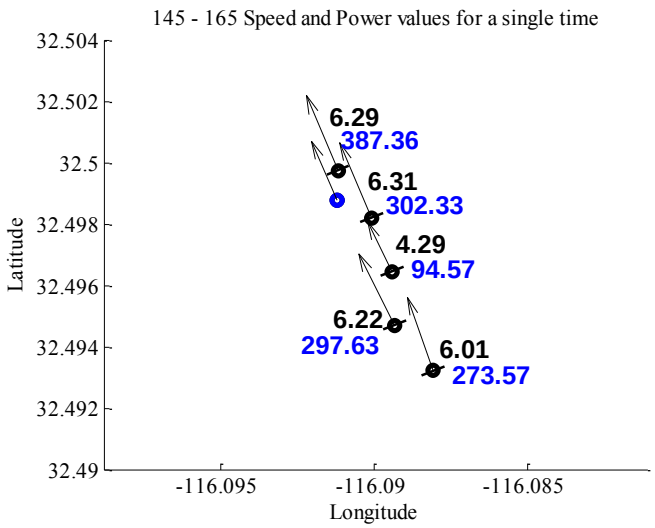

Figure 5.8 Met-mast (blue circle) and wind turbines (black circles) quiver, wind speed (black number) and power (blue number) for values between 145° and 165° for a single time which reduces the power over AEG-3.

Power coefficient values were calculated for each of the wind turbines based on equation 2.6, considering the hub-height wind speed and the power from the generator. AEG-5 and AEG-4 have a power coefficient of 0.35, which decreases at AEG-3 to 0.33, and then increases to 0.34 at the AEG-2 to finally, reach a 0.43 value for the AEG-1 (Fig. 5.9).

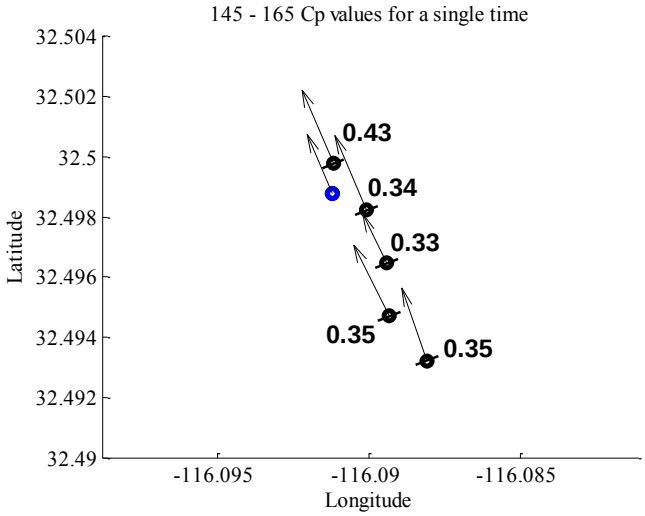

Figure 5.9 Met-mast (blue circle) and wind turbines (black circles) power coefficient for values between 145° and 165° for a single time which reduces the power over AEG-3.

The matching wind speed and power coefficient for each wind turbine for a single time between 145° and 165° which reduces the power over AEG-3 are presented in Table 5.6, additionally the manufacturer's power and thrust coefficients are presented for the wind speed per turbine.

Table 5.6 Wind turbines speed, Manufacturer C_p and Operation C_p between 145° and 165° for a single time which reduces the power over AEG-3.

Wind Turbine	Speed (m/s)	Operation C_P	$C_{P(u)}$	$C_{T(u)}$
AEG-1	6.29	0.43	0.431	0.812
AEG-2	6.31	0.34	0.432	0.812
AEG-3	4.30	0.33	0.360	0.812
AEG-4	6.22	0.35	0.430	0.812
AEG-5	6.01	0.35	0.427	0.812

5.5.2.1 Single values over wind speed operative range

Similar to Subsection 5.6.1.2, a single time step from those identified with a met-mast angle between 145° and 165° and turbines at operating wind speeds was selected. However, this time step shows a wind speed value at AEG-3 which almost causes the turbine to shut down. Wind turbines angles range from 153.30° to 161.08° with speeds from 3.13 m/s to 5.91 m/s and power values from 11.73 kW to 229.85 kW, with corresponding power coefficient values of 0.11 and 0.37 (Table 5.7).

Table 5.7 Met-mast and wind turbines angle, speed, power and C_p values between 145° and 165° for a single time which reduces drastically the power over AEG-3.

Source	Long	Lat	θ_{AEG}	U	u	v	Power	C_p
Met-mast	-116.091	32.498	158.00	4.83	-1.81	4.47		
AEG-1	-116.091	32.499	153.48	5.57	-2.49	4.98	229.85	0.37
AEG-2	-116.090	32.498	156.81	5.91	-2.32	5.43	205.57	0.28
AEG-3	-116.089	32.496	153.55	3.13	-1.39	2.80	11.73	0.11
AEG-4	-116.089	32.494	153.30	5.67	-2.54	5.06	178.04	0.27
AEG-5	-116.088	32.493	161.08	4.51	-1.46	4.27	115.18	0.35

From the u and v wind speed components the quivers for each one of the five wind turbines and the met-mast are calculated. Figure 5.10 shows these vectors and compares the wind speed and power from each wind turbine. AEG-5 and AEG-4 have wind speeds of 4.51 m/s and 5.67 m/s and wind powers of 115.17 kW and 178.04 kW. At the location of AEG-3 the wind speed reduces to 3.13 m/s and as a result, the ten minute averaged power goes down to 11.73 kW. The wind speed is recovered at AEG-2 and AEG-1, where it reaches 5.91 m/s and 5.57 m/s, providing 205.56 kW and 229.84 kW, respectively.

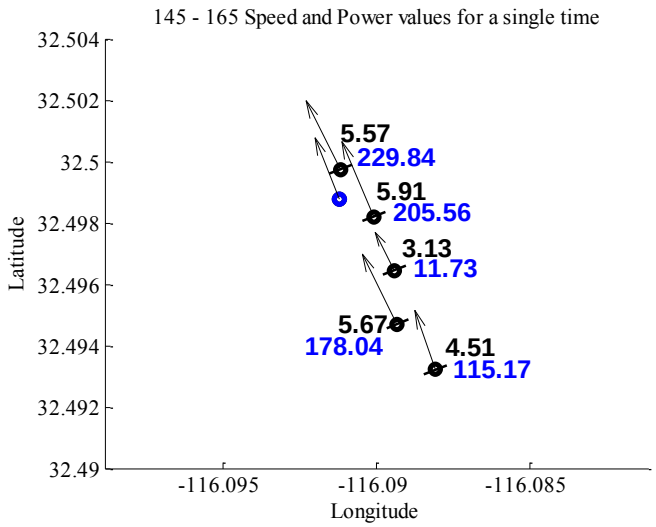

Figure 5.10 Met-mast (blue circle) and wind turbines (black circles) quiver, wind speed (black number) and power (blue number) for values between 145° and 165° for a single time which reduces drastically the power over AEG-3.

Finally, the power coefficients are calculated for each wind turbine for wind speeds and power output values. AEG-5 upwind of the rest of the turbines has a value of 0.35. The next turbine in line, AEG-4, reaches a power coefficient of 0.27. Due to the reduction of wind speed and hence power, AEG-3 has a power coefficient of only 0.11. For the last two wind turbines AEG-2 and AEG-1, the power coefficients increase respectively to 0.28 and 0.37 (Fig. 5.11).

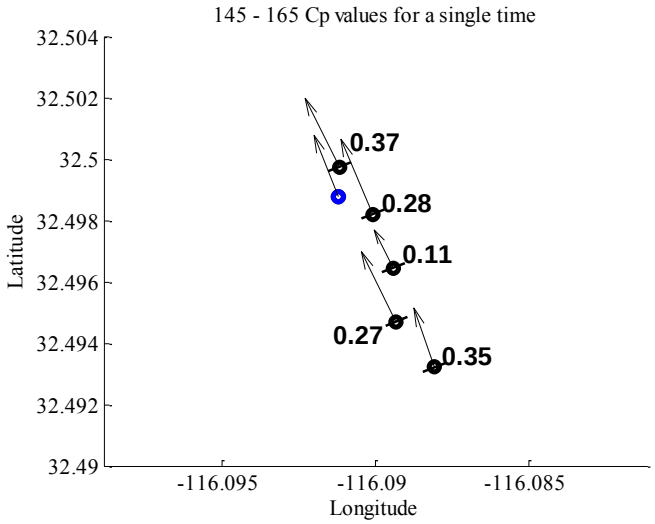

Figure 5.11 Met-mast (blue circle) and wind turbines (black circles power coefficient for values between 145° and 165° for a single time which reduces drastically the power over AEG-3.

The wind speed values for the time step when the wind blows between 145° and 165° and the power over AEG-3 reduces drastically are presented in Table 5.8. For each wind turbine electrical power, the operation power coefficient is calculated, in addition the manufacturer's power and thrust coefficients are presented for the corresponding wind speed.

Table 5.8 Wind turbines speed, Manufacturer C_p and Operation C_p for averaged values between 145° and 165° for a single time which reduces drastically the power over AEG-3.

Wind Turbine	Speed (m/s)	Operation C_P	$C_{P(u)}$	$C_{T(u)}$
AEG-1	5.57	0.37	0.417	0.812
AEG-2	5.91	0.28	0.425	0.812
AEG-3	3.13	0.11	0.000	0.000
AEG-4	5.67	0.27	0.419	0.812
AEG-5	4.51	0.35	0.374	0.821

5.6 WRF simulations for selected case

The Weather Research and Forecasting (WRF) model version 3.4 is used to reproduce the wind characteristics from the time steps presented in Section 5.5. Wind turbines are represented throughout the Fitch et al. (2012) model, with a

78 m hub height and 87 m diameter. From the 2014 aggregated periods presented in Section 4.5.3, the time periods with the wind blowing from the South-Southeast were identified.

5.6.1 WRF model configuration

A single domain was configured, with a 78 by 78 horizontal mesh size, 400 m resolution and 45 vertical layers, from which twelve were located within the lowest 200 m. A single domain was defined, with the centre corresponding at the coordinates of the AEG-3, Latitude 32.496° and Longitude -116.089°. The North American Regional Reanalysis (NARR) dataset was applied, using 12 hours as spin-up period. The parameterization models used were the Mellor-Yamada Nakanishi and Niino (MYNN) Level 2.5 PBL model, the Rapid Update Cycle (RUC) Land Surface Model and the revised MM5 surface layer scheme. Two sets of simulations were performed, from which one was to represent the atmospheric flow, whereas the second represented the effect of the five wind turbines form the La Rumorosa I wind farm, the difference between them represents the wind speed deficit and the wake from the turbines (Figs. 5.12–5.14).

From the results obtained, two time steps are presented in the following subsections, one from results with similar wind speed values and the other with higher wind speed values but corresponding wind directions. For both time steps, the wind speed magnitude and components are presented with the angle of the wind direction and the corresponding power and power coefficient from the manufacturer's data.

5.6.2 WRF Predictions

WRF results with similar wind speed values for the averaged data presented in Section 5.5.1 are presented in Table 5.9. The wind speed direction ranges from

171.62° to 173.85°, and the wind speed decreases from 6.16 m/s to 5.65 m/s from AEG-5 to AEG-1, respectively. The electrical power from each turbine has been calculated for the corresponding wind speed and the manufacturer's power curve, ranging from 365.27 kW to 280.81 kW, from which the power coefficient goes from 0.429 to 0.426 from the turbines AEG-5 to AEG-1.

Table 5.9 Met-mast and wind turbines angle, speed, power and C_p values between 145° and 165° for a single time with similar wind speed values.

Source	Long	Lat	θ_{AEG}	U	u	v	Power	C_P
AEG-1	-116.091	32.499	173.85	5.65	-0.60	5.62	280.81	0.426
AEG-2	-116.090	32.498	172.73	5.70	-0.72	5.65	283.74	0.420
AEG-3	-116.089	32.496	172.18	5.86	-0.93	6.80	310.45	0.424
AEG-4	-116.089	32.494	172.23	6.01	-0.81	5.95	337.46	0.427
AEG-5	-116.088	32.493	171.62	6.16	-0.90	6.09	365.27	0.429

The wind flow is oriented to the North, so the wind turbines are not directly one behind the other (Fig. 5.12). However, the wind speed values were close to the averaged values from Figure 5.6, from which a deficit of 8.28% for the wind speed and 23.12% for power deficit is shown at turbine AEG-1 compared against turbine AEG-5.

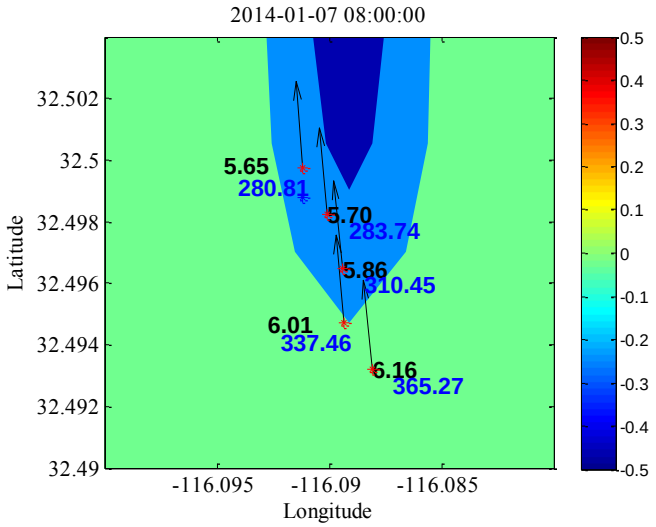

Figure 5.12 Met-mast (blue circle) and wind turbines (black circles) quiver, wind speed (black number) and power (blue number) for a WRF simulation single time with similar wind speed values.

From the WRF results, the wind speed is interpolated at hub height for each wind turbine, and from the manufacturer's power curve, the corresponding power is calculated. From both of these values, the power coefficient is calculated at each wind turbine, which decreases from 0.429 to 0.426 from the upwind turbine (AEG-5) to the downwind turbine (AEG-1) (Fig. 5.13).

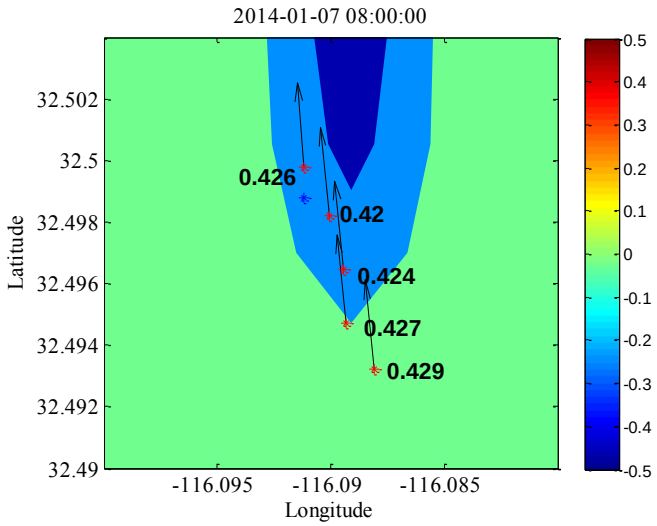

Figure 5.13 Met-mast (blue circle) and wind turbines (black circles) power coefficient for a WRF simulation single time with similar wind speed values.

The mean wind speed value from the wind turbines on subsection 5.5.2 is 5.82 m/s, whereas for the WRF results is 5.87 m/s, over predicting it in a 0.86% the mean wind speed value. The thrust coefficient has been interpolated form the manufacturer's data, to calculate the net drag from the operating data and the WRF simulation. Results are 511.4 kN and 510.9 kN, respectively. The WRF model provides a reasonable prediction of the net thrust force across the all five turbines.

5.6.3 Results with similar wind speed direction

From the WRF results, the wind speed values from a time step with a similar wind direction but higher wind speed magnitude compared against the

averaged data presented in Section 5.5.1 are shown in Table 5.10. The wind speed direction varies along AEG-5 to AEG-1, respectively, from 141.26° to 142.54°, for which the wind speed decreases from 8.47 m/s to 7.81 m/s. After calculating the power at each wind turbine location, these values go from 986.77 kW to 775.15 kW. From the wind speed and power values, the power coefficients were calculated for each wind turbine, which is a constant value of 0.446 for all wind turbines.

Table 5.10 Met-mast and wind turbines angle, speed, power and C_p values between 145° and 165° for a single time with similar wind speed direction.

Source	Long	Lat	θ_{AEG}	U	u	v	Power	C_P
AEG-1	-116.091	32.499	142.54	7.81	-4.75	6.20	775.15	0.446
AEG-2	-116.090	32.498	142.17	7.86	-4.82	6.21	788.40	0.446
AEG-3	-116.089	32.496	141.67	7.99	-4.96	6.27	828.78	0.446
AEG-4	-116.089	32.494	141.14	8.21	-5.15	6.39	900.47	0.446
AEG-5	-116.088	32.493	141.26	8.47	-5.30	6.61	986.77	0.446

For this WRF time step, the wind field shows a direction heading from the Southeast. For this direction, AEG-4 is directly downstream AEG-5, and AEG-1 downstream AEG-2 (Fig. 5.14). Wind speed values are higher than those presented in Figure 5.12. AEG-4 shows a speed and power deficit to AEG-5 of 3.07% and 8.75%, respectively. Whereas, for the AEG-1, the deficit compared against the AEG-2 is 0.64% and 1.68% for the wind speed and turbine power, respectively. Finally, comparing AEG-1 to AEG-5, the wind speed and power deficit are 8.40% and 26.84%, respectively.

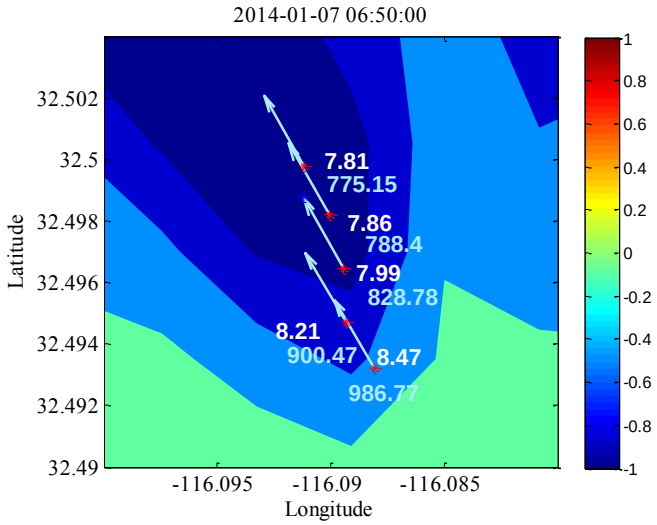

Figure 5.14 Met-mast (blue circle) and wind turbines (black circles) quiver, wind speed (black number) and power (blue number) for a WRF simulation single time with similar wind direction values.

The power coefficient is calculated for each wind turbine, based on the WRF wind speed results and the corresponding power from the manufacturer's curve. For all the velocities from AEG-1 to AEG-5, the power coefficient value is the same 0.446 (Fig. 5.15).

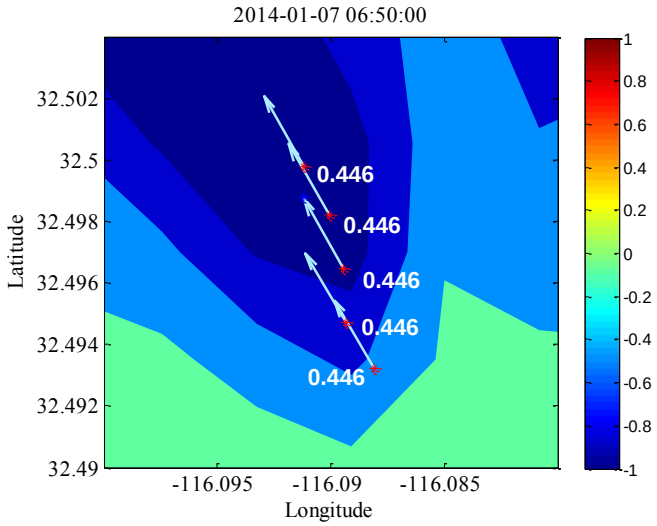

Figure 5.15 Met-mast (blue circle) and wind turbines (black circles) power coefficient for a WRF simulation single time with similar wind direction values.

5.7 Conclusions

In this Chapter, approaches for representing effect of wind turbines on the resource using WRF have been reviewed, data from the La Rumorosa wind farm analysed to quantify influence of turbine interactions on wind speed and power output and the measured changes compared to predictions using the existing wind turbine parameterisation of Fitch et al. (2012).

For the full-scale turbine data analysis an offset angle was applied to the wind heading reported at each wind turbine to account for differing reference angles of each sensor. Samples from a wind direction from the met-mast aligned to the wind farm layout (i.e. 145° to 165° and 325° to 345°) were identified and filtered to identify the number of samples when wind heading at the met-mast and the upwind turbine, lie within this range of angles and the wind speed is above cut-in speed. From the 145° to 165° range 45 samples were calculated, from which only 22 showed the five wind turbines in the operative range, whereas for the range from 325° to 345°, only 4 samples were found, although none of them had all five wind turbines producing wind energy, and this range of directions were discarded.

From the 22 samples within the 145° to 165° range, wind speed and direction, power and power coefficient have been averaged to identify the wake effect from turbine AEG-5, which is upwind of turbines AEG-4 to AEG-1 when the wind is from this direction. Additionally, two ten-minute averaged time steps have been identified, one when the wind speed at AEG-3 is reduced to a value within the operative range, and the other, when the speed at AEG-3 is reduced to a value out of the operative range.

Finally, WRF simulations have been performed applying the wind turbine parameterization model (Fitch et al., 2012) over a period identified with similar wind direction as the cases aforementioned. Particularly two time steps have been outlined, one with similar wind speed values but wind directions with 20°

to the North and a time step with the wind direction within the range, but wind speed values 2.5 m/s higher. Uniform wind speed deficits have been identified along the wind farm from the WRF simulations, whereas from the operating wind farm the wind speed deficits were not uniform, in fact, AEG-3, which is in the centre of the wind farm was the most affected turbine.

In general, the Fitch et al. (2012) model describes the mean of the wind speed from the wind turbines with an error of -0.86%. The overall power from the turbines calculated from WRF is underpredicted by around 16%, however, the net drag force is predicted within 0.10%. The RMSE values for the wind speed, power and drag force based on the five wind turbines for a single time step with similar wind speed values but different wind direction are 0.81 m/s, 116 kW and 25 kN, respectively.

Chapter 6 Multiple Wind Farm Effects

This chapter evaluates the influence of energy extraction by wind farms on the performance of other farms located in close geographical proximity. The energy yield of the 10 MW "La Rumorosa I" wind farm studied in preceding chapters is analysed accounting for the presence of up to four wind farms that are each within a distance of 25 km and with aggregate installed capacity of up to 174 MW. The time interval used for this analysis is selected on the basis of the frequency of occurrence of wind speeds that are from the same heading as the geographical centre of a wind farm, La Zacatosa, located 10.6 km upwind of the case study farm.

The accuracy of the WRF model for simulating the wind resource and energy yield has been evaluated in Chapter 4 for an existing wind farm in Baja California. In the following, the boundary layer model that provided best agreement with the 2014 data for wind speed and energy yield has been applied to assess the effect of future wind farms on the expected energy yield of the existing farm.

A brief review of the approaches available for modelling the effect of wind turbines on the wind resource is given in Section 6.1. The scheme of Fitch et al. (2012) is selected for the present case study. Background to use of this scheme for prediction of wind farm energy supply and wakes is presented in Section 6.2. The location of the potential sites for wind farm developments within the area of La Rumorosa, Mexico is described in Section 6.3. Wind farm deployment scenarios are presented in Section 6.4. The methodology to calculate turbine power output and wind farm energy yield from WRF model predictions of wind speed are presented in Section 6.5. The wind resource assessment based on meteorological simulations for La Zacatosa wind farm is described in Section 6.6, covering the wind resource, effect of wind turbine wakes on performance of turbines within that farm and the downwind effect at the La Rumorosa I wind

farm. Similar analysis is presented in Section 6.7 considering four wind farms within the La Rumorosa area. Energy yield is determined based on simulations of resource only and accounting for wake effects and the effect of these farms on both power output and energy yield of the La Rumorosa I wind farm is assessed.

6.1 Methods for Representing Wind Turbines and Farms in WRF

An approach for representing wind farms in the WRF model was formulated and applied by Singer et al. (2010). They represented a single turbine and an array of turbines, which were perpendicular to the flow. The deceleration of the flow passing through each rotor area was prescribed. Empirical parameters such as the amplitude of deceleration and the distance along the wake were defined and applied. The approach was demonstrated for an array of four by four wind turbines located on flat terrain. This confirmed that a sudden drop of the velocity occurs at the turbines and at downstream locations. This scheme is based on measurements of the wake of full-scale turbines. Comparison of velocity and turbine performance within an array with a real wind farm project indicates velocity reduction of 2.6 m/s and that the wake extends to more than 550 m downwind for an input of 10 m/s. This wake was in qualitative agreement with measured data but no quantitative comparison was presented. It was found that the wake is sensitive to the following empirical model parameters: the rate of deceleration at the turbine, the perpendicular distance over which the deceleration is applied relative to the position of each turbine and the assumed distribution of deceleration over this distance as a function of the distance from the rotor. These parameters are required to be set based on the operational data from a wind farm.

Blahak et al. (2010) developed an actuator disc wind turbine model for WRF by defining a reduction of kinetic energy as a function of the turbine power output. The power coefficient from the wind turbine defines the reduction of the kinetic energy over the vertical levels that intersect the rotor swept area. Additionally, wind shear is induced based on the power coefficient and the mechanical and electrical efficiency of the wind turbine. An additional kinetic energy conversion factor between the grid and subgrid scales, was defined from the power output and efficiency of the turbine. To evaluate this approach, 225 idealised wind turbines were set over an area of 10 km by 10 km, with a 1 km resolution. Each wind turbine was defined by a capacity of 5 MW with a power coefficient of 0.48, a conversion efficiency of 0.9, hub height of 102 m and rotor diameter of 236 m. A wind speed of 9 m/s was considered. For this arrangement the wake from the farm extended to 250 m height relative to the ground, within 3 km of the farm and persists to more than 20 km downwind. The wind speed reduction within the wind farm was from 20% to 25% (3 m/s) of the onset wind speed, while at 21 km downstream, this reduction was between 6.7% and 8.3%, these results have not been compared to an operating wind farm.

Fitch et al. (2012) modified the approach of Blahak et al. (2010) defining the momentum sink and turbulent kinetic energy addition based on a turbine-specific variation of both electrical power output and thrust coefficient with wind speed. The momentum sink was defined by the wind turbine thrust coefficient. The turbulent kinetic energy (TKE) source was defined by the difference between extracted energy, defined by thrust coefficient, and electrical power output and so also varies with onset flow speed. With this approach, it is assumed that the TKE source represents the stirring of the ambient flow by the turbines, but not the mixing which results from the vertical wind shear induced by the momentum sink. This scheme was tested for a 10 by 10 array of wind turbines, each with rated capacity of 3 MW. A wind speed deficit of 10 % reduction was observed, compared against 8% - 9% obtained from

measurements of similar size offshore wind farms (Christiansen and Hasager, 2005). This provides confidence in the approach for accurately predicting the flow-field downwind of a wind farm. A limitation is that the horizontal cell size should be greater than five rotor diameters. By comparing the size for the far-wake region from this study against Christiansen and Hasager (2005), the conclusion is that the drag-disk model performs appropriately.

Volker et al. (2012) presented further development of the Fitch et al. (2012) scheme to account for the influence of upwind turbines within a group on downwind turbine performance. The model was configured with mesh of 60 by 50 cells, with a 1,400 m horizontal resolution and 60 vertical layers. The wind farm was located within 5 by 4 grid-cells, with 4 turbines per cell. This was based on the far wake theory (Tennekes and Lumley, 1972); this theory considers that the characterization of the wind speed deficit region is based on a characteristic length scale and on the maximum velocity deficit, which are determined from measurements. From this formulation, a lower value of momentum sink is obtained per cell compared to the approach of Fitch et al. (2012) since the inter-turbine interaction within the farm is modelled. The Horns Rev and Nysted offshore wind farms were analysed and the results were compared against data from three met-masts, eighteen wind turbines (rows 4 and 5 from Horns Rev) and from a satellite, to evaluate the wake velocity and its extent downwind of the farm. Their model provided closer prediction of the observed data than the Fitch et al. (2012) model, the latter presented an overestimation of the energy extraction, while the approach proposed followed the measured thrust and results are compared qualitatively per met-mast and wind turbine. Discrepancy is due to the Fitch model over estimating the momentum sink and predicting higher near-ground velocities due to the input of TKE at all levels occupied by the turbine. Although a promising approach

the Volker et al. (2012) parameterization scheme is not yet implemented within the open-source WRF model.

6.2 Studies of inter-farm effects

The effect of an operating wind farm on another wind farm within relatively close geographic proximity has received limited attention in the literature, mostly addressing offshore farms rather than onshore farms.

In terms of wind resource analysis, Byrkjedal et al. (2014) employed the Fitch et al. (2012) wind turbine parameterization to perform a WRF study with three nested domains, with a resolution up to 1 km. The 68 wind turbine Smøla wind farm was analysed from June 2007 to July 2008. Analysis was performed over a sector with a wind direction from 22.5° to 47.5°. From these angles, intervals with wind speed values from 5 to 15 m/s were selected. Mean wind speed values for atmospheric stable conditions presented mean wind speed values of 7.3 m/s, which showed wind speed deficits of 0.3 m/s at a range of distances from 20 to 25 km downstream the wind farm. Whereas for the atmospheric unstable conditions, mean wind speed value was of 7.0 m/s and the deficit was smaller than 0.3 m/s from 10 to 15 km away from the farm. Results were validated from a met-mast located 167 m southwest to the farm and from each met-mast from the wind turbines. The power produced from the wind farm was underestimated in a 7.3% for the period analysed, while the wake velocity were underpredicted by 2.6% compared to the observations.

On the same year, Hidalgo et al. (2014) simulated the interaction of 17 different wind farms on the Southeast of Spain over 2011. Results showed a lower mean wind speed (i.e. a higher deficit) at those farms close to other wind farms. The

difference on the wind speed values from wind resource and wind farm simulations reached up to 1 m/s. Wakes extended up to 25 km downwind of each farm, with a greater extent from the largest wind farms.

Jiménez et al. (2015) calculated the power deficit and the wake size downstream of an offshore wind farm throughout the WRF model. Five nested domains were applied with horizontal resolution of 333 m in the most refined level and a ratio 1:3 between levels. All domains considered 36 vertical levels. A configuration of 8 by 10 wind turbines, with 80 m diameter and capacity of 2 MW was defined on the centre of finest level, representing the Horns Rev wind farm. The spacing between turbines was seven diameters from East to West and 10.4 diameters Northwest to Southeast. The energy extraction model of Fitch et al. (2012) was applied considering the wind turbine manufacturer data to estimate the thrust and power coefficients. Hourly data was calculated for the years 2005 to 2007. Results showed effects of the wind farm to greater than 15 km downwind. Additionally, the power generated per each turbine was calculated, ranging from 515 to 405 kW, producing a power deficit up to 21 %.

Eriksson et al. (2015) compared WRF model simulations against Large Eddy Simulations (LES), to describe large scale wind farm wakes and the interaction with another wind farm. Results were compared against operational data from the Lillgrund wind farm, which comprises 48 2.3 MW Siemens wind turbines. SCADA data from five years was analysed to identify periods with an inflow angle of 222°. WRF simulations were performed for those periods identified for a domain without the turbines and with the turbines considering the parameterization model (Fitch et al., 2012). Results for the wind energy yield were more accurate with the LES method. The dimensionless velocity for the WRF model recovered to 0.82 at 2 km and to 0.95 at 6 km behind the farm,

while for the LES model, these values were smaller, recovering to 0.81 and to 0.907 at the same distances, respectively.

From this inter wind farm effects review, two works were performed onshore (Byrkjedal et al., 2014; Hidalgo et al., 2014), while two were performed offshore (Jiménez et al., 2015; Eriksson et al., 2015). From which, the size of wake calculated from WRF reaches more than 20 km downwind, at this distance, the power deficit reaches 7% to 15%. For a 15 km downstream distance, the power deficit can reach 21% (Byrkjedal et al., 2014). Nevertheless, the work from Eriksson et al. (2015) and from Byrkjedal et al. (2014) both agree that the WRF wind turbine parameterization model (Fitch et al., 2012), overpredicts the wind speed deficit at the wind farm, due to the lack of representing the influence of neighbouring wind turbines over the power production. The analysis of this Thesis considers the effect on the wind energy yield at an existing wind farm due to the operation of wind farms at distances in the range 15-25 km located in complex onshore terrain.

6.3 Potential sites for future wind farms

The geographic region considered for this study is the same region of Baja California considered in Chapter 4 (Section 4.4). Within this region, four sites have been identified by the Baja California Energy Commission (State of Baja California, 2011), which are suitable for wind energy developments in terms of proximity to the network, topography, wildlife and archaeological remains (SIGEA, 2006), shown on Figure 6.1. Met-mast data from two points La Rumorosa and La Zacatosa and the operational data from the existing wind farm "La Rumorosa I" are available for the whole year 2014.

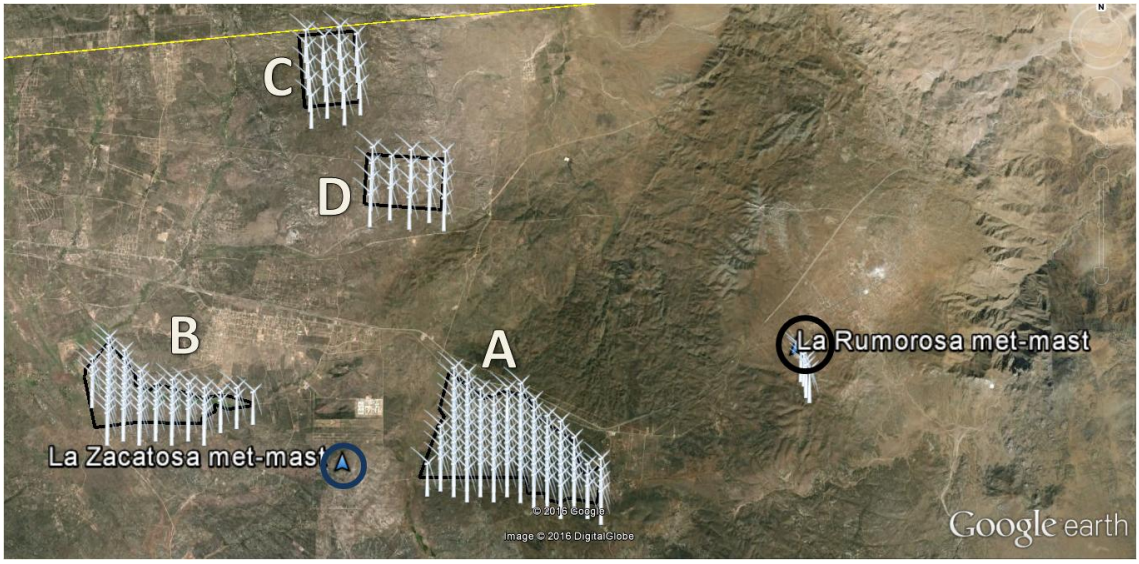

Figure 6.1 La Rumorosa I wind farm at Lat 32°29'47.55" N, Long 116°05'21.01" W and 1,349 mamsl, with met-mast (black circle), La Zacatosa met-mast (blue circle) and future wind energy projects, La Zacatosa (A), Jacomun (B), Canoas (C) and Saucito (D).

Table 6.1 Data about the sites on the area of La Rumorosa.

	Site	Lat	Long	Area (ha)	Min Altitude (mamsl)	Max Altitude (mamsl)	Distance and orientation from La Rumorosa
A	Zacatosa	32.473°	-116.201°	1,537	1,160	1,360	10.6 km WSW
B	Jacomun	32.484°	-116.333°	630	927	1,025	23.6 km W
C	Canoas	32.591°	-116.268°	499	1,040	1,105	19.55 km NW
D	Saucito	32.555°	-116.238°	491	987	1,122	15.07 km NW

Table 6.1 summarizes the location in latitude and longitude coordinates, the area, the highest and lowest elevation points in metres above the mean sea level (mamsl), and their distance and direction away from the existing "La Rumorosa I" wind farm for the four sites depicted in Figure 6.1. From this site, the closest is the Zacatosa, while the farthest is Jacomun, in terms of size Zacatosa is the largest, while Saucito is the smallest. Regarding the topography, Zacatosa presents the highest point, while the site of Jacomun is the lowest. As it has

been mentioned in Chapter 1, there are plans to increase the wind power installed capacity nationwide by 2018 (Reuters, 2015), however, none of the local plans from the state of Baja California were published at the time of writing.

6.4 Wind Farm Deployment Scenarios

WRF simulations considering the effects of wind turbines over the region aforementioned have been performed for different turbine types per farm and for two scenarios. The computational domain with a 400 m resolution is presented in Figure. 6.2 with the boundary of each farm located as Figure 6.1.

Case 1: only the farm directly upwind (La Zacatosa)

Case 2: all four farms

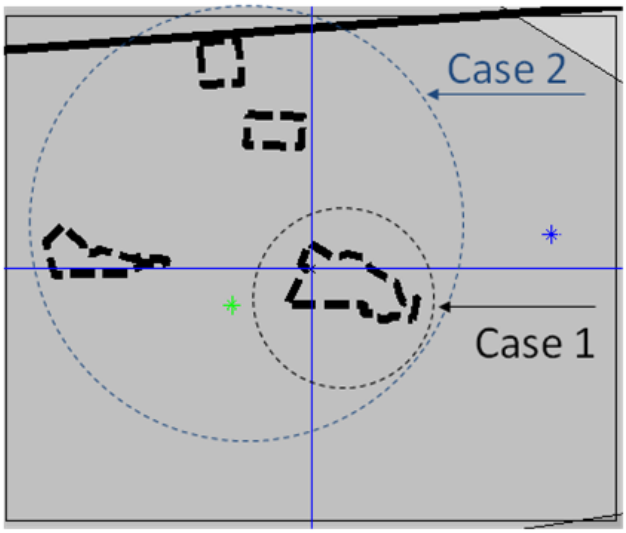

Figure 6.2 Wind Farms distribution for the analysis, blue point on the right defines the location of the La Rumorosa met-mast, the green point left to the centre shows the location of the La Zacatosa met-mast.

For each wind farm development scenario the same wind turbine model is considered for all wind farms. Three alternative wind turbine models are

considered with rated power 2 MW, 3.3 MW and 5 MW and diameter 87 m, 112 m and 128 m, respectively. These turbine types were considered to represent farm development in the near, medium and long term future.

Table 6.2 summarises the scenarios considered, including only one farm and all four, for a wind turbine rated power model of 2 MW, 3.3 MW and 5 MW. The wind turbine models are the following: Gamesa G87 2 MW, with a diameter of 87 m and a hub height of 78 m. A Vestas V112 3.3 MW with a diameter of 105 m and a hub height of 84 m. Finally, the Gamesa G128 5 MW, with a diameter of 128 m and a hub height of from 120 to 140 m.

Table 6.2 Wind Farms and turbine models for the analysis.

Number of Farms	Wind Turbine Capacity	Manufacturer	Wind Turbine Model
1	2 MW	Gamesa	G87 2 MW
4	2 MW	Gamesa	G87 2 MW
1	3.3 MW	Vestas	V112 3.3 MW
4	3.3 MW	Vestas	V112 3.3 MW
1	5 MW	Gamesa	G128 5 MW
4	5 MW	Gamesa	G128 5 MW

6.5 Selection of Wind Farm Installed Capacity and Layout

According to the Department of Energy and Climate Change throughout the Digest of United Kingdom energy statistics (DECC, 2015), from 2009 to 2013 the average capacity factor for wind power plants is of 28.48%, this capacity factor has been set as a target value for the La Zacatosa wind farm layout in order to select a representative installed capacity and inter wind turbine distance. For this aim, four different installed capacities have been selected for La Zacatosa site: 72 MW, 92 MW, 128 MW and 184 MW (Table 6.2). The wind speed has been extracted at hub height (78 m) of the Gamesa G87-2MW wind turbine

(Gamesa, 2007) for both a wind resource only simulation and using the Fitch et al. (2012) wind turbine scheme. This turbine parameterization model was applied at each of the Latitude and Longitude coordinates of each turbine within the four installed capacity scenarios.

Four planned farms are identified that are located 10.6 km to 23 km away from the existing farm, they are expected to have an installed capacity of between 50 – 150 MW each. Based on the annual wind rose distribution from 2014 each of the planned farms are upwind of the existing farm. Energy yield from each farm was modelled based on wind resource only and accounting for the turbine wake effect for the aggregated time intervals from 2014, as summarised in Table 6.2. Turbine type and turbine arrangement were selected for these planned locations such that each farm would operate with a capacity factor similar to that of the case study La Rumorosa farm (28.48%, see Section 6.5).

Wind farm energy yield, and hence farm capacity factor, was calculated from the hub height time series wind speed at the location of each wind turbine and the manufacturer's power curve (Gamesa, 2007). The hub height wind speed, energy yield, and hence capacity factors were calculated by two methods:

- Yield neglecting turbine interaction: considering only the wind resource and neglecting the interactions between the wind turbines. From which WRF simulations were configured with a single domain of 78 by 78 cells with a horizontal resolution of 400 m, 45 vertical levels were defined, from which twelve levels were set in the lowest 200 m. The centre of the domain coordinates were Latitude 32.4987° and Longitude -116.0912°. As defined on Section 4.3.2.2, simulations were performed over four

aggregated periods which represented the annual wind speed and direction distribution. The dataset selected for the initial and boundary conditions was the North American Regional Reanalysis (NARR) and the WRF configuration model was the 5-3-1 (NARR 5-3-1), as defined in Section 4.4.3 with a 12 hour spin up period.

- Yield considering turbine interaction: the wind turbine parameterization was applied, to evaluate the change on the capacity factor for each installed capacity. For this case, the WRF simulations were configured exactly the same as above, however, the location of the wind turbines (latitude and longitude) and their corresponding operational data (hub height, diameter, standing thrust coefficient, nominal power, cut-in and cut-out speeds), to activate the wind turbine parameterization scheme (Fitch et al., 2012).

The wind energy yield for each wind farm is calculated from equation (6.1)

$$E_F = \sum_{t=1}^{N_t} \sum_{i=1}^{N} P_i\big(U(t)\big)dt \qquad (6.1)$$

where E_F is the energy of the farm in kWh, t is the time step, N_t is the total number of time steps at increments dt = 10/60 for data sampled at ten minutes, i denotes a turbine within the farm comprising a total of N turbines, and $P_i(U(t))$ is the corresponding power in kW from the wind turbines manufacturers power curve to hub-height wind speed u in m/s. For the case of the wake effect simulations, the energy from the wake effect (E_W) in kWh will be calculated by equation (6.1) with the same power curve, number and location of turbines, however, the wind speed from the resource only simulations is replaced by the wind speed from the simulation with wake effect modelled, denoted U_w. The capacity factor for the wind resource assessment farms is calculated as:

$$CF_F = \frac{E_F}{N\ P_R N_t\ dt} \tag{6.2}$$

where CF_F is the capacity factor for the wind farm based on the resource only simulations in kWh, E_F is the energy yield from the farm, N is the total number of turbines, N_t is the total number of ten-minutes time steps, P_R is the rated power of the wind turbine in kW. The capacity factor from the wind farms addressing the wake effects (CF_W) is also calculated with equation (6.2), however, the wind energy yield (E_W) is the one calculated with the wind speed interpolated from the wake effect simulations.

The same methodology for wind energy yield (equation 6.1) and capacity factor analysis (equation 6.2) is employed for all the four wind farms. Table 6.3 presents the energy yield and their wind turbine spacing in diameters (D) for the installed capacity scenarios from 72 to 184 MW. From this set, the farm with the highest capacity factor (28.78%), closest to mean value published by the DECC (2015) and to the capacity factor of La Rumorosa, was found with the 72 MW capacity farm.

Table 6.3 Capacity factor per installed capacity at La Zacatosa site with and without the wind turbine model considered.

Installed Capacity (MW)	E-W distance	N-S distance	Wind Resource Energy Yield (GWh)	Capacity Factor (%)	Wake Effect Energy Yield (GWh)	Capacity Factor (%)
72	8.9 D	6.9 D	15.628	32.30%	13.922	28.78%
92	7.9 D	7.3 D	19.591	31.69%	17.105	27.67%
128	7.4 D	5.6 D	27.559	32.04%	23.201	26.97%
184	5.4 D	4.3 D	39.846	32.23%	31.485	25.46%

The wind turbine spacing from the La Zacatosa 72 MW (Table 6.3) wind farm was applied to the other three farms (Jacomun, Canoas and Saucito) to identify the number and installed capacity of 2 MW turbines that would fit on each farm. The same installed capacity values from each farm, based on the 2MW rated power model, was kept constant or the closest value to the other wind turbine rated power models (3.3 MW and 5 MW). Table 6.4 shows the number of turbines, and the corresponding capacity factor for each farm for each of the three turbines considered.

Table 6.4 Number of turbines and total capacity per site by turbine capacity.

Name of Site	2 MW		3.3 MW		5 MW	
	Number of Turbines	Total Capacity	Number of Turbines	Total Capacity	Number of Turbines	Total Capacity
Zacatosa	36	72 MW	22	72.6 MW	14	70 MW
Jacomun	23	46 MW	14	46.2 MW	9	45 MW
Canoas	14	28 MW	9	29.7 MW	6	30 MW
Saucito	14	28 MW	9	29.7 MW	6	30 MW

The spacing between turbines used for the La Zacatosa wind farm was also used for the other three pieces of land in order to keep an installed capacity close to 72 MW for each wind turbine model (Table 6.5).

Table 6.5 Spacing between wind turbines for all sites by turbine capacity.

Turbine Capacity	2 MW		3.3 MW		5 MW	
Direction	E-W distance	N-S distance	E-W distance	N-S distance	E-W distance	N-S distance
Spacing	8.9 D	6.9 D	15.4 D	6.5 D	11.5 D	8.9 D

Finally, wind energy yield is calculated at the La Rumorosa I wind farm from equation (6.1) and the deficit of the wind energy yield is calculated as:

$$dE_{LR} = \frac{E_W - E_F}{E_F} \times 100 \qquad 6.3$$

where dE_{LR} is the percentage wind energy deficit at La Rumorosa I wind farm, E_W is the wind energy yield calculated at the La Rumorosa I wind farm accounting for the wake effect from close proximity farms and E_F is the wind energy yield calculated at the La Rumorosa I wind farm considering only the wind resource.

To graphically describe the wind speed difference from wind resource simulations and the wake effect of the wind turbines over the wind speed field, the wind speed difference ($\Delta u_{i,j,k,t}$) will be calculated by:

$$\Delta u_{i,j.k,t} = u_{w\ i,j.k,t} - u_{r\ i,j.k,t} \qquad 6.4$$

where Δu is wind speed deficit in m/s, u_w is the wind speed from the simulations considering the wake effects, u_r is the wind speed for the wind resource only, i is the longitude, j is the latitude, k is the elevation and t is the time.

6.6 Case 1: La Zacatosa Wind Farm only

The wind resource has been evaluated throughout the WRF model for the area of La Rumorosa (Chapter 4.3). In this Section the wind power density (W / m^2) over the plan area of La Zacatosa site is evaluated. The wind energy yield and capacity factor, for each of the installed capacities on this site, described in Table 6.4 are calculated. A farm arrangement is then selected and the influence of this deployment at La Zacatosa on the power output and energy production of the La Rumorosa I wind farm is assessed.

6.6.1 Energy yield from turbines at La Zacatosa: resource only

Wind resource simulations have been performed for the four week aggregated period of 2014 that is described in Section 4.3.2.2 and based on the La Zacatosa met-mast annual distribution of occurrence of wind rose. Wind speed profiles have been extracted at three different heights: 78 m, 84 m and 120 m heights, which are applied to the wind turbine power curve for capacities of 2 MW, 3.3 MW and 5 MW, respectively, described in section 6.4. Based on the wind farm layouts and installed capacities from Table 6.4, the wind energy yield was calculated from the wind resource simulation from equation (6.1).

The La Zacatosa wind farm for the 2 MW wind turbine case and an installed capacity of 72 MW, projected 15.628 GWh over the aggregated period and a capacity factor of 32.30% (see Table 6.3, Fig. 6.3 and Table 6.6). Mean wind speed for the aggregated period at a hub height of 78 m varies from 5 m/s up to 7.5 m/s; additionally, the capacity factor (equation 6.2) per turbine ranges from 20% to 40% depending on position within the wind farm. Zones with highest mean wind speed and capacity factors are located on the Northwest of the farm (Fig. 6.3).

For Cases 3 and 5, the wind speed values were extracted at 84 m and 120 m height and were interpolated at the locations of the 3.3 MW and 5 MW wind turbines, respectively. Considering the manufacturers power curve, the power was calculated at each wind turbine based on the wind speed at hub height from equation (6.1). The capacity factor for both of the wind farm layouts was calculated from equation (6.2). Wind energy yield values over the aggregated period are presented in Table 6.6 for the three cases of wind energy yield assessment at the La Zacatosa wind farm based on the wind resource assessment without considering the wake effect within the farm.

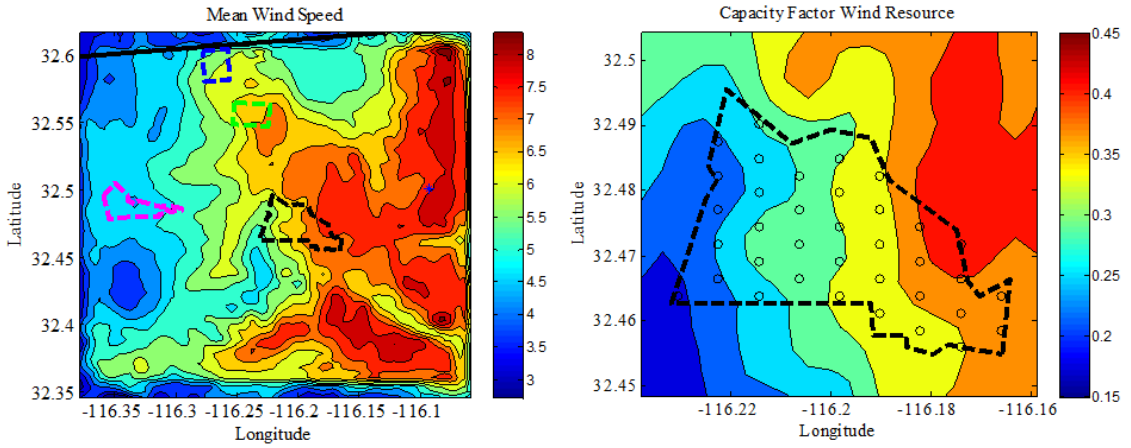

Figure 6.3 Wind speed in m/s over the domain (left) and capacity factors over the La Zacatosa wind farm (right) form the resource assessment the circles denote the location of a wind turbine.

6.6.2 Energy yield from turbines at La Zacatosa: with wake effect

The same sets of simulations have been conducted locating the wind turbines in the same position as aforementioned; however, in this case, the Fitch et al. (2012) scheme was employed to simulate the influence of the wind farm performance on the wind resource (Figure. 6.4).

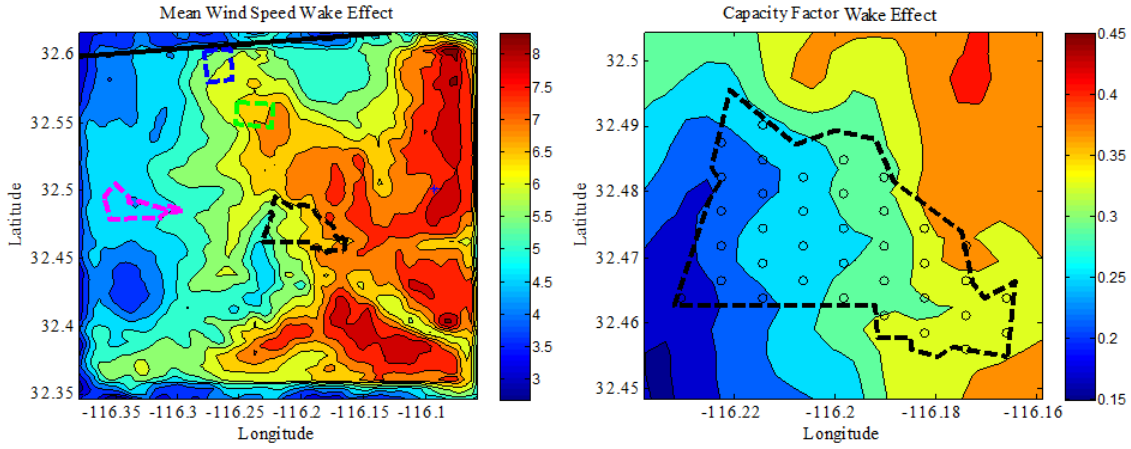

Figure 6.4 Wind speed in m/s over the domain (left) and capacity factors over the La Zacatosa wind farm (right) form the wake effect the circles denote the location of a wind turbine.

The mean wind speed at hub height over the La Zacatosa site was reduced from 5 m/s to 4.5 m/s for the low mean wind speed, while it diminished from 7.5 m/s to 7 m/s for the high wind speed, and the capacity factor (equation 6.2) for turbines within the farm varied from 10% to 37%. Wind energy yield (equation 6.1) was reduced to 13.922 GWh, corresponding to a capacity factor of 28.78% (Fig. 6.4 and Table 6.6).

Table 6.6 describes the wind energy yield from the La Zacatosa wind farm. For the 2 MW wind turbine case and an installed capacity of 72 MW (Table 6.4), from resource only simulation 15.6 GWh were calculated (equation 6.1). However, by applying the wind turbine momentum sink parameterization (wake effect) 13.9 GWh (equation 6.1) was forecasted. This reduction on the wind energy yield is due to the effect from the wind turbines parameterization model over the wind speed flow.

The three wind turbine models (2 MW, 3.3 MW and 5 MW) have been deployed over the La Zacatosa wind farm. From this the capacity factors (equation 6.2) during the interval of four aggregated weeks (Section 4.3.2.2) are calculated, based on the resource only and wake effects simulations. Being 32.30% and 28.78% respectively, for the 2 MW wind turbine model (Table 6.6). The 3.52% decrease is associated with the wake effect from each turbine on the downwind turbines. For the 3.3 MW turbines, these values are 35.95% and 30.42% (Table 6.6), for which difference is 5.53%. This is larger than for the 2 MW turbine model, because the 3.3 MW model has a larger diameter and affects the resource over a larger vertical area. From the 5 MW wind turbines, the capacity factors were 34.53% and 29.14% (Table 6.6), showing a difference of 5.39% from the resource only and the wake effect simulations, which is smaller than obtained from the 3.3 MW model, this is attributed to a larger spacing between

the 5 MW wind turbines within the farm. All of these capacity factors are over 28.48% reported from the DECC (2015) for the United Kingdom, value which is taking as guide to define the feasibility of the wind farms layouts.

Table 6.6 Wind energy yield and capacity factor at La Zacatosa wind farm.

La Zacatosa	2 MW	3.3 MW	5 MW
Resource Only (GWh)	15.62	17.53	16.24
Capacity Factor	32.30%	35.95%	34.53%
Wake Effect (GWh)	13.92	14.84	13.71
Capacity Factor	28.78%	30.42%	29.14%

From this analysis, the configuration for La Zacatosa wind farm provided feasible wind energy yield values for the aggregated subset of 2014, which represents the annual wind resource within 9.2% (Section 4.3.2).

6.6.3 Effect of La Zacatosa wind farm on La Rumorosa wind farm

The influence of the La Zacatosa wind farm on the performance of the La Rumorosa I wind farm is assessed in terms of power production and energy yield. Wind energy deficit (equation 6.3) at la Rumorosa due to the operation of La Zacatosa was calculated for the three wind turbine model layouts (Table 6.4) these deficits are summarised in Table 6.7. Effect on energy yield is considered for the aggregated time interval during 2014 detailed in Section 4.2.2. Effect on power production is evaluated for the wind direction aligned with the bearing from La Zacatosa to La Rumorosa which is 67 degrees (East-Northeast).

To evaluate the impact of the upstream wind farm, the wind speed values were interpolated at exactly the same points at the hub height once the wind turbine parameterization model was addressed (Fitch et al., 2012). Based on equation

6.1, wind energy yield is calculated at La Rumorosa I wind farm from the wind resource simulations by considering the effect over the flow from the three layouts at La Zacatosa wind farm described in Table 6.4.

The three wind turbine models have been deployed over the La Zacatosa wind farm, 2 MW, 3.3 MW and 5 MW. From which the farm capacity factor (equation 6.2) during the four aggregated weeks interval are calculated, based on the resource only and wake effects simulations (Table 6.7). The wind farm with the greater capacity factor is the 72.6 MW installed capacity, with a wind turbine model of 3.3 MW (35.95%). The capacity factors were calculated from the WRF simulations addressing the wake effects from the wind turbines, from which the configuration with the higher capacity factor was the same 72.6 MW wind farm with the 3.3 MW wind turbine model (30.42%)

The installed capacities for the 2 MW, 3.3 MW and 5 MW wind turbines models over the La Zacatosa wind farm are 72 MW, 72.6 MW and 70 MW (Table 6.4). From which the wind energy yield has been calculated downstream at La Rumorosa I wind farm from the wind resource and wake effect simulations. Wind energy yield from the wind resource simulation is 3.130 GWh for the four weeks aggregated period. The wind energy yields at this farm, addressing the effects from the aforementioned potential farms, are respectively: 3.096 GWh, 3.087 GWh and 3.086 GWh, corresponding to deficits of 1.09%, 1.37% and 1.41% (Table 6.7). The larger diameter wind turbines at La Zacatosa wind turbines result in a larger effect on energy yield of La Rumorosa I wind farm.

Table 6.7 Wind energy yield at "La Rumorosa I" wind farm due to the operation of La Zacatosa wind farm.

La Zacatosa	2 MW	3.3 MW	5 MW
Wind Resource	3.130	3.130	3.130
Wake Effect	3.096	3.087	3.086
Deficit	**1.09%**	**1.37%**	**1.41%**

Figure 6.5 shows the deficit of horizontal wind speed (Δu), calculated as the difference of the wind speed at 78 m height from the wake effect simulations (u_w), minus the same field from the resource only simulations (u_r), for the heading directly from the La Zacatosa wind farm to La Rumorosa I wind farm, equation 6.4. Wind speed values at La Zacatosa met-mast reached 5.95 m/s, while the value at La Rumorosa met-mast was of 10.34 m/s for the resource only. After addressing the effects of the 2MW wind turbines over the La Zacatosa farm, the wind speed decreased to 10.03 m/s at La Rumorosa met-mast. The wind speed deficit of 0.31 m/s corresponds to a 3.00% reduction of the wind speed. Converting to electrical power following the power curve from Figure 4.4, the power reduces from 1,633 kW down to 1,538 kW, a power deficit of 5.84% (Table 6.8). Wind speed deficit reached 2.0 m/s over the area of La Rumorosa and a wake is evident at 12 km downwind of La Zacatosa farm, which was calculated by subtracting the wake effect simulations wind field from the wind resource simulations wind field.

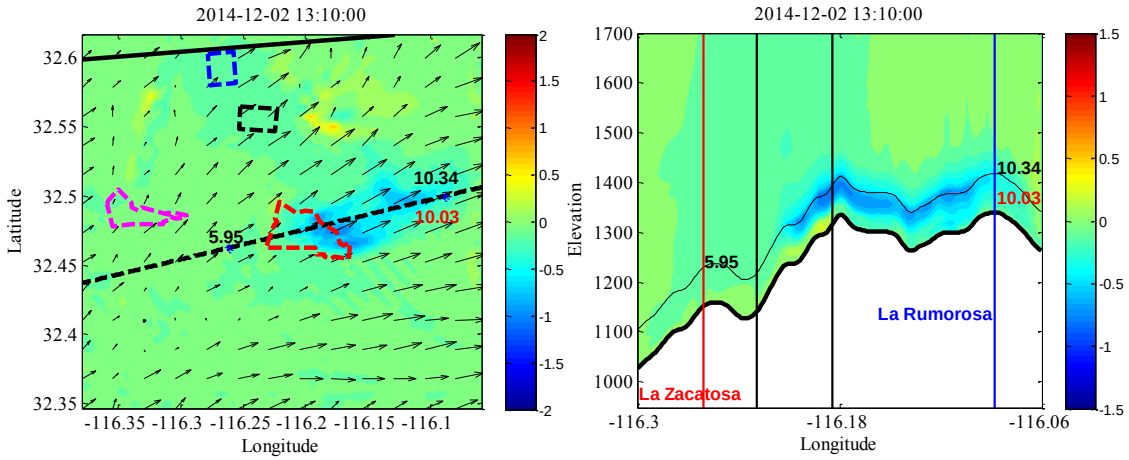

Figure 6.5 Wind speed difference (m/s) at 78 m height for farm of 2 MW wind turbines at La Zacatosa. Horizontal section (left) shows wind farms (dashed regions) and plane (dashed line) of vertical section (right). Wind speed (m/s) shown without (black text) and with (red text) wake effect modelled from wind farm at La Zacatosa (red dashed region, vertical lines).

The 5 MW wind turbines were located within the limits of the La Zacatosa site (see Fig. 6.6). Wind speed deficit was calculated at 78 m height, the hub height of the 2 MW turbines at La Rumorosa. Figure 6.6 illustrates the extent of the wake for this farm, reaching deficit values of 2 m/s over a larger downstream distance and vertical extent than the wake from the farm of 2 MW turbines at La Zacatosa. For a mean wind speed of 9.90 m/s a reduction of 0.44 m/s (4.26%) is observed at the La Rumorosa met-mast. The turbine power output associated with this wind speed is 1,495 kW, which corresponds to an 8.48% power deficit compared against the wind resource only simulations (Table 6.8). Operation of 70 MW of 5 MW at La Zacatosa thus causes a 3% greater reduction of power output at La Rumorosa than operation of 72 MW of 2 MW turbines at La Zacatosa. The vertical section is presented on Figure 6.6 (right), which shows higher wind speed deficits within the area of the farm and downwind.

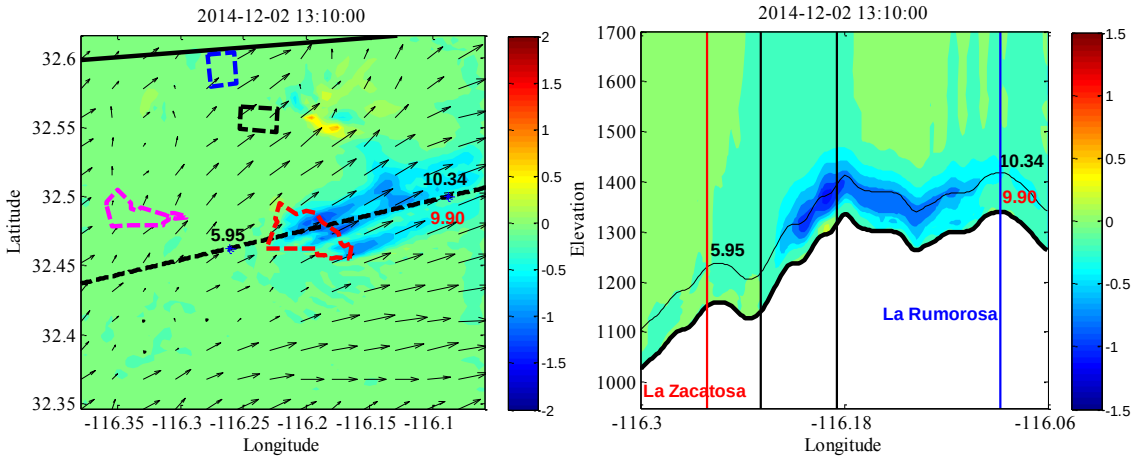

Figure 6.6 Wind speed difference (m/s) at 78 m height for farm of 5 MW wind turbines at La Zacatosa. Horizontal section (left) shows wind farms (dashed regions) and plane (dashed line) of vertical section (right). Wind speed (m/s) shown without (black text) and with (red text) wake effect modelled from wind farm at La Zacatosa (red dashed region, vertical lines).

Wind speed and power has been calculated at the La Rumorosa wind farm for a single turbine based on the Gamesa G87 2 MW power curve and height. The speed and power deficit is calculated from the wind resource and wake effect simulations considering only the La Zacatosa wind farm. Speed deficits increase as the turbine power, and hence diameter, increases, ranging from 3.00% up to 4.26%. As the kinetic energy flux changes in the cube of the wind speed, deficits of power are greater, ranging from 5.84% to 8.48% (Table 6.8).

Table 6.8 Wind speed and power at "La Rumorosa I" wind farm due to the La Zacatosa wind farm operation for a single time step with wind direction of 75°.

La Zacatosa	2 MW		3.3 MW		5 MW	
	Speed (m/s)	**Power (kW)**	**Speed (m/s)**	**Power (kW)**	**Speed (m/s)**	**Power (kW)**
Wind Resource	10.34	1,633	10.34	1,633	10.34	1,633
Wake Effect	10.03	1,538	10.00	1,528	9.90	1,495
Deficit	**3.00%**	**5.84%**	**3.29%**	**6.43%**	**4.26%**	**8.48%**

In this section, wind turbines from 2 MW, 3.3 MW and 5 MW rated power have been set over the La Zacatosa site for wind farm installed capacities of 72 MW, 72.6 MW and 75 MW, respectively. Wind resource has been interpolated to their corresponding hub-heights and throughout the manufacturers' power curve, wind energy yield has been calculated from equation 6.1, consequently the wind farm capacity factors have been calculated from equation 6.2 from the wind resource simulations (Table 6.6). Additionally, the interaction between each turbine for the three different layouts has been addressed in the WRF model, which showed a reduction on the wind energy yield (equation 6.1) and hence on the corresponding capacity factors (equation 6.2). Finally, the effect of the wake downstream at the La Rumorosa I wind farm has been evaluated, and is showed in Table 6.8.

6.7 Four wind farms in close proximity analysis

Four wind farms have been simulated over the area of La Rumorosa, within the land areas occupied by the sites La Zacatosa, Jacomun, Canoas and Saucito (Fig. 6.1 and Table 6.1). Within these areas, three different wind turbine rated power models were set as Table 6.4. Wind energy yield is calculated (equation 6.1) for an interval of four weeks during 2014 and based on hub height wind speed at each turbine location from WRF simulations of both the resource only and with wake effect simulated, by applying the wind turbine parameterization model (Fitch et al., 2012). The number of turbines of each rated capacity at La Zacatosa was selected to develop a typical capacity factor of 0.28. For the other farms the same spacing was applied and the capacity factor calculated. The influence of all four planned wind farms on the performance of the La Rumorosa wind farm was subsequently assessed (equation 6.3). From the results obtained, these three wind farms have negligible effect on the wind energy yield at La Zacatosa for the interval studied. Nevertheless the wind energy yield deficit (equation 6.3) at

La Rumorosa I wind farm increases 0.29% for the 5 MW wind turbines within all the four farms, compared against the effect from La Zacatosa only.

6.7.1 Influence of wind turbine rating on energy yield from all farms

The Gamesa G87 2MW wind turbine model has been located at all the four sites for the amount and installed capacities described in Table 6.4. In total, 174 MW have been situated within all four farms. In a similar way as the resource only, wind speed values considering the wake effects are interpolated at the corresponding hub height (78 MW) and with the manufacturer's power curve and equation (6.1), the wind energy yield is calculated at each site. The capacity factor has been calculated from equation (6.2), for the wind resource and wake effects simulations, respectively and summarised in Table 6.9. The farm with the highest capacity factor for the resource only simulations is the La Zacatosa (32.51%), whereas when the wake effect is modelled the farm with highest capacity factor is Saucito (28.91%). For both simulations, the farms at Jacomun and Canoas have relatively low capacity factors due to the relatively sheltered positions and low mean wind speed at these locations compared to Zacatosa and Saucito.

Table 6.9 Wind energy yield and capacity factor for all the farms 2 MW case.

2 MW	Zacatosa	Jacomun	Saucito	Canoas
Resource Only (GWh)	15.728	4.974	5.938	4.622
Capacity Factor	32.51%	16.09%	31.56%	24.56%
Wake Effect (GWh)	13.925	4.505	5.439	4.280
Capacity Factor	28.78%	14.57%	28.91%	22.75%

Table 6.10 summarizes the wind energy yield calculated from the wind resource and from the wake effect WRF simulations for all the four farms with the Vestas

V112 3.3MW wind turbine. The wind farm from La Zacatosa develops the highest capacity factor for the wind resource only simulation. The Saucito wind farm, for the 3.3 MW wind turbine model, has the highest capacity factor value for the wake effect simulations. The Jacomun site has the lowest capacity factors for both types of simulation (Table 6.9).

Table 6.10 Wind energy yield and capacity factor for all the farms 3.3 MW case.

3.3 MW	Zacatosa	Jacomun	Saucito	Canoas
Resource Only (GWh)	17.539	5.653	7.158	5.683
Capacity Factor	35.95%	18.21%	35.87%	28.48%
Wake Effect (GWh)	14.782	4.754	6.326	4.889
Capacity Factor	30.30%	15.31%	31.70%	24.50%

The wind energy yield (equation 6.1) and capacity factors (equation 6.2) from the Gamesa G128, 5MW wind turbine model at all the four wind farms is described in Table 6.4. WRF results from the wind resource only simulation present the La Zacatosa wind farm with the highest capacity factor. Whereas from the wake effect simulation, the Saucito wind farm has the highest capacity factor value. The Jacomun wind farm has the lowest capacity factor amongst all the wind farms (Table 6.11).

Table 6.11 Wind energy yield and capacity factor for all the farms 5 MW case.

5 MW	Zacatosa	Jacomun	Saucito	Canoas
Resource Only (GWh)	16.242	5.254	6.846	5.080
Capacity Factor	34.53%	17.37%	33.96%	25.20%
Wake Effect (GWh)	13.678	4.457	5.963	4.392
Capacity Factor	29.08%	14.74%	29.58%	21.79%

6.7.2 Effect of Four wind farms in close proximity on La Rumorosa wind farm

The effect of all four wind farms operating at once with the wind turbine model over the performance of the La Rumorosa I wind farm was calculated. Wind energy yield was obtained from the wind resource simulations by equation 6.1, as wells as for the wake effect simulations. This was performed for the four wind farms and the three different wind turbine models of 2 MW, 3.3 MW and 5 MW. Their corresponding total installed capacities were 174 MW, 178.2 MW and 175 MW (Table 6.4), respectively. Once both wind energy yields were calculated, the energy yield deficit was obtained from equation 6.3. The wind energy yield at La Rumorosa I wind farm, from the wind resource only simulation, and for the wake effect simulations is presented in Table 6.12. From these wind energy yield values based on the WRF wake effect simulations, the wind energy yield deficit was calculated from equation 6.3, providing values of 1.25%, 1.57% and 1.69% of deficit for the wind farms with the 2 MW, 3.3 MW and 5 MW wind turbines models, respectively (Table 6.12).

Table 6.12 Wind energy yield at "La Rumorosa I" wind farm for four wind farms in close proximity cases.

All 4 Farms	2 MW	3.3 MW	5 MW
Wind Resource (GWh)	3.130	3.130	3.130
Wake Effect (GWh)	3.091	3.081	3.077
Deficit	**1.25%**	**1.57%**	**1.69%**

The wind speed deficit at 78 m height was calculated from equation (6.4). Wind speed values from the resource only simulations at La Zacatosa met-mast reached 5.95 m/s, downwind at La Rumorosa met-mast for the same simulations the wind speed is 10.34 m/s (Figure 6.7). However, for the wake effect simulation the wind speed was reduced to 9.97 m/s after considering the effects of all the four wind farms with the 2 MW wind turbine model. This wind speed is a deficit of 3.58%, which is 0.58% greater compared against the effect of

only La Zacatosa wind farm (Section 6.6.3). Nevertheless, after calculating the power from a 2 MW wind turbine at this location without the wake is 1,633 kW, and with the wake present is 1,518 kW, which corresponds to a 7.04 % of power deficit (1.2% bigger compared against the deficit from La Zacatosa wind farm in Section 6.6.3). Figure 6.7 (right) presents the wake from the 2MW wind turbines at all four wind farms. This is similar to the wake shown on Figure 6.5, the wake is presented within the blue area and reaches up to 108 m height and 12 km length.

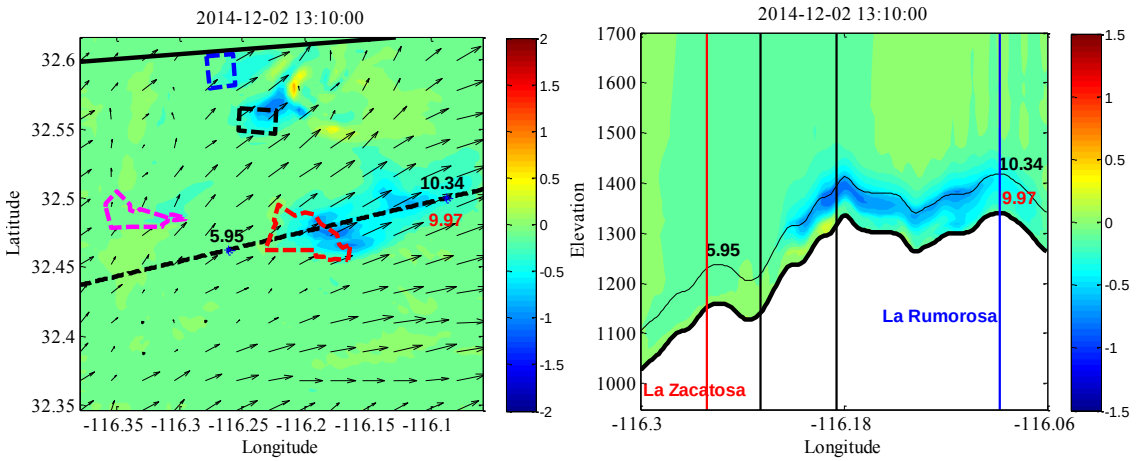

Figure 6.7 Wind speed difference (m/s) at 78 m height for farms of 2 MW wind turbines at the four sites. Horizontal section (left) shows wind farms (dashed regions) and plane (dashed line) of vertical section (right). Wind speed (m/s) shown without (black text) and with (red text) wake effect modelled from wind farm at La Zacatosa (red dashed region, vertical lines).

Simulations were also performed with the 5 MW wind turbine model over the four wind farms. Figure 6.8 presents the wind speed deficit at 78 m height over the La Rumorosa area. Wind speed at the La Rumorosa met-mast for the wake effect reaches 9.86 m/s, corresponding to a wind speed deficit of 4.64% (the effects from La Zacatosa only are 0.38% smaller, which shows that the other three farms have negligible effect over La Rumorosa I wind farm). Wind power at La Rumorosa met-mast for a 2 MW wind turbine for the resource only simulation is 1,633 kW, while after addressing the effects of the 5 MW wind turbines over the four wind farms, it is reduced to 1,481 kW, corresponding to a

9.31 % of power reduction. i.e. the power reduction is affected 0.83% more from all the four farms, compared against the effects from La Zacatosa farm only, this value is greater due to the electric power output changes with the wind turbine power curve. A vertical section of the plane which links the La Zacatosa met-mast with the La Rumorosa met-mast is presented in Figure 6.8 (right), where the wake shows a similar height and extent as for the 5 MW La Zacatosa wind farm from Figure 6.6.

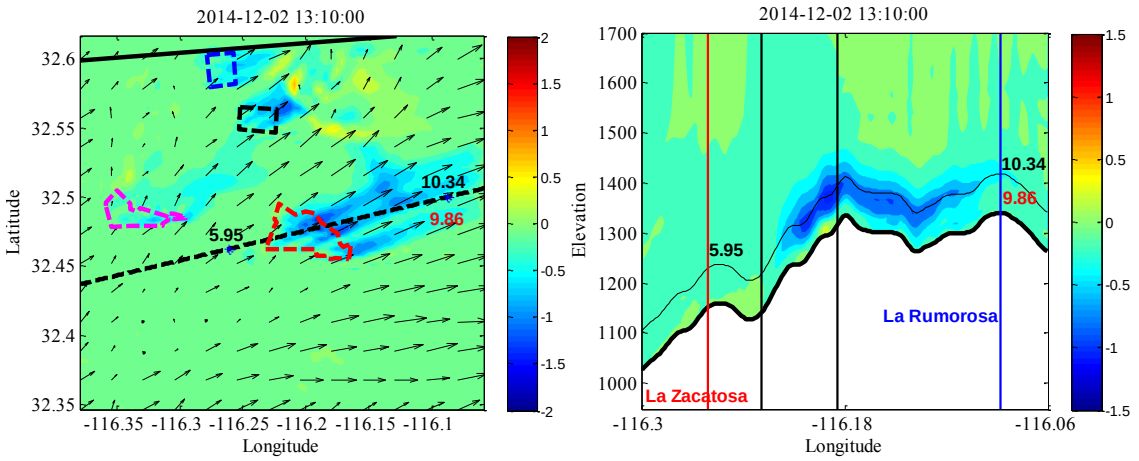

Figure 6.8 Wind speed difference (m/s) at 78 m height for farms of 5 MW wind turbines at the four sites. Horizontal section (left) shows wind farms (dashed regions) and plane (dashed line) of vertical section (right). Wind speed (m/s) shown without (black text) and with (red text) wake effect modelled from wind farm at La Zacatosa (red dashed region, vertical lines).

Wind speed and power deficits caused at La Rumorosa I wind farm for a single turbine due to the effect of all the close proximity wind farms wake effects is presented in Table 6.13. For the larger diameter turbines there is a greater deficit of wind speed, increasing from 3.58% up to 4.64%. As the electric power output varies based on the wind turbine power curve, the power deficits are greater than the speed deficits, with values from 7.04% up to 9.31%. Deficit values are slightly larger compared with the La Zacatosa wind farm effect over the La Rumorosa I wind farm, presented in Table 6.8, due to the contribution of the rest of the wind farms.

Table 6.13 Wind speed and power at "La Rumorosa I" wind farm for all the four wind farms.

All 4 Farms	2 MW		3.3 MW		5 MW	
	Speed (m/s)	Power (kW)	Speed (m/s)	Power (kW)	Speed (m/s)	Power (kW)
Wind Resource	10.34	1,633	10.34	1,633	10.34	1,633
Wake Effect	9.97	1,518	9.91	1,498	9.86	1,481
Deficit	**3.58%**	**7.04%**	**4.16%**	**8.24%**	**4.64%**	**9.31%**

In this section, the wind energy yield for the all four farms in the area of La Rumorosa, described in Table 6.1 and 6.4 has been calculated. Wind speed has been interpolated to the hub height and location of the corresponding wind turbine model with the power curve provided from the manufacturers the wind energy yield was calculated (equation 6.1) as well as the capacity factor (equation 6.2) for each wind farm and wind turbine model array. Furthermore, as WRF simulations have been performed considering the effect of the wind turbines' operation within the flow, wind energy yield has been calculated from these results (equation 6.1) and in the same way the capacity factors (equation 6.2). The wind energy yield and capacity factors values for each wind farm, for the resource only and wake effect simulation are presented on Tables 6.7 to 6.9. Lastly, the effect of the operation from these potential wind farms over the La Zacatosa wind farm has been evaluated throughout the wind energy yield deficit from equation (6.3) and it is presented in Table 6.7 for the three wind turbine models over the four sites.

6.8 Results and Discussion

In this Chapter, the WRF model has been applied to quantify the effect of electricity production from a proposed wind farm located directly upwind from an existing wind farm. For this analysis, an aggregated period from 2014 analysed for La Zacatosa met-mast in Section 4.3.2.2 was considered. Four area of land within the La Rumorosa region have been identified, with sizes from

491 ha to 1537 ha and distances between 10-25 km from the La Rumorosa I wind farm studied in earlier Chapters.

To define the wind turbine capacity installed in each area, the 2 MW wind turbine model was deployed for the La Zacatosa site. Based on the literature (DECC, 2015) a layout of 72 MW rated capacity was selected which develops a capacity factor of 28.78% considering the interaction from the wind turbines within the farm. The distance between wind turbines was kept constant to define the installed capacity over the other three pieces of land. For a 2 MW turbine, capacities of 46, 28 and 28 MW were selected over the areas Jacomun, Canoas and Saucito, respectively. Three wind turbines models were selected to perform the wind energy yield analysis, with rated powers of 2, 3.3 and 5 MW. The installed capacity from these last two wind turbine models at each piece of land, was set to the closest value corresponding to their 2 MW installed capacity. From these installed capacities, the effect of all four farms and La Zacatosa only on the La Rumorosa wind farm, located downwind, was studied.

Six cases were defined based on the number of farms (one or the four) and the three wind turbines models (2, 3.3 and 5 MW rated power). Two simulations were performed for each one of the cases, one analysing the wind resource and wind energy yield at hub height for each wind turbine model, and the other considering the Fitch et al. (2012) parameterization scheme at the location of every single wind turbine. From Chapter 4, the WRF model configuration NARR 5-3-1 was the one that provided smallest root mean square error relative to the measured met-mast data. Wind energy yield was calculated based on resource only simulations, without considering any effect from the wind turbines. Additionally, WRF simulations with this configuration were

conducted considering the Fitch et al. (Fitch et al., 2012) scheme at the wind turbines locations for each one of the six cases aforementioned.

For the 2 MW wind turbine model deployed at La Zacatosa, the wind energy yield was of 15.628 GWh for the wind resource only, and decreased to 13.922 GWh when accounting the wind turbines interactions, the capacity factors were 32.30% and 28.78%, respectively. Based on the 3.3 MW wind turbine model, the wind energy yield reached 17.539 GWh for the resource simulation and was of 14.840 GWh for the wind turbines simulations, capacity factors for these two simulations were of 35.95% and 30.42%, respectively. The latter wind turbine model provided 16.242 GWh at La Zacatosa wind farm for the wind resource simulations, which decreased to 13.708 GWh after accounting the interaction between the wind turbines, the correspondent capacity factors were of 34.53% and 29.14%

The downstream effect of the La Zacatosa wind farm on the La Rumorosa I wind farm was analysed. The wind energy yield during the aggregated period at La Rumorosa I wind farm was 3.130 GWh. Energy extraction by turbines at La Zacatosa wind farm reduced the La Rumorosa I energy yield by between 1.09 – 1.41% (Table 6.7). The energy yield reduction was higher for a farm of 14 5 MW turbines than for a farm of 36 2 MW turbines. Over the time period considered the wind direction was from a range of headings. For the heading 75 degrees (East-Northeast) for which La Zacatosa wind farm is directly upwind of La Rumorosa wind farm, the power output at La Rumorosa was reduced by 5.84 % and 8.48 % for 2 MW and 5 MW turbines respectively.

Wind energy yield for all the farms with the 2 MW wind turbine model went from 31.262 GWh from the wind resource only simulations to 28.149 GWh after implementing the wind turbine parameterization model over each one of them. Capacity factors were from 32.51% to 28.78% for La Zacatosa wind farm, while for the Jacomun was 16.09% to 14.57%, the Saucito farm provided 31.56% down to 28.91%, and finally, the Canoas site, which had a capacity factor of 24.56% and then 22.75%, all these factors were for the wind resource simulations only values and for the simulations considering the wake effect for each farm, respectively. Considering the influence of four proposed farms, the La Rumorosa I wind farm energy yield was reduced by 1.25%, 1.57% and 1.69%, respectively for the 2MW, 3.3MW and 5 MW turbines (Table 6.12). The power reduction effect of all these wind farms over the La Rumorosa was particularly calculated for the East-Northeast wind heading (75 degrees), from which the La Zacatosa wind farms is directly downstream the La Rumorosa wind farm. From this analysis, the total installed capacity of 174 MW for the four wind farms with the 2 MW wind turbine model caused a wind speed deficit of 3.58 % which means a 7.04 % of wind power deficit for a 2 MW wind turbine. For the case of the 5 MW wind turbines over the four farms, a total installed capacity of 175 MW increased the wind speed deficit to 4.64 %, which in terms of power is a reduction of 9.31 %.

Chapter 7 Conclusions

Wind resource assessment from numerical weather prediction models provides the opportunity to explore wind resource over a geographic region before installation of a met-mast and wind farm. This study has focused on the impact of one and four wind farms located in close proximity and upwind of an existing wind farm. A review of the literature concerning Numerical Weather Prediction models identified that the Weather Research and Forecasting (WRF) model is increasingly used for simulation of both wind resource and energy yield from wind farms. The accuracy of the WRF model has been assessed for predicting the wind resource and energy yield measured at a full-scale wind farm located in a region of complex terrain.

Two time intervals have been studied. The first interval covered two consecutive weeks from 2011, which described statistically the annual wind speed distribution from a 50 m high met-mast at the site of an existing wind farm comprising five turbines each rated at 2 MW. The second interval considered four aggregated weeks from 2014, which represented statistically the annual wind speed and direction distribution (i.e. the wind rose) from an 80 m high met-mast located at the site of a proposed wind farm of approximately 70 MW installed capacity upwind of the existing farm.

For both time intervals WRF prediction accuracy was assessed against both wind speed at 50 m height at the existing wind farm and energy yield of the same farm obtained from the Supervisory Control and Data Acquisition (SCADA) system. For the 2011 dataset, accuracy obtained for La Rumorosa met-mast was within 1.8% for the histogram describing wind speed occurrence, 1.4% for the Weibull distribution and 11.7% coefficient of variation for the time series. The input dataset NARR with model configuration 5-3-1 (MYNN Level 2.5 PBL, Rapid Update Cycle LSM and Revised Monin-Obukov MM5 SL model)

performed most accurately. For all simulations an overprediction of peak wind speed was observed. This limitation of the model follows from the spatial and temporal resolution from the initial and boundary conditions, which are respectively between 28 km to 32 km and from 3 to 6 hours.

For the interval during 2014, at the La Zacatosa met-mast location, the accuracy was within 1.5% for the probability of wind speeds occurrence histogram, 0.9% for the Weibull distribution, 11.5% *RMSE* for the time series and 26.5% for the wind rose distribution, for this case, the NARR 5-3-1 was the configuration which performed more accurately, being the wind rose distribution the driving metric to select the method for the wind turbines wake simulations. A limitation for this case was that the wind rose for the aggregated period differed by 9.24% from the annual measured wind rose and thus represented a slightly wider range of wind directions than the annual data.

Wind energy yield from the existing farm at La Rumorosa was underpredicted by 1.04% for the two-week 2011 interval, but only within 5.25% for the four-week 2014 interval. The 2011 interval was selected based on the similarity to the annual probability of wind speeds occurrence. Whereas the 2014 one, was chosen based on the similarity of the probability of wind speed and direction occurrence (i.e. wind rose), the latter having a greater discrepancy to annual data, compared to the 2011 interval.

The capability of WRF to calculate the net drag imposed by a wind farm on the flow has been assessed for a single row wind farm. Samples were identified for which the wind heading was aligned with the wind farm layout and the onset flow, power and loading to each turbine within the farm evaluated for these intervals. Net thrust force has been calculated from wind speed values obtained at wind turbine hub heights from WRF simulations, from the thrust coefficient from the manufacturer's data. For the case with similar wind speeds, a mean

wind speed error within 0.86% was obtained from the WRF results, compared against measured data. For this case, the variation of wind speed and power between the wind turbines was not predicted by the WRF model. Nevertheless, the net thrust force has been calculated for both measured and simulated data at the wind turbines locations, with good agreement.

The wind speed, power and energy yield deficits over an existing farm due to the operation of a wind farm with geographic centre 10 km upwind of the existing farm has been evaluated. The upwind farm was defined with an installed capacity of 72 MW comprising 2 MW wind turbines and a capacity factor of 28.78%, which is typical for onshore wind projects in the UK (DECC, 2015). For an interval when the wind heading was from the upwind farm with speed 10.34 m/s, wind speed and power output of the existing farm were reduced by 3.58% and 7.04% respectively. Over the four-week interval from 2014, and the NARR 5-3-1 WRF model configuration, the wind energy yield deficit was 1.09% compared against the wind resource only simulations.

For the same model configuration and sample time, the effect of the same wind farm with 70 MW installed capacity of 5 MW turbines with a capacity factor of 29.14% was studied. For this upwind farm, deficits obtained for wind speed and power at the existing farm were 4.26% and 8.48% respectively and the wind energy yield deficit was 1.14%. Deficits of velocity and power output at the existing farm are therefore larger if the upwind farm comprises the 5 MW turbines, rather than the 2 MW turbines. This is due to the larger rotor diameter resulting in the need of a longer distance downwind for the wake to recover.

The operation of four wind farms within the region, with a total installed capacity of 175 MW has been evaluated. All farms comprised 5 MW turbines. The installed capacity per farm was 70 MW, 45 MW, 30 MW and 30 MW, at corresponding distances upwind from an existing farm of 10.6 km, 23.6 km,

19.55 km and 15.07 km. The wind speed and power were reduced by 4.64% and 9.31% respectively, these considering the single interval aforementioned. The wind energy yield deficits over the existing wind farm due to four upwind farms over the 2014 aggregated period was 1.69%. This energy yield deficit is 0.29% greater than the deficit from the single 70 MW upwind farm, showing that the rest of the farms, apart from the La Zacatosa, have limited influence over the La Rumorosa I wind farm. The influence of wake effect on annual energy yield may however be underestimated since the wind rose for the aggregated four week interval during 2014 represents a wider range of wind headings than the annual wind rose during this year.

From the wind resource evaluation, two potential wind farm sites with wind power capacity factors of 31.70% and 30.30% have been identified within the La Rumorosa region. These sites have installed capacities of 29.7 MW and 72.6 MW, respectively and are located 15.07 km NW and 10.6 km WSW away from the existing wind farm. The annual energy yield from these farms is estimated to be 21.10 GWh. This is approximately 14 times the yield from the existing wind farm within this region for which the yield may be expected to reduce by the order of 1-2%. This study has highlighted the feasibility to invest and develop wind energy projects based on the wind resource assessment from the WRF model, which has been validated from two met-masts and an existing wind farm over the area of La Rumorosa.

7.1 Future Work

To further develop understanding of the suitability of WRF for wind resource and wake effect assessments, the further analysis could be performed.

- **Location of the wind resource assessment**

So far the study has been performed over a region of the Northwest of Mexico. Performing an accuracy assessment of the WRF model, and being validated at a

different geographic location will help to characterize the accuracy of the meteorological datasets and model configuration. However, the North American Mesoscale model and the North American Regional Reanalysis model, provide the data only for the area of Mexico, United States and Canada. Global datasets will have to be employed at a different location, such as the Global Forecast System dataset.

- **Topographic characteristics**

The terrain within the region of the present study comprises several plateaus and deep valleys. Within an area of 20 x 20 km, elevation varies from 800 to 1400 m with steep slopes. Turbines within the five-turbine case study farm have hub height elevations that differ by up to half a diameter. Within the larger farms modelled hub height elevations differ by up to two diameters. Further analysis of the effect of slope steepness and the resolution of topographic data would be of value for increasing confidence in resource predictions in such regions. The rate of mixing between wakes that are developed from turbines with significantly differing up height also requires further study.

- **Local wind speed characteristics**

For the case studied, the wind speed values ranged from 0 m/s to 18 m/s for the 50 m height met-mast, while for the 80 m height met-mast, the wind speed ranged between 0 m/s to 15 m/s, based on the 10 min averaged samples. Within the finest resolution domain two wind farms with capacity factor higher than 30% were identified. Evaluating the accuracy of the WRF models within areas with a greater wind speed resource, will allow to identify the suitable WRF model configuration, as well as the meteorological dataset for such characteristics, in order to perform reliable wind resource assessment analysis over areas with potential more feasible compared against the La Rumorosa.

- **Size and layout of the wind farm from which the data is accessed**

The wind farm considered for the wind turbine model from WRF (Fitch et al., 2012) was evaluated over a single row with five wind turbines farm. From the statistical distribution of the wind direction, there were only a small number of samples for which the wind was blowing aligned to the wind farm layout and this was generally for low wind speeds. Analysis of further data for aligned cases would be of value to evaluate the wake effect from the wind turbines within the farm..

- **Representative aggregated period**

From the wind resource assessment and wake effect analysis performed, the four aggregated week periods represented the annual wind speed and direction distribution within an $RMSE_{\theta}$ value of 9.242%. Evaluation of met-mast data for different years can be performed, to identify an aggregated period with a smaller variation from the annual wind speed and direction distribution. This will improve confidence in projection of the WRF results from the aggregated period to the full year.

- **Number of domains of WRF model for wake effect analysis**

The wind resource evaluation sensitivity analysis was performed with a five nested domains, covering a total area of 2,527 km by 2,527 km from the outer domain, whereas the analysis performed to evaluate the wake effect from a single and multiple farms from the WRF wind turbine model, was performed based on a single domain mesh. Performing a multiple nested domains simulation will expand the area covered from the analysis, which will increase the data gathered from the meteorological datasets for the initial and boundary conditions.

- **Wind turbine parameterization model**

As described on the literature (Volker et al., 2012) the wind turbine scheme from the WRF model (Fitch et al., 2012) does not consider any performance deficit due to the interaction between multiple turbines located within the same cell. For the present study all simulations comprised a maximum of one turbine per cell. However, further development and analysis of wind turbine parameterization models which address the attenuation of the wake downstream should be performed to validate the applicability of each model based on the amount and spacing of wind turbines within and downwind within a wind farm.

- **Turbulent kinetic energy vertical from WRF assessment**

The WRF model in conjunction with semi empirical wake models (i.e. OpenWind) can be applied to implement the wind speed fields at hub height from the former into the latter, to describe the power and thrust characteristics of a turbine, or group of turbines within a farm. This will describe the operative performance accounting the interaction with the wind turbines form the surrounding. Eventually, this data (i.e. power coefficient (C_p) and thrust coefficient (C_T) curves) can be defined within the WRF model, to describe the downwind wake from the wind turbines. In a similar way, the WRF model can be paired with a CFD model (i.e. StarCCM), to employ the vertical wind speed profile from the former as input into the latter, to describe the thrust and power along the rotor diameter and calculate the C_p and C_T curves at hub height, to finally, be introduced within the WRF model to obtain a better description of the wake due to the more accurate turbine operative characteristics (i.e. C_T, C_P). Finally, from the CFD simulations, the Turbulent Kinetic Energy (*TKE*) can be calculated over the wind turbine(s) operative range, in order to identify the discrepancy against the WRF wake model formulation, based on the Fitch et al. (2012) scheme, which states that the $C_{TKE}=C_T-C_P$.

Bibliography

Ainslie, J. F., (1988). Calculating the flowfield in the wake of wind turbines. *Journal of Wind Engineering and Industrial Aerodynamics,* 27(1–3)**,** 213-224.

Al-Yahyai, S., Charabi, Y. & Gastli, A., (2010). Review of the use of Numerical Weather Prediction (NWP) Models for wind energy assessment. *Renewable and Sustainable Energy Reviews,* 14(9)**,** 3192-3198.

Alemán-Nava, G. S., Casiano-Flores, V. H., Cárdenas-Chávez, D. L., Díaz-Chavez, R., Scarlat, N., Mahlknecht, J., Dallemand, J.-F. & Parra, R., (2014). Renewable energy research progress in Mexico: A review. *Renewable and Sustainable Energy Reviews,* 32**,** 140-153.

Ávila, G., Meléndez, M. E. M. & Rubio, G. O. (2011). *Hacia la sustentabilidad ambiental de la producción de energía en México*.

Barry, R. G. & Chorley, R. J. (2009). *Atmosphere, weather and climate*. Routledge.

Bei, N., Li, G., Zavala, M., Barrera, H., Torres, R., Grutter, M., Gutiérrez, W., García, M., Ruiz-Suarez, L. G., Ortinez, A., Guitierrez, Y., Alvarado, C., Flores, I. & Molina, L. T., (2013). Meteorological overview and plume transport patterns during Cal-Mex 2010. *Atmospheric Environment,* 70(0)**,** 477-489.

Blahak, U., Goretzki, B. & Meis, J., (2010). A simple parameterization of drag forces induced by large wind farms for numerical weather prediction models. *Proc. European Wind Energy Conf. and Exhibition 2010***,** 186-189.

Burton, T., Sharpe, D., Jenkins, N. & Bossanyi, E. (2001). *Wind Energy Handbook*. John Wiley & Sons.

Byrkjedal, Ø., Bredesen, R. E., Keck, R.-E., Sondell, N. & Berge, E., (2014). Properties of a wind farm wake as simulated by a numerical weather prediction model for the Smøla wind farm. *EWEA*.

Capps, S. B., Hall, A. & Hughes, M., (2012). Sensitivity of southern California wind energy to turbine characteristics. *Wind Energy***,** n/a-n/a.

Carta, J. A. & Ramírez, P., (2007). Analysis of two-component mixture Weibull statistics for estimation of wind speed distributions. *Renewable Energy,* 32(3)**,** 518-531.

Carvalho, D., Rocha, A., Gómez-Gesteira, M. & Silva Santos, C., (2012). A sensitivity study of the WRF model in wind simulation for an area of high wind energy. *Environmental Modelling & Software,* 33(0)**,** 23-34.

CDHCU. (2015). General Law of Climate Change. Available from: http://www.diputados.gob.mx/LeyesBiblio/pdf/LGCC_130515.pdf

CFE, (2014). Rumorosa met-mast wind speed. Tecate, Baja California.

Clark, J. S., Carpenter, S. R., Barber, M., Collins, S., Dobson, A., Foley, J. A., Lodge, D. M., Pascual, M., Pielke, R., Pizer, W., Pringle, C., Reid, W. V., Rose, K. A., Sala, O., Schlesinger, W. H., Wall, D. H. & Wear, D., (2001). Ecological Forecasts: An Emerging Imperative. *Science,* 293(5530)**,** 657-660.

Crespo, A., Hernández, J. & Frandsen, S., (1999). Survey of modelling methods for wind turbine wakes and wind farms. *Wind Energy,* 2(1)**,** 1-24.

Chagas, G., Guedes, R. & Manso, M., (2009). Estimating wind resource using mesoscale modeling. *European Wind Energy Conference EWEC 2009*.

Chang, T. P., (2011). Performance comparison of six numerical methods in estimating Weibull parameters for wind energy application. *Applied Energy,* 88(1)**,** 272-282.

Chavez, R., Probst, O. & Lozano, S., (2012a). Evaluation of the wind resource for a coastal site in Mexico by combining WindSim with WRF. *EWEA 2012*.

Chavez, R., Probst, O. & Lozano, S., (2012b). Mesoscale modeling of the wind resource at a complex coastal site. *EWEA 2012*.

Chenghai, W., Shuanglong, J., Ju, H., Feimin, Z., Shuanglei, F. & Chun, L., (2011). Comparing different boundary layer schemes of WRF by simulation the low-level wind over complex terrain. *Artificial Intelligence, Management Science and Electronic Commerce (AIMSEC), 2011 2nd International Conference on***,** 6183-6188.

Chin, H., Glascoe, L., Lundquist, J. & Wharton, S., (2010). Impact of WRF physics and grid resolution on low-level wind prediction: towards the assessment of climate change impact on future wind power. *Fifth International Symposium on Computational Wind Engineering***,** 23-27.

Christiansen, M. B. & Hasager, C. B., (2005). Wake effects of large offshore wind farms identified from satellite SAR. *Remote Sensing of Environment,* 98(2–3)**,** 251-268.

DECC. (2015). Digest of United Kingdom energy statistics. Available from: https://www.gov.uk/government/uploads/system/uploads/attachment_data/file/450298/DUKES_2015_Chapter_6.pdf

Deppe, A. J., Gallus, W. A. & Takle, E. S., (2013). A WRF Ensemble for Improved Wind Speed Forecasts at Turbine Height. *Weather and Forecasting,* 28(1)**,** 212-228.

DOF, (2015). Renewable Energy Target for 2018. Mexico.

Draxl, C., Hahmann, A. N., Pena Diaz, A., Nissen, J. N. & Giebel, G., (2010). Validation of boundary-layer winds from WRF mesoscale forecasts with applications to wind energy forecasting.

Dudhia, J., (1989). Numerical Study of Convection Observed during the Winter Monsoon Experiment Using a Mesoscale Two-Dimensional Model. *Journal of the Atmospheric Sciences,* 46(20)**,** 3077-3107.

Eriksson, O., Lindvall, J., Breton, S. P. & Ivanell, S., (2015). Wake downstream of the Lillgrund wind farm - A Comparison between LES using the actuator disc method and a Wind farm Parametrization in WRF. *Journal of Physics: Conference Series,* 625(1)**,** 012028.

FB&EI, F. B. E. I. (2012). An Economic and Comprehensive Analysis For the Cali-Baja Mega-Region. Available from: http://www.pointloma.edu/sites/default/files/filemanager/Fermanian_Bu

siness__Economic_Institute/Economic_Reports/Sempra_sierra_juarez_V3.pdf.

Fitch, A. C., Olson, J. B., Lundquist, J. K., Dudhia, J., Gupta, A. K., Michalakes, J. & Barstad, I., (2012). Local and Mesoscale Impacts of Wind Farms as Parameterized in a Mesoscale NWP Model. *Monthly Weather Review,* 140(9)**,** 3017-3038.

Fitch, A. C., Olson, J. B., Lundquist, J. K., Dudhia, J., Gupta, A. K., Michalakes, J., Barstad, I. & Archer, C. L., (2013). CORRIGENDUM. *Monthly Weather Review,* 141(4)**,** 1395-1395.

Foley, A. M., Leahy, P. G., Marvuglia, A. & McKeogh, E. J., (2012). Current methods and advances in forecasting of wind power generation. *Renewable Energy,* 37(1)**,** 1-8.

Gamesa. (2007). *Gamesa G87-2.0 MW Brochure.* [Online] Available from: http://www.iberdrolarenewables.us/deerfield/Zimmerman/DFLD-JZ-Rev5a-GamesaBrochure.pdf [Accessed April 6 2013].

Gilliam, R. C. & Pleim, J. E., (2009). Performance Assessment of New Land Surface and Planetary Boundary Layer Physics in the WRF-ARW. *Journal of Applied Meteorology and Climatology,* 49(4)**,** 760-774.

Google, (2012). Google Earth.

Hansen, K. S., Barthelmie, R. J., Jensen, L. E. & Sommer, A., (2012). The impact of turbulence intensity and atmospheric stability on power deficits due to wind turbine wakes at Horns Rev wind farm. *Wind Energy,* 15(1)**,** 183-196.

Hartmann, D. L., (1988). On the Comparison of Finite-Element to Finite-Difference Methods for the Representation of Vertical Structure in Model Atmospheres. *Monthly Weather Review,* 116(1)**,** 269-273.

Henderson-Sellers, A., Yang, Z. L. & Dickinson, R. E., (1993). The Project for Intercomparison of Land-surface Parameterization Schemes. *Bulletin of the American Meteorological Society,* 74(7)**,** 1335-1349.

Hidalgo, A., Jiménez, P. A., Navarro, J., Conte, J., González-Rouco, J. F. & Prieto, L., (2014). Evaluation of the Wind Farms' impact on onshore wind resource availability. *EWEA*.

Horvath, K., Koracin, D., Vellore, R., Jiang, J. & Belu, R., (2012). Sub-kilometer dynamical downscaling of near-surface winds in complex terrain using WRF and MM5 mesoscale models. *Journal of Geophysical Research: Atmospheres,* 117(D11)**,** D11111.

Hu, X.-M., Klein, P. M. & Xue, M., (2013). Evaluation of the updated YSU planetary boundary layer scheme within WRF for wind resource and air quality assessments. *Journal of Geophysical Research: Atmospheres,* 118(18)**,** 10,490-10,505.

Hu, X.-M., Nielsen-Gammon, J. W. & Zhang, F., (2010). Evaluation of three planetary boundary layer schemes in the WRF model. *Journal of Applied Meteorology and Climatology,* 49(9)**,** 1831-1844.

IIE. (2016). *Sistema de Información Geográfica para las Energías Renovables en México.* [Online] Available from: http://sag01.iie.org.mx/siger/ [Accessed 2016].

INEGI. (2012). *México en Cifras.* [Online] Available from: http://www3.inegi.org.mx/sistemas/mexicocifras/default.aspx?e=2 [Accessed January 20 2012].

Inness, P. M. & Dorling, S. (2012). *Operational Weather Forecasting*. John Wiley & Sons.

Janjić, Z. I., (2002). Nonsingular implementation of the Mellor–Yamada level 2.5 scheme in the NCEP Meso model. *NCEP office note,* 437**,** 61.

Jiménez, P. A. & Dudhia, J., (2011). Improving the Representation of Resolved and Unresolved Topographic Effects on Surface Wind in the WRF Model. *Journal of Applied Meteorology and Climatology,* 51(2)**,** 300-316.

Jiménez, P. A., Dudhia, J., González-Rouco, J. F., Montávez, J. P., García-Bustamante, E., Navarro, J., Vilà-Guerau de Arellano, J. & Muñoz-Roldán, A., (2013). An evaluation of WRF's ability to reproduce the surface wind over complex terrain based on typical circulation patterns. *Journal of Geophysical Research: Atmospheres,* 118(14)**,** 7651-7669.

Jiménez, P. A., González-Rouco, J. F., García-Bustamante, E., Navarro, J., Montávez, J. P., de Arellano, J. V.-G., Dudhia, J. & Muñoz-Roldan, A., (2010). Surface wind regionalization over complex terrain: Evaluation and analysis of a high-resolution WRF simulation. *Journal of Applied Meteorology and Climatology,* 49(2)**,** 268-287.

Jiménez, P. A., Navarro, J., Palomares, A. M. & Dudhia, J., (2015). Mesoscale modeling of offshore wind turbine wakes at the wind farm resolving scale: a composite-based analysis with the Weather Research and Forecasting model over Horns Rev. *Wind Energy,* 18(3)**,** 559-566.

Kimura, R., (2002). Numerical weather prediction. *Journal of Wind Engineering and Industrial Aerodynamics,* 90(12–15)**,** 1403-1414.

Landberg, L. (2015). *Meteorology for Wind Energy: An Introduction*. John Wiley & Sons.

Landberg, L., Myllerup, L., Rathmann, O., Petersen, E. L., Jørgensen, B. H., Badger, J. & Mortensen, N. G., (2003). Wind Resource Estimation—An Overview. *Wind Energy,* 6(3)**,** 261-271.

Le Matre, O. & Knio, O. M., (2010). Spectral methods for uncertainty quantification. *Scientific Computation. Springer, New York*.

LeVeque, R. J. (2007). *Finite difference methods for ordinary and partial differential equations: steady-state and time-dependent problems*. Vol. 98: Siam.

Lindvall, J., Byrkjedal, Ø., Eriksson, O. & Ivanell, S., (2015). Simulating wind farms in the Weather Research and Forecasting model, resolution sensitivities. *Proc. European Offshore Wind Energy Conf. and Exhibition*.

Liu, Y., Warner, T., Liu, Y., Vincent, C., Wu, W., Mahoney, B., Swerdlin, S., Parks, K. & Boehnert, J., (2011). Simultaneous nested modeling from the

synoptic scale to the LES scale for wind energy applications. *Journal of Wind Engineering and Industrial Aerodynamics,* 99(4)**,** 308-319.

Liu, Y., Warner, T. T., Bowers, J. F., Carson, L. P., Chen, F., Clough, C. A., Davis, C. A., Egeland, C. H., Halvorson, S. F., Huck, T. W., Lachapelle, L., Malone, R. E., Rife, D. L., Sheu, R.-S., Swerdlin, S. P. & Weingarten, D. S., (2008). The Operational Mesogamma-Scale Analysis and Forecast System of the U.S. Army Test and Evaluation Command. Part I: Overview of the Modeling System, the Forecast Products, and How the Products Are Used. *Journal of Applied Meteorology and Climatology,* 47(4)**,** 1077-1092.

Lo, J. C.-F., Yang, Z.-L. & Pielke, R. A., (2008). Assessment of three dynamical climate downscaling methods using the Weather Research and Forecasting (WRF) model. *Journal of Geophysical Research: Atmospheres,* 113(D9)**,** n/a-n/a.

Lynch, P., (2008). The origins of computer weather prediction and climate modeling. *Journal of Computational Physics,* 227(7)**,** 3431-3444.

Macrae, N. (2000). *John von Neumann: The scientific genius who pioneered the modern computer, game theory, nuclear deterrence, and much more*. American Mathematical Soc.

Machenhauer, B., Kaas, E. & Hjort Lauritzen, P., (2009). Finite-Volume Methods in Meteorology. *In:* Ciarlet, P. G. (ed.) *Handbook of Numerical Analysis.* Vol. Volume 14. Elsevier. 3-120.

Manwell, J. F., McGowan, J. G. & Rogers, A. L. (2002). *Wind Energy Explained : Theory, Design and Application*. Wiley.

McIlveen, R. (1992). *Fundamentals of weather and climate*. Psychology Press.

Mesinger, F., DiMego, G., Kalnay, E., Mitchell, K., Shafran, P. C., Ebisuzaki, W., Jović, D., Woollen, J., Rogers, E., Berbery, E. H., Ek, M. B., Fan, Y., Grumbine, R., Higgins, W., Li, H., Lin, Y., Manikin, G., Parrish, D. & Shi, W., (2006). North American Regional Reanalysis. *Bulletin of the American Meteorological Society,* 87(3)**,** 343-360.

Michelson, S. A. & Bao, J.-W., (2008). Sensitivity of low-level winds simulated by the WRF model in California's Central Valley to uncertainties in the large-scale forcing and soil initialization. *Journal of Applied Meteorology and Climatology,* 47(12)**,** 3131-3149.

Miller, A., Chang, B., Issa, R. & Chen, G., (2013). Review of computer-aided numerical simulation in wind energy. *Renewable and Sustainable Energy Reviews,* 25(0)**,** 122-134.

Monin, A. & Obukhov, A., (1954). Basic laws of turbulent mixing in the surface layer of the atmosphere. *Contrib. Geophys. Inst. Acad. Sci. USSR,* 151**,** 163-187.

Muñoz, G., Campbell, H., Díaz, E. & Quintero, M. (2012). *Baja California: Perfil Energético 2010-2020*. Comisión Estatal de Energía de Baja California.

Nakanishi, M. & Niino, H., (2006). An Improved Mellor–Yamada Level-3 Model: Its Numerical Stability and Application to a Regional Prediction of Advection Fog. *Boundary-Layer Meteorology,* 119(2)**,** 397-407.

NASA, A. G., (2011). ASTER Global Digital Elevation Model Version 2 – Summary of Validation Results. ASTER GDEM Validation Team.

NCWCP, N. C. f. W. a. C. P. (2013). *GLOBAL FORECAST SYSTEM.* [Online] Available from: http://www.emc.ncep.noaa.gov/index.php?branch=GFS [Accessed 15 November 2013].

NESDIS, N. E. S. D. a. I. S. (2013). *North American Regional Reanalysis Daily Dataset.* [Online] Available from: http://nomads.ncdc.noaa.gov/cgi-bin/ncdc-ui/define-collection.pl?model_sys=narr&model_name=narr-a&grid_name=221 [Accessed 15 November].

NREL. (2004). *Baja California Norte Border Region 50m Wind Power.* [Online]: U.S. Department of Energy, National Renewable Energy Laboratory. Available from: http://www.nrel.gov/wind/pdfs/mexico_baja.pdf [Accessed 20 October 2012].

NRG. (2010a). *RNRG 40C ANEMOMETER.* [Online] Available from: https://www.renewablenrgsystems.com/products/met-sensors/anemometers/detail/40c-anemometer [Accessed 2014].

NRG. (2010b). *RNRG 200P WIND VANE.* [Online] Available from: https://www.renewablenrgsystems.com/products/met-sensors/wind-direction-vanes/detail/200p-wind-vane [Accessed 2014].

NRG. (2010c). *SYMPHONIEPLUS®3 DATA LOGGER.* [Online] Available from: https://www.renewablenrgsystems.com/products/data-loggers/detail/symphonieplus3-data-logger [Accessed 2014].

NRG, (2015). #40C Anemometer Uncertainty. *Application Note.*

Obukhov, A. M., (1971). Turbulence in an atmosphere with a non-uniform temperature. *Boundary-Layer Meteorology,* 2(1)**,** 7-29.

Park, S. & Bretherton, C. S., (2009). The University of Washington Shallow Convection and Moist Turbulence Schemes and Their Impact on Climate Simulations with the Community Atmosphere Model. *Journal of Climate,* 22(12)**,** 3449-3469.

Pielke Sr, R. A. (2013). *Mesoscale meteorological modeling*. Vol. 98: Academic press.

Pleim, J. E. & Xiu, A., (2003). Development of a Land Surface Model. Part II: Data Assimilation. *Journal of Applied Meteorology,* 42(12)**,** 1811-1822.

Puga, N., (2008). Wind energy resource development along the Baja California-U.S. Border: progress and potential hurdles. *BORDER ENERGY FORUM XV*.

Reddy, J. N. (2014). *An Introduction to Nonlinear Finite Element Analysis: with applications to heat transfer, fluid mechanics, and solid mechanics*. OUP Oxford.

Reuters. (2015). *Mexico sees $14 bln in wind energy investment by 2018.* [Online] Available from: http://www.reuters.com/article/mexico-energy-idUSL1N0US06X20150113 [Accessed 4 December 2015].

Richardson, L. F. (1922). *Weather prediction by numerical process*. Cambridge University Press.

Rife, D. L., Davis, C. A., Liu, Y. & Warner, T. T., (2004). Predictability of Low-Level Winds by Mesoscale Meteorological Models. *Monthly Weather Review,* 132(11)**,** 2553-2569.

Rogers, A. L., Rogers, J. W. & Manwell, J. F., (2005). Comparison of the performance of four measure–correlate–predict algorithms. *Journal of Wind Engineering and Industrial Aerodynamics,* 93(3)**,** 243-264.

Rogers, E., DiMego, G., Black, T., Ek, M., Ferrier, B., Gayno, G., Janjic, Z., Lin, Y., Pyle, M. & Wong, V., (2009). The NCEP North American mesoscale modeling system: Recent changes and future plans. *Preprints, 23rd Conference on Weather Analysis and Forecasting/19th Conference on Numerical Weather Prediction*.

Schultz, D. M., Anderson, S., Fairman, J. G., Lowe, D., McFiggans, G., Lee, E. & Seo-Zindy, R., (2014). ManUniCast: A Community Weather and Air-Quality Forecasting Teaching Portal. *EGU General Assembly Conference Abstracts,* 16**,** 11448.

Seguro, J. V. & Lambert, T. W., (2000). Modern estimation of the parameters of the Weibull wind speed distribution for wind energy analysis. *Journal of Wind Engineering and Industrial Aerodynamics,* 85(1)**,** 75-84.

SIGEA. (2006). Proyecto Eoloeléctrico Baja California 2000. Available from: http://sinat.semarnat.gob.mx/dgiraDocs/documentos/bc/estudios/2006/02BC2006E0013.pdf

Singer, M., Mirocha, J., Lundquist, J. & Cleve, J., (2010). Implementation and assessment of turbine wake models in the Weather Research and Forecasting model for both mesoscale and large-eddy simulation. *International Symposium on Computational Wind Engineering*.

Skamarock, W., Klemp, J., Dudhia, J., Gill, D. & Barker, D., (2005). A description of the Advanced Research WRF version 3. Note NCAR/TN-4751STR.

Skamarock, W. C. & Klemp, J. B., (2008). A time-split nonhydrostatic atmospheric model for weather research and forecasting applications. *Journal of Computational Physics,* 227(7)**,** 3465-3485.

Smirnova, T. G., Brown, J. M., Benjamin, S. G. & Kim, D., (2000). Parameterization of cold-season processes in the MAPS land-surface scheme. *Journal of Geophysical Research: Atmospheres,* 105(D3)**,** 4077-4086.

Soler-Bientz, R., Watson, S. & Infield, D., (2010). Wind characteristics on the Yucatán Peninsula based on short term data from meteorological stations. *Energy Conversion and Management,* 51(4)**,** 754-764.

Sørensen, J. N. r. & Shen, W. Z., (2002). Numerical Modeling of Wind Turbine Wakes. *Journal of Fluids Engineering,* 124(2)**,** 393-399.

Spera, D. A. (1994). *Wind Turbine Technology: Fundamental Concepts of Wind Turbine Engineering*. American Society of Mechanical Engineers.

State of Baja California. (2011). Analysis for La Rumorosa II wind farm location.

State of Baja California, (2014). La Rumorosa I wind farm operational data. Mexicali, Mexico: Baja California Energy Commission, BCEC.

Stensrud, D. J. (2009). *Parameterization Schemes: Keys to Understanding Numerical Weather Prediction Models*. Cambridge University Press.

Stevens, M. J. M. & Smulders, P. T., (1979). The estimation of the parameters of the Weibull wind speed distribution for wind energy utilization purposes. *Wind Engineering,* 3(2)**,** 132-145.

Stylianou, I., Cuevas-Figueroa, G. & Stallard, T., (2015). Prediction of wind farm energy yield using NWP considering within-cell wake losses. *Proc. European Offshore Wind Energy Conf. and Exhibition*.

Tennekes, H. & Lumley, J. L. (1972). *A first course in turbulence*. MIT press.

Versteeg, H. K. & Malalasekera, W. (2007). *An introduction to computational fluid dynamics: the finite volume method*. Pearson Education.

Volker, P., Badger, J., Hahman, A. & Ott, S., (2012). Wind Farm parametrization in the mesoscale model WRF. *EWEA - The European Wind Energy Association*.

Wang, C., Jin, S., Hu, J., Zhang, F., Feng, S. & Liu, C., (2011). Comparing different boundary layer schemes of WRF by simulation the low-level wind over complex terrain. *Artificial Intelligence, Management Science and Electronic Commerce (AIMSEC), 2011 2nd International Conference on***,** 6183-6188.

Warner, T. T. (2011). *Numerical weather and climate prediction*. Vol. 89: Cambridge University Press Cambridge, UK.

Wilson, T. H., (2012). The Evaluation of a Southern California Physics Ensemble.

Xiu, A. & Pleim, J. E., (2001). Development of a Land Surface Model. Part I: Application in a Mesoscale Meteorological Model. *Journal of Applied Meteorology,* 40(2)**,** 192-209.

Yang, Q., Berg, L. K., Pekour, M., Fast, J. D., Newsom, R. K., Stoelinga, M. & Finley, C., (2013). Evaluation of WRF-Predicted Near-Hub-Height Winds and Ramp Events over a Pacific Northwest Site with Complex Terrain. *Journal of Applied Meteorology and Climatology,* 52(8)**,** 1753-1763.

Zhang, Y., Dulière, V., Mote, P. W. & Salathé Jr, E. P., (2009). Evaluation of WRF and HadRM Mesoscale Climate Simulations over the US Pacific Northwest. *Journal of Climate,* 22(20)**,** 5511-5526.